Enhanced Diagrammatic Monte-Carlo Approaches for the Anisotropic Triangular Hubbard Model

A Project Report Submitted

in Partial Fulfilment of the Requirements

for the Degree of

Doctor of Philosophy

in

Physics

by

John Pooley



Division of Natural Sciences - School of Physics and Astronomy

Physics of Quantum Materials Group

University of Kent

June 2025

DECLARATION

I, **John Pooley**, hereby declare that, this report entitled **"Enhanced diagrammatic Monte-Carlo approaches for the anisotropic triangular Hubbard model"** submitted to the University of Kent towards partial requirement of **Doctor of Philosophy** in **Physics**, is an original work carried out by me under the supervision of Gunnar Möller and has not formed the basis for the award of any degree or diploma, in this or any other institution or university. I have sincerely tried to uphold the academic ethics and honesty. Whenever an external information, statements, or result are used, they have been duly acknowledged and cited.

University of Kent **John Pooley**

June 2025

ACKNOWLEDGEMENTS

I would like to express my deepest gratitude to my supervisor, Dr. Gunnar Möller, not only for his mentoring in matters of physics, infinite patience for my questions, and imparting his wisdom upon me, but also his kindness, and support over the period of my PhD. I would also like to extend my thanks to both Evgeny Kozik, and Connor Leniham for use of their software, and many fruitful discussions, which helped progress this project.

I would like to wholeheartedly thank my family. To my wife Hayley, I am eternally grateful for her endless love and support during these times, pushing me to go further, and never give up. Moreover for always putting up with me, even during difficult times. My children Brooke, and Jacob, I am thankful for their love, kindness, and humour which helped tremendously. I would also like to thank my mother, and my late father for always believing in my endeavours.

A special thanks to the PQM group, and the Ingram 208 PhD candidates, who shared this experience, even if it was only briefly due to COVID. Being part of the PQM group at Kent was a great experience and one that I will cherish.

I would also like to acknowledge the use of the Kent HPC cluster Icarus: "Specialist and High Performance Computing systems provided by Information Services at the University of Kent"

ABSTRACT

In this thesis we first describe the implementation of our code base, which acts as a framework in which Diagrammatic Monte Carlo (DiagMC) is accessible for multiple different theories, at both the one- and two-particle propagator levels. We implement "classical" DiagMC along with the shifted-action approach, which offers improvements in convergence by expanding around an arbitrary starting point. Monte-Carlo updates are generalised for n-legged vertices, and for both standard and anomalous Green's functions. Observable classes are easily implemented and we offer the possibility of including global basis functions in the Monte-Carlo weight to reduce variance. Finally, we present benchmark data to confirm the validity of our implementation.

We then turn to an investigation of the evolution from the metallic to insulating state of the anisotropic triangular lattice Hubbard model, with motivations arising due to the rich physics found in this model, and the somewhat varied results found in the literature. Moreover, to the authors knowledge there is only one published study which applies DiagMC to the model. We present results for a number of observables at $T = 0.5$, for which we have used re-summation methods to extrapolate to infinite order. We find a smooth crossover from metallic to insulating state for all anisotropies studied, and the formation of 120° quasi-antiferromagnetic order in the isotropic limit.

Contents

List of Figures **ix**

1 Introduction **1**

1.1 Outline 4

2 Background **5**

2.1 Diagrammatic Perturbation Theory 5

2.1.1 Propagators 8

2.1.2 Diagram Rules in momentum and imaginary-time 14

2.1.3 Dyson's equation 17

2.1.4 Bethe-Salpeter Equation 19

2.2 Lattice Models 20

2.2.1 The Hubbard Model 21

2.2.2 Observables 29

2.3 Series Resummation 31

3 Diagrammatic Monte-Carlo 34

3.1 Classical Diagrammatic Monte Carlo 37

3.1.1 Markov Chain Diagrammatic Monte Carlo 37

3.1.2 Sectors 46

3.1.3 Updates 47

3.2 Connected Determinant Diagrammatic Monte Carlo 60

4 Diagrammatic Monte Carlo Implementation 66

4.1 Alterations to standard Updates 67

4.1.1 Swap Measurement Alteration 68

4.1.2 Add/Remove Vertex Alterations 69

4.2 Update Validity Checks 70

4.3 Diagram Validity Checks 70

4.4 Scaled Integers 72

4.5 Code Structure & Implementations 73

4.5.1 Updates/Moves 74

4.5.2 Vertices 75

4.5.3 Diagrams 75

4.5.4 Observables 76

4.5.5 Move Accumulator 77

4.5.6 Sectors 77

4.5.7 Monte Carlo Algorithm 78

4.6 Observable matrices 79

4.7 Shift Position Sampling Biases at Second Order 79

4.8 Observables 85

4.8.1 Observable Normalisation 87

4.9 Basis Functions - Group Theory 92

4.9.1 Spatial basis functions for the square lattice 94

4.9.2 Temporal basis functions 96

4.10 Measurements 97

4.11 Autocorrelation time 99

4.12 Error calculations 100

4.13 Shifted action 101

4.13.1 Updates 103

5 Benchmarks **106**

5.1 Square Lattice Hubbard Model 106

5.1.1 Low Order Contributions 106

5.1.2 Comparison With Other Diagrammatic Methods 108

5.1.3 Momentum Depedency of the Self-Energy 109

5.1.4 Momentum Distribution Function 111

6 Anisotropic Triangular Hubbard Model Investigation **113**

6.1 Results 117

6.1.1 Density 117

6.1.2 Double occupancy, Potential energy, and Kinetic energy 120

6.1.3 Charge-Charge and Compressibility 124

6.1.4 Spin structure factor 129

6.1.5 Summary 135

7 Conclusion and Outlook **138**

7.1 Conclusion 138

7.2 Outlook 142

List of Figures

2.1 Some low order contributions to the ladder approximation. Labels have been omitted. The ladder approximation sums all diagrams with one hole-line(directed from right to left here). 7

2.2 Some low order Feynman diagrams. Solid lines represent propagators, and dashed lines represent interaction vertices. The third diagram is reducible and is implicitly included via Dyson's equation, hence must not be sampled in the proper self-energy. The imaginary time arguments are highlighted blue to differentiate them from the momentum labels. 15

2.3 An example of some low order disconnected diagrams. Labels have been omitted. The lower lines represent G_0, and the upper parts of the diagrams are fully closed diagrams denoted by F in the text. . . . 16

2.4 Graphical representation of Dyson's equation for a two-point propagator. Double line represents interacting propagator G, and single line represents non-interacting propagator G_0 18

2.5 Dispersion relations for various values of t' progressing from the square to the triangular lattice. Black contour indicates $\epsilon(k) = 0$. 25

2.6 Left: depiction of spins aligning anti-parallel to reduce the energy of the system. There is no configuration possible for the all spins to be anti-parallel. Right: at large interaction strengths the three spins form 120° angles between each other, to lower the energy of the system. 26

2.7 a) Basis used for simulations. b) triangular lattice. Arrow between a)-b) represents linear transformation described in text. c) Square lattice Brillouin Zone, with high symmetry points marked by red crosses. d) Triangular lattice Brillouin Zone with high symmetry points marked, with $\Gamma = (0, 0)$, $K' = (2\pi/3, 2\pi/\sqrt{3})$, and $M' = (0, 2\pi/\sqrt{3})$. 27

3.1 Schematic of labelling conventions used for the Hubbard model, more specifically two vertices numbered $1, 2$. s_n denotes a slot number, v_m the vertex number, $V_l = v_m - 1$ the vertex label, and l_k the absolute location in the diagram. 43

3.2 Two possible ways to internally connect a vertex. Vertex slots are indicated as white squares for incoming lines, and grey squares for outgoing lines. We use the connections shown on the left. 43

3.3 The same diagrams as shown in figure 2.2 as represented in our code. The dashed line indicates the measurement line which closes the diagrams. For brevity only one τ label is added, however each slot may have a different τ value associated with it, depending on the theory. . 44

3.4 Comparison of first order diagram drawn in the standard fashion (without external propagators), and depiction of our abstract representation used in simulations. 45

3.5 Depiction of the configuration change caused by the *Create/Delete worm* update. 48

3.6 Depiction of the change in momentum of a propagator line as the worm is moved across it. 50

3.7 Depiction of the change in momentum of a vertex as the worm is moved across it vertically. 51

3.8 Depiction of the change in momentum of a vertex as the worm is moved across it horizontally. 52

3.9 Depiction of the configuration change when the *Shift Position* update is performed on the upper incoming slot labelled τ 53

3.10 Depiction of the configuration change when sampling two-point diagrams, caused by the *Swap Measurement* update. 54

3.11 Depiction of configuration change caused by the *Reconnect* update. Only the corner of the vertices that are involved are shown for clarity. 55

3.12 Depiction of configuration change caused by the *Add/Remove* update. The newly added vertex is highlighted in blue for clarity. 56

3.13 Representation of a single $n = 4$ configuration. Line colours denote spin, black circles are vertices, and the blue circles denote the external points introduced by the extra creation and annihilation operators. Both the configurations contribute weight w to the partition function. 62

4.1 UML type diagram of top-level classes. All classes have a dependency on the Option Manager class, which has been disconnected for clarity. Solid lines indicates an association. Whilst dotted lines indicate a dependency. Lines point in the direction of the association/dependency 74

4.2 Probability distribution of drawing $\Delta\tau$ when τ_2, and τ_1 are both independently drawn from the interval $[0, \beta]$ 81

4.3 Second order momentum independent self-energy obtained via only the *Shift Position* update drawing a single τ value, showing the self-energy amplitude tending to zero as $\Delta\tau$ tends towards $\pm\beta$. On the $\Delta\tau$ axis the interval $[0, 1]$ represents $[0, \beta]$, and $(1, 2]$ represents $(-\beta, 0)$. 82

4.4 Examples of the symmetry adapted basis functions for the D4 point group with $\boldsymbol{r} = (2, 1)$. 95

4.5 The set of first and second order diagrams sampled for a shifted action expansion for the Hubbard Model. Red crosses indicate α counter terms. 102

4.6 Low order terms of diagrammatic expansion in ξ via shifted-action recursive method. Black lines represent bare propagators, blue lines represent $\tilde{G}^{(1)}$ i.e. dressed with $\tilde{a}_1$, and red lines $\tilde{G}^{(2)}$ i.e. dressed with $\tilde{a}_2$ 104

5.2 Second order contribution to the self energy at the nodal $\boldsymbol{k}_N = (\pi, 0)$, and anti-nodal $\boldsymbol{k}_{AN} = (\pi/2, \pi/2)$ points, as well as a generic point $\boldsymbol{k}_N = (3\pi/4, 3\pi/4)$ for various temperatures 107

5.3 Comparison of self-energy obtained via diagMC, DF, DΓA, and DCA for half filling at $\beta = 2$. 108

5.4 Benchmark Data for $\beta = 1.25$, With ReΣ for $U = 4$ (black), and $U = 8$ (black, dashed) and ImΣ for $U = 4$ (red), and $U = 8$ (red, dashed), and the corresponding reference data shown as points. . . . 109

5.5 Benchmark Data for $\beta = 2.0$, With ReΣ for $U = 4$ (black), and $U = 8$ (black, dashed) and ImΣ for $U = 4$ (red), and $U = 8$ (red, dashed), and the corresponding reference data shown as points. 110

5.6 Benchmark Data for $\beta = 5.0$, With ReΣ for $U = 4$ (black), and $U = 8$ (black, dashed) and ImΣ for $U = 4$ (red), and $U = 8$ (red, dashed), and the corresponding reference data shown as points. 110

5.7 The momentum distribution $n(\boldsymbol{k})$ for different temperatures, showing the sharpness of the Fermi surface increasing with decreasing temperature. 112

6.1 Left: partial summation of density at $\beta = 0.5$, for μ corresponding to half filling in the non-interacting limit. Right: same as left at $\beta = 2.0$. Note the overlap of the 0th and 1st order, as we nullify tadpole diagrams via an alpha shift such that the first order contribution is zero. 118

6.2 Left: Density extrapolated to infinite order via Dlog-Padé for various chemical potentials at $\beta = 0.5$. Right: same as left at $\beta = 2.0$ 119

6.3 Double occupancy extrapolated to infinite order via Dlog-Padé for various chemical potentials at $\beta = 2.0$. The black line with triangular markers indicates double occupancy at half filling. Inset: derivative of D with respect to U. 120

6.4 Left: Double occupancy as a function of temperature. A minimum in D is found at $\beta \approx 2.0$. The increase in D as temperature is reduced past $\beta \approx 2.0$ indicates an increase in entropy. Right: Kinetic energy for temperatures $\beta = 2.0, 1.6$ and $t' = 1.0, 0.8, 0.6$ showing a crossover in the derivative with respect to temperature at large U, which decreases with t'. 122

6.5 Left: Potential energy showing expected behaviour for metallic to insulating crossover. Right: Kinetic energy showing the same behaviour123

6.6 Curves of compressibility κ for different temperatures showing the condition $\partial\kappa/\partial T = 0$ is met at $U \approx 6.7$ defining the crossover. 125

6.7 Compressibility curves at half filing for $\beta = 2.0$ and $\beta = 1.6$, showing the condition $\partial\kappa/\partial T = 0$ occuring for lower U as t' increases. Note that the curves for $t' = 0.8$, and $t' = 0.6$ have been shifted by $+0.05$, and $+0.1$ respectively. 125

6.8 Compressibility curves for different chemical potentials at $\beta = 2.0$. The curves overlay each other at intermediate U values before splitting at large U. 126

6.9 Plot comparing magnitude of local C_{loc}, and nonlocal C_{nl} charge correlations, highlighting the similarity in magnitude but difference in sign. 127

6.10 Left: Charge correlation on the same sublattice as $\boldsymbol{r} = (0, 0)$ as function of U for different chemical potentials. $\boldsymbol{r} = (1, -1)$ is identical to $\boldsymbol{r} = (-1, 1)$ and not plotted. Right: Charge correlation on different sublattices. $\boldsymbol{r} = (1, 0), (0, 1)(0, -1), (-1, 0)$ are identical to $\boldsymbol{r} = (1, 1)$ and not plotted 128

6.11 The evolution of the magnetic structure factor peak moving from M' to K as a t' increases at both small, and large interaction strength. . 130

6.12 Spin-spin correlator in real space at both low and high U values. The triangular sublattices are labelled on the top right heatmap. t' decreases when moving down a row, and we see the evolution from a three-sublattice state toward a two-sublattice state. 132

6.13 The spin structure factor for $\beta = 4, 10$ showing a decrease in the magnitude at the K-point, when compared with $\beta = 2$. 133

6.14 The spin structure factor for $\beta = 4$, $U = 4$, across the full Brillouin zone for $t' = 1.0, 0.75, 0.5, 0.25$. 134

6.15 The spin structure factor for $\beta = 10$, $U = 4$, across the full Brillouin zone for $t' = 1.0, 0.75, 0.5, 0.25$. 136

Chapter 1

Introduction

Solid state physics is concerned with the behaviour of a macroscopic number of interacting particles (of the order of 10^{23}), which in general, have non-trivial interactions with each other. A solution to the Schrödinger equation for such a system is not plausible, since the memory required to store the wave function grows exponentially with the number of particles. As such, a brute force approach to solve a system via the full representation of the wave function is not viable. We therefore seek approaches that can approximate the problem effectively. In certain situations we are able to map the interacting problem onto a single particle system in a stationary potential, for which we can obtain a solution. This is the premise of mean-field theory (MFT). However we find that many phenomena, e.g. High-Temperature superconductivity[1], only occur when we consider the collective behaviour of the system as a whole. That is to say, the system is more than just its individual constituents. Solid state physics is the study of such systems.

[1] Conventional superconductivity is described well by MFT, however High-Temperature or 'unconventional' superconductivity goes beyond the realm of MFTs.

The problem, however, is less black-and-white than stated in the previous paragraph. We may describe many materials via density functional theory (DFT) which treats systems as free electrons in a potential which arises from the other electrons in the system, as well as the nuclei. DFT has had great success in describing crystal structures and the electronic energy bands associated with them, and is widely applied by many physicists, and chemists. Such great success has lead to very elaborate open source programs such as Abinit[1], allowing researchers to apply DFT without developing their own code, and knowing all the technical details of the technique. Systems that can be approached via DFT, in general, fit into the regime of weakly correlated models. However, in materials with strong local interactions, the description in terms of a single-particle band structure is not sufficient to capture all of the physics. Moreover, the density functional is also only known approximately.

Many of the more exotic phenomena, such as the Mott insulating state, arise when we are in the strongly correlated regime. This regime is more difficult to investigate as, generally, we may not extrapolate the behaviour of the system from that of a small number of particles, and furthermore, many phenomena that arise are emergent properties, that only appear when considering the behaviour of the system en-masse[2] – we may still obtain valid information from simplified models, albeit not the full story. In 1963 Hubbard proposed a model [2] to try and tackle this regime – more precisely itinerant ferromagnetism. The "standard" model of condensed matter theory, contains electron kinetic energy, electron-electron interactions, electron-ion interactions, ion kinetic energy, and ion-ion interactions. Solving such a model is infeasible. Hubbard took this generic model and applied a series of approximations – considering the ionic nuclei to be stationary, and therefore the potential the electrons see is periodic, taking the basis of Wannier functions restricted to the first band,

[2]For an excellent expose on the matter see "More Is Different" by Phil Anderson

considering the coulomb interaction to be a contact interaction, and only allowing electrons to hop to directly adjacent sites – leaving only the kinetic and potential energy term of the electrons. The Hubbard model is given by the Hamiltonian

$$\mathcal{H} = -t \sum_{\langle i,j \rangle, \sigma} \left(c^{\dagger}_{i,\sigma} c_{i+1,\sigma} + c^{\dagger}_{i+1,\sigma} c_{i,\sigma} \right) + U \sum_{i} n_{i,\uparrow} n_{i,\downarrow}, \tag{1.1}$$

where we have used second quantisation nomenclature such that, $c^{\dagger}_{i}(c_i)$ are creation(annihilation) operators at site i, $n_{i,\sigma} = c^{\dagger}_{i,\sigma} c_{i,\sigma}$ is the number operator, $U \equiv U_{ii}$ is the on-site Coulomb repulsion, the brackets on the sum $\langle \dots \rangle$ restricts the sum to nearest neighbours, and t is the hopping term, which corresponds to the hopping matrix element between two adjacent sites [3], where $t_{ij} = t_{ji} \equiv t$.

This seemingly simple model, which has just two parameters – which may also be expressed as a single parameter model in $U/|t|$ – is only exactly solvable in certain regimes, those being, the limit of zero coupling ($U \to 0$), infinite coupling ($U \to \infty$), and 1-dimensional, or infinite dimensional systems – For infinite dimensions the solution came from application of dynamical mean-field theory [4] (DMFT). However many systems of interest fall somewhere in-between this range, and due to this the Hubbard model has been widely researched for many years. Solutions for the Hubbard model at various values of U are crucial as the model is thought to describe phenomena in many physical materials. For instance the three-band Hubbard model is thought to describe the interactions that occur in Cu-O_2 planes found in high temperature superconducting cuprate materials [5]. Furthermore, the Hubbard model exhibits Mott insulating behaviour for $U \gg t$ where the system becomes insulating due to the large on-site energy cost of a site being doubly occupied. The high energy penalty causes sites to become singly occupied and the opening of a charge gap. Also

of interest is the realisation of the Hubbard model via quantum emulators, such as optical lattices. Many numerical techniques have been developed to study this intermediate regime, such as DMFT, density matrix renormalization group (DMRG), Quantum Monte-Carlo (QMC), and Diagrammatic Monte Carlo (DiagMC). DiagMC will be the focus of this thesis.

1.1 Outline

This thesis is, firstly, concerned with our pursuit of creating a "plug and play" code base for DiagMC simulations, in which, an expansion that employs bare vertices, can be implemented simply by defining the vertex, dispersion relation, and type of propagator, e.g. normal or anomalous. To this end, chapter 2 gives an introduction to Many-body perturbation theory, in the guise of diagrammatic expansions, as well as details of the Hubbard model in preparation of chapter 6. Chapter 3 describes Markov chain Diagrammatic Monte Carlo, as well as Connected Determinant Diagrammatic Monte Carlo (cDet), and briefly discusses closely related numerical techniques. Chapter 4 then details the implementation of our code base, along with a discussion of issues found with the *shift position* update. Chapter 5 details benchmarking carried out to validate the code base, where we compute the full momentum dependency of the self-energy up to 6th order for the Hubbard model on a square lattice at half filling, along with other results. Finally in chapter 6 we summarise the literature on the evolution from metallic to insulating states of the anisotropic triangular lattice Hubbard model, and present results for various observables in the intermediate temperature range.

Chapter 2

Background

This, and the following chapter, aim to provide the reader with the relevant background information required to understand the research presented in this thesis. In this chapter we discuss the physics of diagrammatic perturbation theory – which is required to understand diagMC techniques – as well as a discussion of the Hubbard model, its magnetic states, and the Mott insulator, which is relevant for chapter 6. The next chapter introduces diagMC in terms of both classical diagMC and connected determinant diagMC.

2.1 Diagrammatic Perturbation Theory

As mentioned in the introduction, solid state physics is concerned with the study of a macroscopic number of interacting particles. Since we are, in general, unable to find analytical solutions to such problems, we might apply what is known as Many-body

perturbation theory (MBPT). The premise is that we begin by describing a system of free electrons, and turn on the interaction perturbatively. This amounts to a series expansion in the coupling parameter U, where each successive term takes into account one extra interaction, i.e. the nth order term gives the contribution from n interactions (more below). For small enough U we find that the corrective terms decrease with increasing order, however, for U in the strongly correlated regime this is generally not the case, and we must include many orders of expansion to obtain the limiting value of the series. To be more concrete consider a Hamiltonian H, that cannot be solved exactly, which we decompose as follows,

$$H = H_0 + H_I, \tag{2.1}$$

where H_0 is the non-interacting part, and H_I the interacting part. We begin with the free system, H_0, and calculate the effects of adding H_I perturbatively via a series expansion. There are, of course, subtleties to this. Performing the expansion requires calculating multi-dimensional integrals that, in general, require numerical techniques. Furthermore, we are not guaranteed convergence even if we can calculate the integrals. A pragmatic treatment of a perturbative expansion usually results in the resummation of certain classes of diagrams via Dyson's equation[1], often called a partial summation. The choice of diagrams to resum is chosen due to their physical importance, or their overall contribution to the series expansion. One such choice is the 'ladder approximation', which is useful for describing a low density system of interacting particles. It consists of summing all diagrams with a either zero, or one hole propagator[2] – where a hole is the lack of an electron in a certain momentum

[1] See section 2.1.3

[2] Propagators are explained later in this chapter.

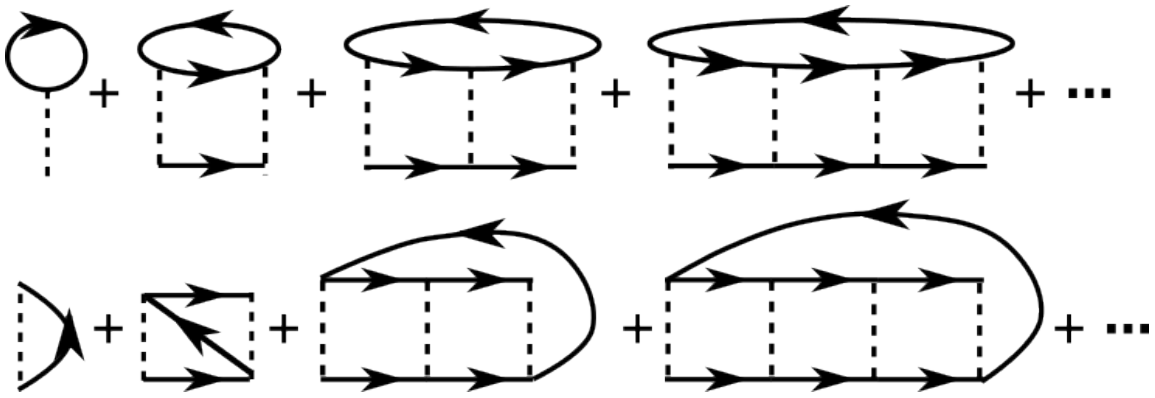


Figure 2.1: Some low order contributions to the ladder approximation. Labels have been omitted. The ladder approximation sums all diagrams with one hole-line(directed from right to left here).

state within the Fermi surface. The ladder approximation is shown in Fig. 2.1. Since the density of the system is low, the Fermi momentum $\boldsymbol{k}_F$ is small. Holes are produced by scattering an electron into a higher energy state, and therefore the momentum integral for hole propagators is considered in the region $|\boldsymbol{p}| < \boldsymbol{k}_F$, whereas the particle propagator lines have momentum integrals for $|\boldsymbol{p}| > \boldsymbol{k}_F$. Since $\boldsymbol{k}_F$ is small the integrals for particle propagators give a greater contribution [6, 7]. By considering only the ladder diagrams we may obtain the largest contributions to the expansion whilst drastically reducing the number of diagrams we need to consider for each expansion order – such expansions are applied in the Ladder Dual Fermion Approximation, which is a diagrammatic extension to DMFT [8, 9]. We are however, still not guaranteed convergence when performing a sum over classes of diagrams.

Quantum field theory (QFT) is a large area of physics in which fields[3] play the main role. The central function of condensed matter field theory is many-body

[3]In QFT particles are replaced by fields. Fields are assigned a value at all points in space-time, and excitations of the field correspond to particles, e.g. a photon is an excitation in the electromagnetic field.

physics [6, 10], and as such many-body physics can be explained in the nomenclature used in QFT. The goal of QFT is to calculate expectation values for observables which are given as correlation functions. Free-field theories are bilinear in field operators, for which correlation functions can be calculated exactly via Gaussian integration. When interactions are introduced, the Gaussian integration can no longer be performed. However, thanks to Wicks theorem we can express n-point correlation functions – where n is the number of field operators in the correlation function, e.g. a two body interaction is described by a four-point correlation function – as the sum of products of two-point correlation functions. The terms in this series may be expressed as Feynman diagrams, where each Feynman diagram is a pictorial representation of a multidimensional integral. MBPT can be performed by summing over Feynman diagrams. To accurately calculate thermodynamic observables, we should ideally sum over all Feynman diagrams, however, a subset of diagrams is often used in practice, as explained above. The Dyson, or the Bethe-Salpeter equations when working with two- or four-point diagrams respectively, may be used to sum a given series to infinite order.

2.1.1 Propagators

The building blocks of Feynman diagrams are interaction vertices and propagators. Interaction vertices represent the interaction between particles, e.g. the Coulomb interaction, and in general have both spatial(momentum) and temporal(frequency) dependencies. Propagators, also known as Green's functions, describe the propagation of a particle, or hole, in space-time. The single-particle propagator is a two-point correlation function, and the two-particle propagator is a four-point cor-

relation function. At finite temperature, we work in the grand canonical ensemble where $H \to H - \mu N$, and averages must be taken over an ensemble of states. We define the thermal density matrix as

$$\hat{\rho} = e^{-\beta H}, \tag{2.2}$$

where $\beta = 1/T$, is the inverse temperature. The partition function is then

$$Z = \mathrm{Tr}[\hat{\rho}] = \mathrm{Tr}[e^{-\beta H}], \tag{2.3}$$

where Tr is the trace over states. We may then define the thermal expectation value of an operator $\hat{O}$ to be

$$\langle \hat{O} \rangle = \frac{\mathrm{Tr}[\hat{O}\hat{\rho}]}{\mathrm{Tr}[\hat{\rho}]} = \frac{\mathrm{Tr}[\hat{O}e^{-\beta H}]}{\mathrm{Tr}[e^{-\beta H}]} = Z^{-1}\,\mathrm{Tr}[\hat{O}e^{-\beta H}]. \tag{2.4}$$

In general correlators involve taking the expectation value of multiple operators, and generically we may write a correlator of many operators as,

$$C(t_a, \ldots, t_z) = \langle A(t_a)B(t_b)\ldots Y(t_y)Z(t_z)\rangle. \tag{2.5}$$

For a two-point correlation function of Heisenberg operators $A(t)$, and $B(0)$, this corresponds to

$$C_{AB}(t) = Z^{-1}\,\mathrm{Tr}[e^{-\beta H}e^{iHt}Ae^{-iHt}B], \tag{2.6}$$

where the time argument of the second operator has been set to 0, without loss of generality for time-independent Hamiltonians. To avoid having to perform two perturbative expansions, we use the Matsubara formulation and treat time as an

imaginary temperature. Setting $\tau = it$ allows us to group the thermal density matrix with the time dependence of the Heisenberg operator, which in the Matsubara formalism is $O_H(\tau) = e^{H\tau}Oe^{-H\tau}$. The correlation function is then

$$C_{AB}(\tau) = Z^{-1}\,\mathrm{Tr}[e^{-\beta H}e^{H\tau}Ae^{-H\tau}B]. \tag{2.7}$$

Propagators come in many flavours, but here, we will be interested in the imaginary time one-particle (two-point), and two-particle (four-point) propagators, with the forms

$$G_{\mu\nu}(1;2) = -\langle \mathcal{T} c_\mu(1)c_\nu^\dagger(2)\rangle \tag{2.8}$$

$$G_{\mu\nu\delta\gamma}(1,3;2,4), = \langle \mathcal{T} c_\mu(1)c_\nu(2)c_\delta^\dagger(3)c_\gamma^\dagger(4)\rangle, \tag{2.9}$$

where the shorthand $1 = (\boldsymbol{x}_1, \tau_1)$ has been used. $c_\mu^\dagger(1)(c_\mu(1))$ are creation(annihilation) field operators, that create(destroy) a particle at position and imaginary time $(\boldsymbol{x}_1, \tau_1)$, with spin μ. $\mathcal{T}$ is the Wick time ordering operator, which places operators in time descending-order. This operator introduces a factor of (-1) when two fermion field operators are swapped, due to their anti-commutation relation $\{c_\mu, c_\nu^\dagger\} = \delta_{\mu,\nu}$.
To obtain a perturbative expansion for the Green's function, we move to the interaction picture, where Heisenberg operators evolve according to the bilinear (free) part of the hamiltonian, H_0,

$$O_I(\tau) = e^{H_0\tau}Oe^{-H_0\tau}. \tag{2.10}$$

We then define the time evolution operator for the interaction Hamiltonian $H_I = H - H_0$, to be $U_I(\tau) = e^{H_0\tau}e^{-H\tau}$, for which we may calculate the equation of motion,

leading to the time ordered exponential

$$U_I(\tau) = \mathcal{T} \exp\Big[- \int_0^\tau H_I(\tau')d\tau' \Big]. \tag{2.11}$$

Inserting the time evolution operator into the definition of the Green's function yields[4]

$$G_{\mu\nu}(1;2) = -\frac{\mathrm{Tr}[e^{-\beta H_0} U_I(\beta) c_I(1) c_I^\dagger(2)]}{\mathrm{Tr}[e^{-\beta H_0} U_I(\beta)]}. \tag{2.12}$$

We may then develop the Green's function as a power series expansion in H_I, where expectation values $\langle \dots \rangle_0 = \mathrm{Tr}[e^{-\beta H_0} U_I(\beta) \dots]$ are taken with respect to the non-interacting part of the Hamiltonian, leading to

$$G_{\mu\nu}(1;2) = -Z_0^{-1} \sum_{n=0}^{\infty} \frac{(-1)^n}{n!} \int_0^\beta d\tau_1 \dots d\tau_n \langle \mathcal{T} H_I(\tau_1) \dots H_I(\tau_n) c_\mu(1) c_\nu^\dagger(2) \rangle_0. \tag{2.13}$$

As an example consider the case of $n = 2$, and let $G^{(2)}$ represent Eq. (2.13) with the sum restricted to $\sum_{n=0}^{2}$,

$$\begin{aligned} G_{\mu\nu}^{(2)}(1;2) = G_0(1;2) - \int_0^\beta d\tau_1 \langle \mathcal{T} c_\mu(1) c_\nu^\dagger(2) H_I(\tau_1) \rangle_0 + \dots \\ \frac{1}{2!} \int_0^\beta d\tau_1 d\tau_2 \langle \mathcal{T} c_\mu(1) c_\nu^\dagger(2) H_I(\tau_1) H_I(\tau_2) \rangle_0, \end{aligned} \tag{2.14}$$

where, H_I will be some product of field operators greater than bi-linear in order, e.g.

$$H_I = c_\mu^\dagger(1) c_\nu^\dagger(2) c_\mu(3) c_\nu(4). \tag{2.15}$$

[4]Much of the algebra in developing equation 2.12 and how operators in the interaction picture relate to Heisenberg operators has been omitted. For a detailed walk-through see pages 157-162 in [11].

The first term represents particle propagation from (1) to (2) without any interactions – this is the non-interacting propagator labelled G_0. The second term describes propagation with a single interaction occurring, and the third term propagation of a particle that experiences two separate interactions at imaginary times τ_1 and τ_2. By extrapolating this to infinite order, we see that the propagator $G_{\alpha,\beta}(1;2)$ is given as the contribution of all possible ways the particle may propagate from (1) to (2), e.g. freely, or with n interactions occurring.

We may express the propagator in $\boldsymbol{k}, \tau$ via a standard Fourier transform

$$G(\boldsymbol{k},\tau) = \int \frac{d\boldsymbol{k}}{(2\pi)^d} e^{-i\boldsymbol{k}\boldsymbol{x}} G(\boldsymbol{x},\tau). \tag{2.16}$$

To find the non-interacting propagator we substitute the Hamiltonian $H_0 = \sum_{\boldsymbol{k}} \epsilon_{\boldsymbol{k}} c^\dagger_{\boldsymbol{k}} c_{\boldsymbol{k}}$ into Eq.(2.13), and perform a fourier transform, which reduces to

$$G_0(\boldsymbol{k},\tau) = -\langle \mathcal{T} c_{\boldsymbol{k}}(\tau) c^\dagger_{\boldsymbol{k}}(0)\rangle = -[\theta(\tau)\langle c_{\boldsymbol{k}}(0) c^\dagger_{\boldsymbol{k}}(0)\rangle + \theta(-\tau)\langle c^\dagger_{\boldsymbol{k}}(0) c_{\boldsymbol{k}}(0)\rangle] e^{-\epsilon_{\boldsymbol{k}}\tau}, \tag{2.17}$$

where the Heaviside step function $\theta(\tau)$ ensures causality, and we have used $c_{\boldsymbol{k}}(\tau) = c_{\boldsymbol{k}}(0) e^{-\epsilon_{\boldsymbol{k}}\tau}$. For fermions[5] the equal-time expectation value is the Fermi-Dirac distribution function, $\langle c^\dagger_{\boldsymbol{k}}(0) c_{\boldsymbol{k}}(0)\rangle = f(\xi)$, leading to

$$G_0(\boldsymbol{k},\tau) = \begin{cases} -\dfrac{e^{-\xi\tau}}{1+e^{-\beta\xi}} & \tau > 0 \\ \dfrac{e^{-\xi\tau}}{1+e^{\beta\xi}} & \tau \leq 0, \end{cases}$$

where $\xi \equiv \xi(\boldsymbol{k})$ is the dispersion relation of the system, with its dependence on $\boldsymbol{k}$ suppressed for brevity.

[5]For bosons the equal-time expectation value gives the Bose-Einstein distribution

The commutation relation of the operators enforce a periodicity in τ, such that

$$G(\boldsymbol{x}, \tau + \beta) = \zeta G(\boldsymbol{x}, \tau), \tag{2.18}$$

where $\zeta = 1$ for bosons, and -1 for fermions, i.e. the Green's function is periodic in τ for bosons, and anti-periodic for fermions. Such a periodicity implies the representation of $G(\tau)$ in terms of a Fourier series in imaginary frequencies, which leads to the Matsubara representation [10, 12], defined by

$$G(\boldsymbol{x}, \tau) = \frac{1}{\beta} \sum_{i\omega_n} G(i\omega_n) e^{-i\omega_n \tau}. \tag{2.19}$$

Here the required set of frequencies depends on the particle statistics. We are interested in fermions, for which $i\omega_n = (2n+1)\pi/\beta$, while bosons require $i\omega_n = 2n\pi/\beta$. The non-interacting propagator defined in momentum-frequency space has the simple analytical form,

$$G_0(\boldsymbol{k}, i\omega_n) = \frac{1}{i\omega_n - \xi(\boldsymbol{k})}. \tag{2.20}$$

To evaluate the Green's function for interacting systems we apply Wick's theorem, which states that we may calculate the expectation value of a product of operators by summing over all contractions – a contraction is the expectation value of a pair of operators. To fully contract the expression for G, we find all permutations of pairs of operators, along with the permutation sign $(-1)^P$, and take their expectation value. Carrying out such a procedure we find that all terms consisting of two creation(annihilation) operators vanish i.e. the overlap of the original state, and that with two particles added(removed) is zero. The non-vanishing contractions may be conveniently represented pictorially as Feynman diagrams, which we can construct by following the Feynman rules.

2.1.2 Diagram Rules in momentum and imaginary-time

To construct the Feynman diagrams at a given order N, where each order represents a single instance of H_I in Eq. (2.13), we follow the Feynman rules [11].
For a two-point diagram, the Feynman rules in momentum and imaginary-time, are the following:

1. Draw all topologically distinct diagrams with N interaction vertices, and $2N+1$ directed lines. A two-point diagram will have 2 external lines, and $2N-1$ internal lines.

2. Label the external lines by $(\boldsymbol{k}, \tau, \sigma)$. Label each internal line with a spin, momentum, and imaginary time label. Follow conservation rules for the theory you are investigating, e.g. momentum and/or spin conservation at each vertex. To each interaction line assign a direction, momentum, and an imaginary time label at each end.

3. Assign a factor $G_0(\boldsymbol{p}, \tau_j - \tau_i)$ to each fermion line carrying momentum $\boldsymbol{p}$, that runs from vertex i to j, which have times τ_i, and τ_j respectively.

4. Assign a factor $V(\boldsymbol{q})$ to each interaction line, e.g. $V(\boldsymbol{q}) = U$ for the Hubbard model.

5. Integrate over all independent internal momenta and times.

6. Assign a factor of $(-1)^{F_L}(-1)^N$, where F_L is the number of closed fermion loops, and N the diagram order.

7. Treat any Green's function that connects vertices with equal times as $G_0(\boldsymbol{k}, \tau = 0^-)$.

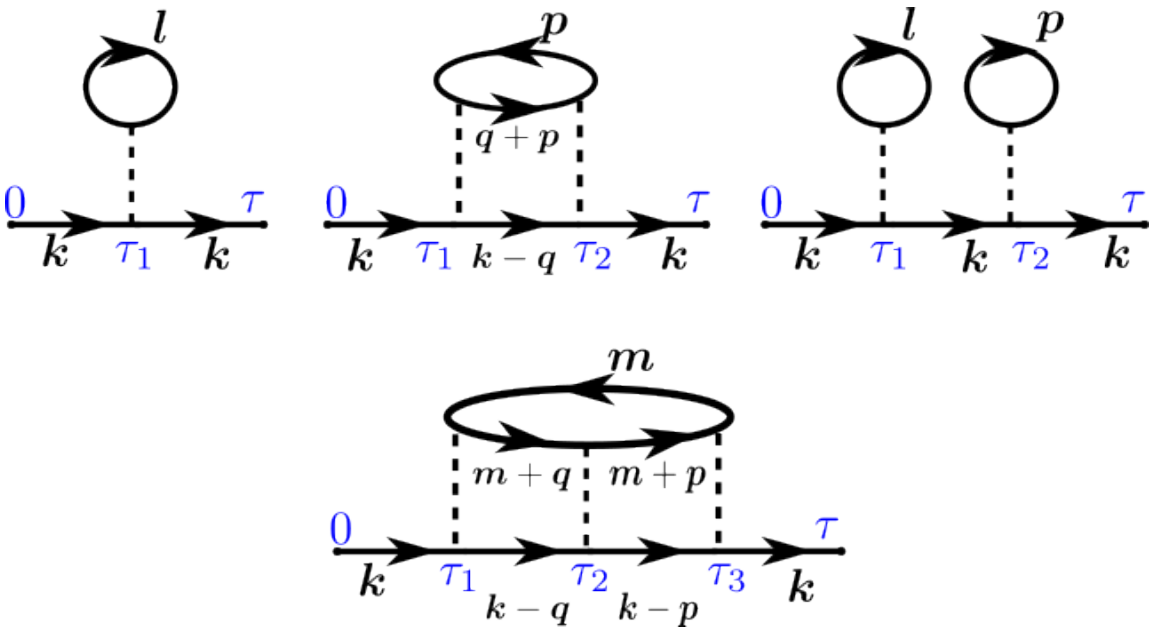


Figure 2.2: Some low order Feynman diagrams. Solid lines represent propagators, and dashed lines represent interaction vertices. The third diagram is reducible and is implicitly included via Dyson's equation, hence must not be sampled in the proper self-energy. The imaginary time arguments are highlighted blue to differentiate them from the momentum labels.

Rule 7 arises due to contractions of the form $\overrightarrow{c^\dagger(\tau)c}(\tau)$, which are ill-defined as they occur at equal times. We interpret this as,

$$\overrightarrow{c^\dagger(\tau)c}(\tau) = \overrightarrow{c^\dagger(\tau+0^+)c}(\tau) = \langle \mathcal{T} c(\tau)c^\dagger(\tau+0^+)\rangle = G_0(\boldsymbol{k}, 0^-). \tag{2.21}$$

Some low order connected diagrams are shown in Fig. 2.2. A connected diagram consists of all propagators being connected to each other via interaction vertices. However, the full set of diagrams produced by performing Wick-contractions on Eq. (2.13) will also contain disconnected graphs, of the form G_0F, where F is a sub-diagram in which all lines are closed within itself. An example of some disconnected diagrams are shown in Fig. 2.3. We need not worry about these diagrams since the

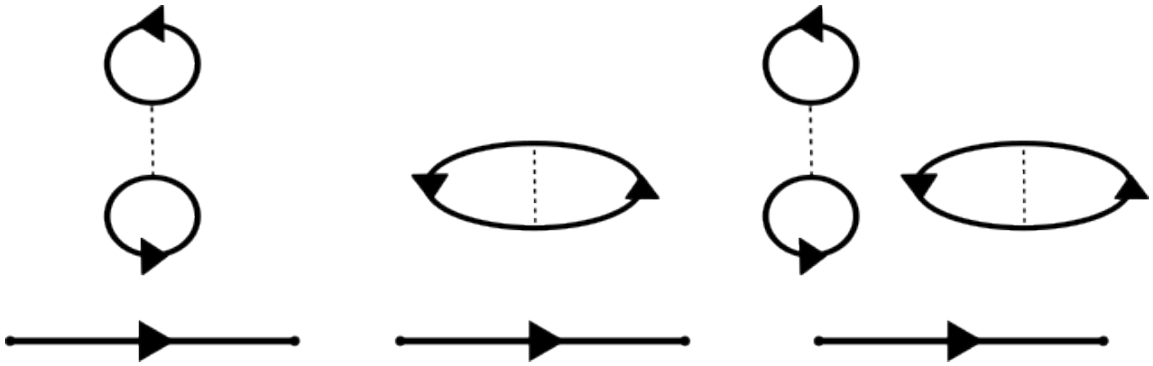


Figure 2.3: An example of some low order disconnected diagrams. Labels have been omitted. The lower lines represent G_0, and the upper parts of the diagrams are fully closed diagrams denoted by F in the text.

expansion of the partition function in Eq. (2.13) produces exactly the same diagrams as the disconnected part of the expansion, and hence these cancel [10]. To see this, consider Eq. (2.13), with the non-interacting partition function Z_0^{-1} expanded as a power series in $H_I(\tau)$,

$$G_{\mu\nu}(1,2) = \frac{\sum_{n=0}^{\infty} \frac{(-1)^n}{n!} \int_0^\beta d\tau_1 \dots d\tau_n \langle \mathcal{T} c_\mu(\tau) c_\nu^\dagger(0) H_I(\tau_1) \dots H_I(\tau_n) \rangle_0}{\sum_{n=0}^{\infty} \frac{(-1)^n}{n!} \int_0^\beta d\tau_1 \dots d\tau_n \langle \mathcal{T} H_I(\tau_1) \dots H_I(\tau_n) \rangle_0}, \tag{2.22}$$

since there are no external field operators in the denominator, an expansion produces closed diagrams only, an example being the top part of the first diagram in Fig. 2.3, whereas the expansion of the numerator produces both connected diagrams, like those shown in Fig. 2.2, and disconnected diagrams. The disconnected parts of the diagram can be factored out of the numerator, and exactly cancel with those in the denominator i.e. the Linked Cluster theorem.

Using the Feynman rules, we may construct the multi-dimensional integrals in $\boldsymbol{k}, \tau$ directly from the Feynman diagram. For example the second diagram in Fig. 2.2 –

ignoring the external propagators – represents the integral,

$$\int d\tau_1 d\tau_2 \frac{d^d\boldsymbol{q}}{(2\pi)^d}\frac{d^d\boldsymbol{p}}{(2\pi)^d} V^2(\boldsymbol{q}) G_0(\boldsymbol{k}-\boldsymbol{q}, \tau_2-\tau_1) G_0(\boldsymbol{p}+\boldsymbol{q}, \tau_2-\tau_1) G_0(\boldsymbol{p}, \tau_1-\tau_2), \quad (2.23)$$

where d is the dimension of the system. Note that we do not integrate over the external momentum $\boldsymbol{k}$ and time τ as they are fixed; however, to account for all possible configurations of a diagram we must integrate over all internal momenta and times, as stated in rule 5.

As is clear from the above details, each diagram corresponds to a multi-dimensional integral over both momentum(position) and imaginary time(or a sum over frequencies), with the number of integrals increasing with diagram order. We must employ numerical techniques to solve such integrals, as they do not have closed form solutions.

Since the number of diagrams grows as the factorial of the diagram order, obtaining an expression for the fully interacting G seems implausible. However, Dyson's equation aids in this endeavour [13].

2.1.3 Dyson's equation

Consider two-point diagrams in momentum space, each diagram has two external propagators, as such, the diagram has an algebraic form of $G_0 B G_0$, where B is determined by the topology of the diagram. By inspection of the closed diagrams we can see that there are two types of diagrams, those that may be split into two by cutting a single propagator line, and those that cannot. We define the *irreducible* self-energy, Σ, as the sum of all sub-diagrams that are connected to a diagram via

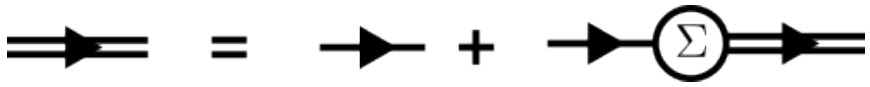


Figure 2.4: Graphical representation of Dyson's equation for a two-point propagator. Double line represents interacting propagator G, and single line represents non-interacting propagator G_0

two particle lines, and cannot be separated into two distinct diagrams by cutting a single propagator line. These diagrams are called one-particle irreducible (1PI). Hence, the full Green's function can be written as a geometric series over all possible numbers of insertions of self-energy graphs, as follows

$$G = G_0 + G_0\Sigma G_0 + G_0\Sigma G_0\Sigma G_0 + G_0\Sigma G_0\Sigma G_0\Sigma G_0 + \dots \ . \tag{2.24}$$

In $\boldsymbol{k}, i\omega_n$ this reduces to the analytical expression

$$G(\boldsymbol{k}, i\omega_n) = G_0(\boldsymbol{k}, i\omega_n) + G_0(\boldsymbol{k}, i\omega_n)\Sigma(\boldsymbol{k}, i\omega_n)G(\boldsymbol{k}, i\omega_n) = [G_0(\boldsymbol{k}, i\omega_n)^{-1} - \Sigma(\boldsymbol{k}, i\omega_n)]^{-1}. \tag{2.25}$$

This is shown pictorially in Fig. 2.4. Since we know the analytical form of the non-interacting propagator G_0, we can obtain the fully interacting propagator G, by calculating the irreducible self-energy Σ. The self-energy consists of many diagrams, however, pragmatically we are able obtain a good estimate with a finite order calculation, and if we are not, then the problem is not amenable to perturbative expansions.

Thermodynamic properties of a system can then be obtained via G. For instance the momentum distribution function of the interacting system is given by

$$n_\sigma(\boldsymbol{k}) = G_\sigma(\boldsymbol{k}, \tau = 0^-), \tag{2.26}$$

which may then be used along with the dispersion relation $\xi(\boldsymbol{k})$ to calculate the kinetic energy,

$$T = \sum_{\sigma} \int \frac{d^d k}{(2\pi)^d} \xi(\boldsymbol{k}) n_\sigma(\boldsymbol{k}) \tag{2.27}$$

2.1.4 Bethe-Salpeter Equation

We may perform an analogous treatment for four-point diagrams via the Bethe-Salpeter equations [14]. Similar to splitting the two-point diagrams into bare propagators and self-energy insertions, the four-point diagrams can be decomposed into pairs of propagators and the reducible vertex function. Like the irreducible self-energy, we may obtain the irreducible vertex function by considering blocks of diagrams that cannot be cut into two by cutting either: a pair of particle propagators, or a pair of particle-hole propagators. These are defined as the irreducible particle-particle, and particle-hole vertex functions respectively. Analogously to Dyson's equation we may write equations for the four-point diagrams in terms of the irreducible vertex,

$$\chi = \chi_0 + \chi_0 \Gamma \chi. \tag{2.28}$$

Where χ is the full two-particle propagator, $\chi_0 = G_0(\boldsymbol{p}) G_0(\boldsymbol{k})$ the non-interacting two-particle propagator, and Γ the irreducible vertex function in either the particle-particle, or particle-hole channel.

In summary, the general goal when applying diagrammatic perturbation theory – to condensed matter systems in the low energy regime – is to calculate the observable of interest via its correlation function. For The Green's function this amounts to

calculation of the irreducible self-energy(vertex function), which is plugged-in to Dyson's(Bethe-Salpeter) equation to obtain the fully interacting propagator. The propagator is then used to obtain the thermodynamic properties of the system.

2.2 Lattice Models

The creation of models that include all features of real materials, and can be solved analytically or by numerical methods, currently remains an insurmountable task. Real materials contain impurities, disorder, grain boundaries[6], etc., and the inclusion of multiple of these phenomena often leads to the problem becoming intractable. As such, the models found in condensed matter physics make some simplifying assumptions, which enable us to to bridge the gap between theory and experiment. We will discuss one such set of simplifications, which results in a class of models called Lattice Models.

We are interested in the low-energy physics of solid materials, and consider the material to be clean of imperfections[7], and to form a regular crystal structure. Since the mass of the nucleons exceed the electron mass by multiple orders of magnitude, we may consider a system of dynamic electrons moving in the potential created by a static arrangement of nuclei – the Born-Oppenheimer approximation [15]. We know that core electrons – electrons in filled shells – screen the Coulomb interaction, and do not contribute toward the thermodynamic properties of the system, such properties depend only on the valence electrons. We therefore consider a model consisting

[6] One of the great triumphs of modern crystal growth is the creation of single wafers of silicon to be used in computers, and digital cameras.

[7] Imperfections are, of course, very important in condensed matter physics, for instance the Anderson Impurity Model considers a magnetic impurity in a bath of electrons. The model describes Kondo physics, and is the basis of DMFT calculations.

of valence electrons in the potential created by a set of fixed nuclei at regular lattice sites. The Hamiltonian corresponding to these approximations is

$$H = \sum_{i,j,\alpha,\beta} t_{i,j}^{\alpha,\beta} c_{i,\alpha}^{\dagger} c_{j,\beta} + \sum_{i,\alpha} V_i n_i^{\alpha} + \sum_{\substack{i,j,k,l,\\ \alpha,\beta,\gamma,\delta}} U_{i,j,k,l}^{\alpha,\beta,\gamma,\delta} c_{i,\alpha}^{\dagger} c_{j,\beta}^{\dagger} c_{l,\gamma} c_{k,\delta}. \tag{2.29}$$

Roman indices sum over lattice sites whilst Greek indices sum over orbitals, spin indices have been omitted. $c_{i,\alpha}^{\dagger}(c_{i,\alpha})$ creates(annihilates) an electron at site i in orbital α, $n_i = c_i^{\dagger} c_i$, $t_{i,j}^{\alpha,\beta}$ are elements of the inter- and intra-band overlap integrals between sites i and j, $U_{i,j,k,l}^{\alpha,\beta,\gamma,\delta}$ the interaction between two particles, and V_i is the on-site potential energy term.

Lattice models are a powerful method in condensed matter physics as they simplify complex systems, whilst being able to describe complex phenomena. They offer a way to discretize continuous models for use with numerical methods such a Monte-Carlo, and are realisable via optical lattices, and as such, theoretical predictions may be tested directly.

2.2.1 The Hubbard Model

The single-band Hubbard model which was briefly described in the introduction, makes further approximations to the generic lattice model described above. Firstly interactions are restricted to on-site interactions only, which is a valid approximation, as the core electrons that were 'integrated out' in the lattice model approximation, screen the Coulomb interaction. Furthermore, electron hopping is restricted to nearest-neighbour sites as it is known that overlap integrals drop off rapidly. The

on-site potential energy is dropped, as we assume the electrons are in a constant potential which we may offset as our zero energy. Finally, it considers only a single orbital for valence electrons to reside in, restricting the number of electrons per site to 2. The Hamiltonian for the single-band Hubbard model is,

$$\mathcal{H} = -t \sum_{\langle i,j \rangle, \sigma} \left(c^{\dagger}_{i,\sigma} c_{j,\sigma} + c^{\dagger}_{j,\sigma} c_{i,\sigma} \right) + U \sum_{i} n_{i,\uparrow} n_{i,\downarrow}. \tag{2.30}$$

The Hubbard model is one of the most well known lattice models in the area of condensed matter physics, and is of great interest as discussed in the introduction. In the following section we present some background physics of the Hubbard model which is relevant in chapter 6.

In general the properties of the Hubbard model are dependent on the underlying geometry of the lattice, however certain properties such as metallic or insulating behaviour in the strongly, or weakly correlated regime, depend only on filling, or dimensionality of the system. As such we briefly discuss the well-known properties of the single-band half-filled Hubbard model on a square lattice at finite temperature in the weak, and strong coupling regime, then proceed similarly for the Triangular lattice.

Square Lattice

In the weak coupling regime the hopping term t is much larger than the interaction U, $t \gg U$. This leads to metallic behaviour as it is energetically favourable for electrons to form a Fermi gas. In the weak coupling regime the system is well described by band physics and we may say that the system exhibits a conduction band and

behaves as a standard metal. A direct consequence of small U is the lack of spin ordering, and as such the system is a paramagnetic metal.

In the strong coupling regime the interaction term U is much larger than the hopping term t, $U \gg t$, which reduces hopping of electrons between sites. Quantitative physics is accessible in this regime via application of second order perturbation theory, with t the perturbation parameter – first order corrections vanish. The second order process consists of electrons hopping from site i, to site j, creating a double-occupied lattice site, then hopping back to site i. This reduces the energy by $-t^2/U$. The Pauli exclusion principle restricts same spin species occupying the same site, and as such the system orders such that spins at adjacent sites are anti-parallel to each other, forming an antiferromagnetic state – the Néel state. This second order process is the famous AFM super-exchange, and the physics of the system may be described via the Heisenberg model with an effective exchange interaction $J = 4t^2/U$. In $d \leq 2$ the Mermin-Wagner theorem [16] forbids the formation of true long-range magnetic order[8], however the AFM correlation length is large at low temperatures, and as such quasi-antiferromagnetism(QAFM)[9] occurs. For large interaction strengths, the model is found to be a Mott insulator. Unlike band insulators that are insulating due to the Fermi energy landing 'in-between' bands, this is a purely interaction driven insulating regime. The large energy penalty for doubly occupied sites, causes electrons to 'lock-in' and become localised to lattice sites. The transition from metal to Mott insulator results in a decrease of spectral weight at $\omega = 0$ – the spectral weight indicates the density of available electron states, where a peak in the spectral density at $\omega = 0$ is indicative of the existence of quasiparticles, and Fermi liquid behaviour

[8] The Mermin-Wagner theorem forbids the spontaneous breaking of continuous symmetries in $d \leq 2$ at non-zero temperatures for systems with short range interactions .e.g. the Hubbard Model.

[9] AFM breaks the (continuous) $SU(2)$ spin symmetry

– and the appearance of two satellite peaks, known as the Hubbard bands, as U increases.

The physics in the limit of both large, and small interaction strength, is generally well understood. It is the regime between these limits that is of interest and has led to numerous studies of the Hubbard model. A well-known result is the effect of perfect nesting found at half-filling. The Fermi surface is found to be diamond shaped such that there is a wave vector $\boldsymbol{Q} = (\pm\pi, \pm\pi)$ that connects any point on the Fermi surface to any other point. This surface is plotted in black in the top left of Fig. 2.5. The property of nesting makes the weakly coupled Fermi gas unstable to the formation of the spin density wave with wave vector $\boldsymbol{Q}$ [17], for any $U > 0$. The formation of spin density waves doubles the unit cell, and QAFM occurs [18]. Nesting leads to an enhanced susceptibility at $\boldsymbol{q} = \boldsymbol{Q}$, and the QAFM order can be identified from a peak in the static spin structure factor at $\boldsymbol{Q}$. In the absence of magnetic correlations (DMFT studies) the MIT is expected to be a first-order transition [4]. However, methods that include non-local correlations [19, 20] find a smooth crossover to an insulating state, and even an intermediate non-Fermi liquid state [21], which is corroborated by quantum simulator results [22].

Triangular Lattice

By altering the geometry of the lattice to a triangular lattice, the perfect nesting exhibited on the square lattice is destroyed due to geometric frustration. This destroys the formation of the Néel state at small U values, and the system is metallic for a large range of U. As the interaction strength increases, the system can no longer order with adjacent spins anti-parallel. This is shown on the left of Fig. 2.6, when two spins

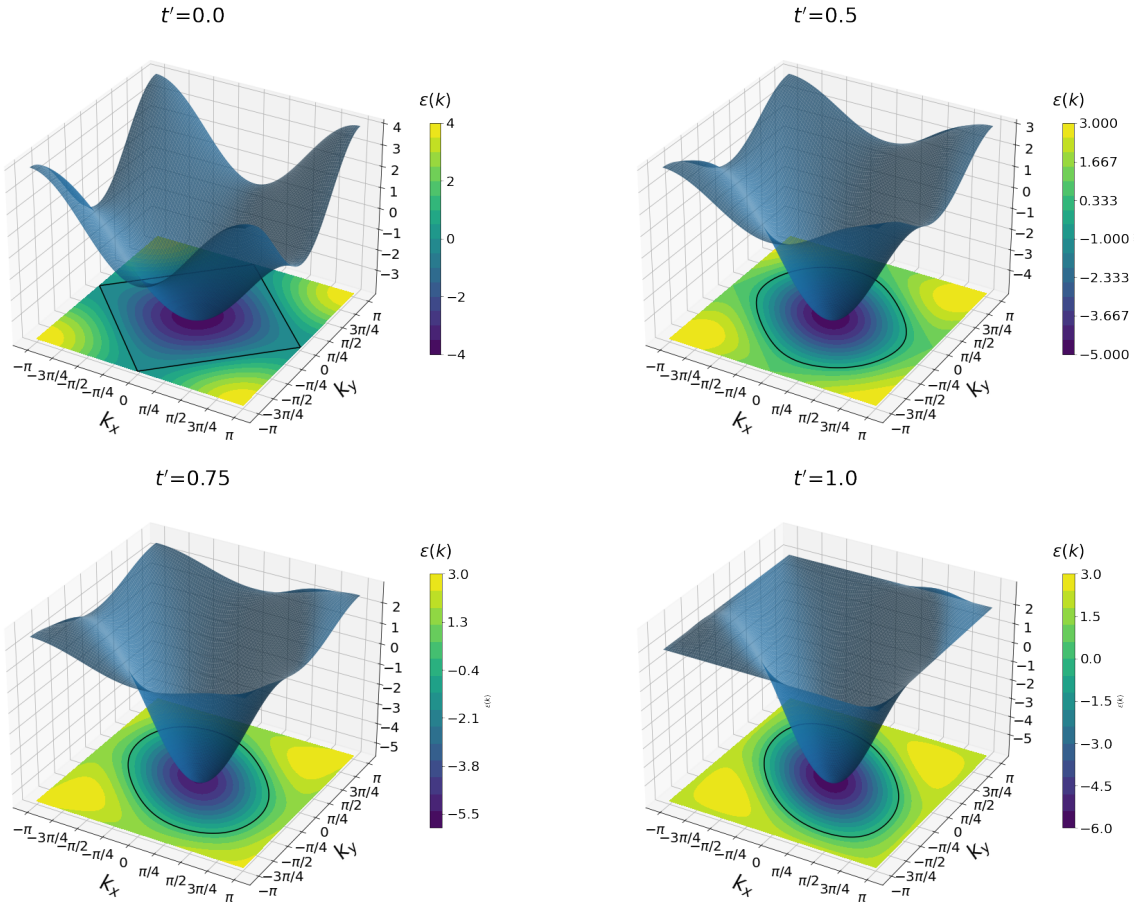


Figure 2.5: Dispersion relations for various values of t' progressing from the square to the triangular lattice. Black contour indicates $\epsilon(k) = 0$.

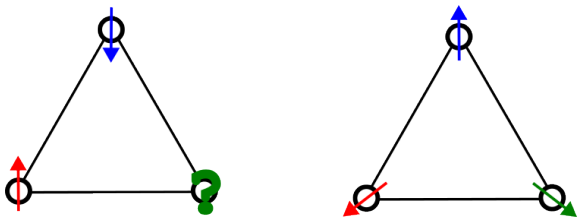


Figure 2.6: Left: depiction of spins aligning anti-parallel to reduce the energy of the system. There is no configuration possible for the all spins to be anti-parallel. Right: at large interaction strengths the three spins form 120° angles between each other, to lower the energy of the system.

have aligned anti-parallel, there is no way to align the third anti-parallel to both. Geometric frustration causes the spins to align at 120° to each other at sufficiently large interaction strengths, as shown on the right side of Fig. 2.6. The 120° QAFM state is indicated by a peak in the static spin structure factor at $\boldsymbol{q} = (2\pi/3, 2\pi/\sqrt{3})$. This high symmetry point is given the label K, and is shown in the bottom right of Fig. 2.7.

In chapter 6 we summarise the current literature, and present results on the metal-insulator crossover, and the corresponding magnetic states of the anisotropic triangular Hubbard model. In the following of this section we discuss the background details for obtaining the results.

We consider a lattice constructed by adding a diagonal hopping term t' from bottom left, to top right of the square lattice. This is shown in the top left of Fig. 2.7. Such a construction translates to the anisotropic triangular lattice – the isotropic triangular case occurs when $t' = t$ – with Hamiltonian

$$\mathcal{H} = -t \sum_{\langle i,j\rangle,\sigma} (c^{\dagger}_{i\sigma} c_{j,\sigma} + \text{h.c}) - t' \sum_{\langle\langle i,j\rangle\rangle,\sigma} (c^{\dagger}_{i\sigma} c_{j,\sigma} + \text{h.c}) + U \sum_{i} \hat{n}_{i\uparrow} \hat{n}_{i\downarrow}, \tag{2.31}$$

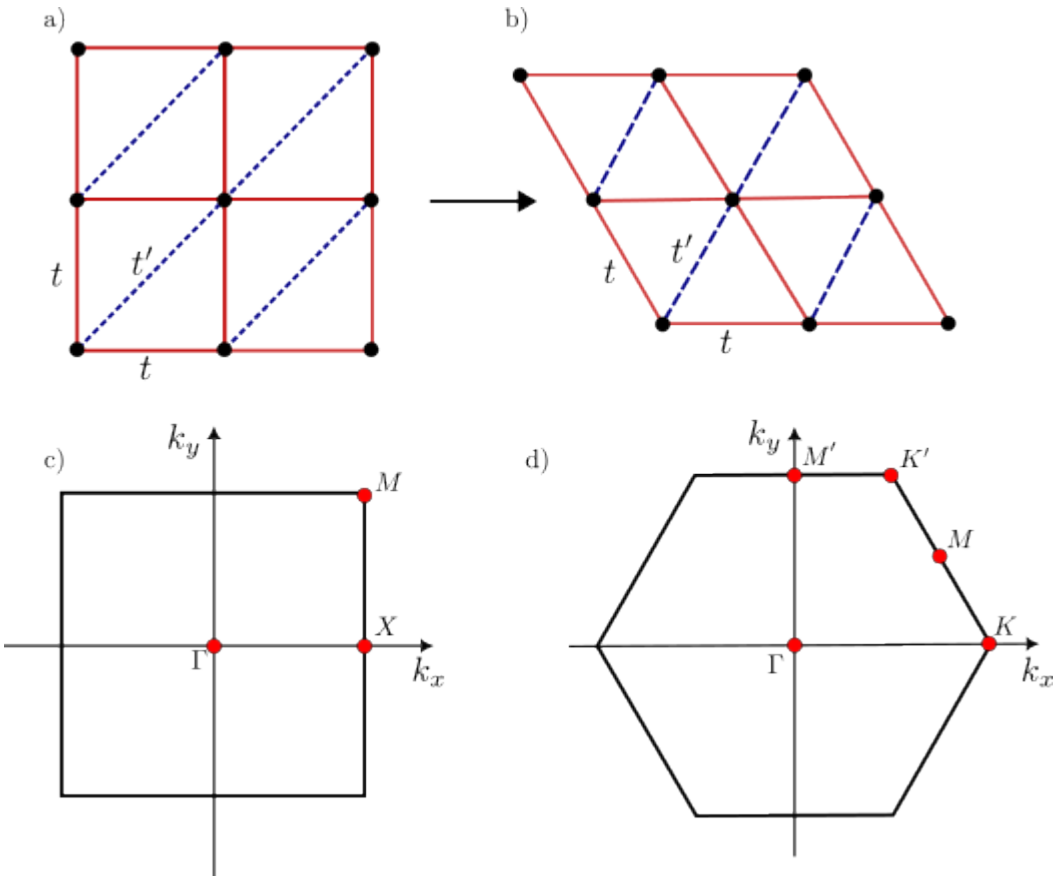


Figure 2.7: a) Basis used for simulations. b) triangular lattice. Arrow between a)-b) represents linear transformation described in text. c) Square lattice Brillouin Zone, with high symmetry points marked by red crosses. d) Triangular lattice Brillouin Zone with high symmetry points marked, with $\Gamma = (0, 0)$, $K' = (2\pi/3, 2\pi/\sqrt{3})$, and $M' = (0, 2\pi/\sqrt{3})$.

where $\langle\langle \dots \rangle\rangle$ indicates the sum over next-nearest neighbours along the bottom left, top right diagonal. When $t' = 0$ this reduces to the square Hubbard model. The model can therefore interpolate between the square and triangular lattice models by tuning t'.

The dispersion relation for several different t' values is shown in Fig. 2.5 with the Fermi surface $\epsilon(\boldsymbol{k}) = 0$, at $\beta \to \infty$ highlighted in black – this occurs at $\mu = 0$ for the square lattice, however, for any non zero t', the density of states is not symmetric around zero, leading to a non-zero chemical potential at half filling in the non-interacting limit. The dispersion relation for the non-interacting model ($U = 0$) is obtained as usual, by summing over lattice vectors, and performing a Fourier transform to momentum space, via $c_k = \frac{1}{\sqrt{n}} \sum_j e^{-ikj} c_j$. The dispersion relation is,

$$\epsilon_{\boldsymbol{k}} = -2(\cos k_x + \cos k_y) - 2t' \cos(k_x + k_y), \tag{2.32}$$

where the lattice constant a, and nearest-neighbour hopping t, have been set to 1. We can directly map onto the triangular BZ by obtaining the lattice points via a linear transformation, which the arrow in Fig. 2.7 represents:

$$\begin{aligned} r'_x &= r_x - 0.5 r_y \\ r'_y &= \frac{\sqrt{3}}{2} r_y, \end{aligned} \tag{2.33}$$

followed by a Fourier transform. Alternatively we may obtain the reciprocal lattice vectors via,

$$\begin{pmatrix} k'_x \\ k'_y \end{pmatrix} = \frac{1}{\sqrt{3}} \begin{pmatrix} 1 & -1 \\ 1 & 1 \end{pmatrix} \begin{pmatrix} k_x \\ k_y \end{pmatrix}, \tag{2.34}$$

with k_x, k_y the components of the square reciprocal lattice vectors.

2.2.2 Observables

The square lattice exhibits particle-hole symmetry, and as such a calculation of the series expansion coefficients, at half-filling for a given temperature, provides results for all U values – provided the series is well behaved, or resummable. For $t' \neq 0$ this is not the case, and the density becomes a function of U. For a fixed t' the density is therefore a function of temperature, coupling strength, and chemical potential, $n(\beta, U, \mu)$. Due to this, the series expansions for observables performed at a fixed chemical potential and temperature, draw out curves in (U, n) parameter space. To obtain results for half-filling we calculate series expansions at different chemical potentials, which cross half-filling at different U values i.e. simulations are carried out at fixed chemical potential, such that density is not a controlled parameter and only known after-the-fact. Firstly, we solve for the non-interacting chemical potential μ_0, via

$$\int \frac{d^2\boldsymbol{k}}{(2\pi)^2} n_F(\epsilon(\boldsymbol{k})) - 0.5 = 0, \tag{2.35}$$

(or equivalently $\int \frac{d^2\boldsymbol{k}}{(2\pi)^2} G_0(\boldsymbol{k}, 0^-) - 0.5 = 0$), where n_F is the Fermi-Dirac function. We then perform simulations at $\mu = \mu_0 \pm m\delta$, with $m \in \mathbf{N}$ and delta some small value that is altered to obtain the desired resolution of crossings. The values of U for which half filling is crossed, are obtained via calculation of the density.

To obtain information on the magnetic state of the system we calculate the static spin structure factor, which is the Fourier transform of the spin correlation function, and given by

$$S(\boldsymbol{q}) = \frac{1}{N} \sum_{i,j} e^{i\boldsymbol{q}(\boldsymbol{r}_i - \boldsymbol{r}_j)} \langle S_i^z S_j^z \rangle, \tag{2.36}$$

where $S_i^z = \frac{1}{2}(\hat{n}_{i,\uparrow} - \hat{n}_{i,\downarrow})$, N is the total number of sites, and $\langle S_i^z S_j^z \rangle$ is the real-space spin correlation function. Peaks in the structure factor are indicative of magnetic

phases. A peak at $M' = (0, 2\pi/\sqrt{3})$ indicates Néel QAFM, whereas a peak at $K = (0, 4\pi/3)$ – and by symmetry, any vertex of the hexagonal BZ, e.g. K' – indicates 120° QAFM. A peak at $M = (\pi, \pi/\sqrt{3})$ indicates collinear antiferromagnetic order [9], where spins are ferromagnetically aligned along one direction of the triangular lattice, and antiferromagnetically aligned along the other two. The position of these high symmetry points are shown in Fig. 2.7. Peaks away from the high symmetry points are considered to be incommensurate magnetic ordering.

Since the metal-insulator transition (MIT) has no single order parameter, we calculate the double occupancy D as a function of U, as it can indicate the presence of a Mott transition [23]. The value of D is expected to decrease as the interaction strength increases, as doubly occupied sites incur an energy penalty U – the MIT may be tracked by other observables such as the spectral function, optical conductivity, or quasiparticle weight. The double occupancy per site is given by,

$$D = \frac{1}{N} \sum_i \langle n_{i\uparrow} n_{i\downarrow} \rangle. \tag{2.37}$$

Calculation of the double occupancy also yields the potential energy of the system via

$$E_{pot} = U \sum_i \langle n_\uparrow n_\downarrow \rangle, \tag{2.38}$$

which should initially increase due to increasing interaction strength, and then decrease upon approach, and into the insulating phase. The kinetic energy is a related observable, as the competition of potential and kinetic energy is a strong indication of the physics occurring. The kinetic energy is given by

$$E_{kin} = -t \sum_{i,j,\sigma} \langle c^\dagger_{i\sigma} c_{j\sigma} + c^\dagger_{j\sigma} c_{i\sigma} \rangle. \tag{2.39}$$

The kinetic energy is negative – hopping lowers the energy of the system – and should decrease in magnitude as interaction increases due to the suppression of doubly occupied sites, and hence hopping.

Furthermore, we calculate the static charge (density-density) correlator which provides information on local ($i = j$) and non-local ($i \neq j$) charge correlations, and is given by

$$C(i-j) = \langle \delta n(i) \delta n(j) \rangle, \tag{2.40}$$

where $\delta n(i) = \sum_\sigma n_\sigma(i) - \langle n_\sigma \rangle$. We may extract the compressibility of the system from the charge correlator via

$$\kappa = \frac{\beta}{N} \sum_{i,j} C(i-j). \tag{2.41}$$

Since we calculate expansion coefficients for multiple densities we also obtain the compressibility by the relationship $\kappa = \frac{dn}{d\mu}$, which we use as a second check.

2.3 Series Resummation

With diagrammatic Monte Carlo we are limited to an expansion order L_{max}, such that we require some resummation techniques to extrapolate the series to infinite order – unless the partial sum has sufficiently converged. We make use of the Padé approximant (PA) [24] to achieve this.

The PA is used to extrapolate power series when only a few terms are known. It may also allow approximations to be found outside the radius of convergence, and

therefore can resum divergent series into convergent ones. The PA is given as the ratio of two series of orders M, and N, such that $M+N+1=L_{max}$, where L_{max} is the order to which the original series is known. The $[M/N]$ approximant is given by

$$P_M^N(x)=\frac{\sum_{m=0}^{M}c_m x^m}{\sum_{n=0}^{N}d_n x^n}, \tag{2.42}$$

where we are free to choose the values M,N under the constraint that $M+N+1=L_{max}$. However, convergence is found to be better for approximations where $M\approx N$, e.g. $M=N$, or $M=N\pm 1$. To perform a PA of a diagrammatic series for the Hubbard model, with coefficients a_n, we obtain c_n, d_n by solving for,

$$a_0+a_1x+\ldots a_nx^L=(c_0+c_1x+\ldots c_Mx^M)/(1+d_1x+\ldots d_Nx^N), \tag{2.43}$$

we may then take the ratio according to Eq.(2.42) to obtain the infinite order approximation. Where for the Hubbard model $x=U$. For certain observables, such as density, the standard PA does not produce reliable results because of the oscillatory nature and/or divergence of the series. We therefore also employ the Dlog-Padé approximant (DPA) [25]. The DPA approximates the logarithmic derivative of a function $f(x)$ via a standard PA. In this way a singularity of the form $(x_i-x)^\gamma$ becomes a simple pole $\frac{\gamma}{(x_i-x)}$. The residue of the pole can then be calculated and incorporated into the resulting approximant, allowing resummation of the divergent series. The PA of the logarithmic derivative is then integrated, and the exponential taken to arrive at the DPA,

$$D_M^N(x)=f(0)+\exp\Big[\int \tilde{P}_M^N(x)dx\Big]. \tag{2.44}$$

Here $f(0)$ is a constant function that reproduces the function at $x = 0$ i.e. the normalisation factor, and $\tilde{P}_M^N(x)$ is the logarithmic derivative of the standard PA. Obtaining the correct error bars for the approximation is somewhat more involved, since we only have one set of series coefficients and variance values. E. Kozik (unpublished work) realised that we may calculate many such approximations by drawing a random set of a_n and corresponding variances from a normal distribution $\mathcal{N}(a_n, a_{n,\mathrm{err}}^2)$, where $a_{n,\mathrm{err}}$ is the measured standard deviation of a_n. By taking the mean of these approximants, we arrive at the final value and variance for the Padé approximant. To improve upon the results obtained via the approximant, we follow Ref. [26] and perform the PA/DPA for $N \approx M$, $N < M$, and $N > M$ (where possible) and take the average of the three results. For an approximant that we can trust, the results for different values of $[M/N]$ should agree closely.

Chapter 3

Diagrammatic Monte-Carlo

Diagrammatic Monte Carlo (DiagMC) is a technique to stochastically sample Feynman diagrams via a Markov chain. DiagMC is a powerful technique for investigating strongly correlated systems, so much so, that there are now multiple iterations of the technique. This thesis is mainly concerned with "classical" DiagMC where diagrams are "drawn" and sampled. However, we also present results from connected determinant diagrammatic Monte Carlo (cDet) simulations, which will be described, albeit in less detail.

DiagMC was first applied to the polaron problem in 1998 [27]. It was then brought in to the realm of fermionic many body theory by Van Houcke *et al.* [28] in 2008, where it was applied to both the Hubbard model, and later the resonant fermi gas [29, 30]. Since then it has been applied to many problems on the Hubbard model [31–35], including magnetic instabilities [26, 36], and the BEC-BCS [37] transition. Moreover DiagMC has played a large role in the comprehensive numerical study of the Hubbard model found in Ref. [17]. A popular technique is the bold-DiagMC scheme

in which skeleton diagrams[1] – skeleton diagrams are the set of all 1PI diagrams – formed via dressed propagators are summed [38], however much care is needed when performing such summation as Ref. [39] has shown that the skeleton expansion can converge to un-physical answers for Hubbard models.

Determinant Diagrammatic Monte Carlo (DDMC) was proposed by Rubstov *et al* [40], this method calculates the determinant of a Green's function matrix, in real space, via principal minor calculations. The determinant calculation of the Green's function is equivalent to calculating the contribution from all possible diagrams, both connected and disconnected. Calculation of disconnected diagrams inhibits extrapolation to the thermodynamic limit (TL), since disconnected pieces that have very large separation contribute to the overall weight. Development of a recursive procedure, by Rossi [41], to systematically remove all disconnected diagrams extended this technique for use in the thermodynamic limit. This extension is aptly named connected determinant diagrammatic Monte Carlo (cDet). cDet complexity scales with diagram order better than DiagMC, by boasting exponential computational time, rather than factorial, which is one of its main advantages. However cDet is not as versatile and much care is needed to consider different types of interactions, e.g. delta-function, or Coulomb.

Haule & Chen have developed a variational DiagMC approach by optimizing the starting Lagrangian, alongside grouping diagrams into "sign-blessed" groups, and calculating the resulting integrals via standard Monte Carlo techniques. This method has seen success in calculating the exchange correlation energy for the uniform electron gas, which is required for DFT calculations [42].

There is also another interesting method, whilst not strictly diagrammatic Monte

[1] Mattuck [7] describes skeleton diagrams as diagrams that have been renormalized by putting self-energy flesh on the bones.

Carlo, it is very closely related. This goes by the name Algorithmic Matsubara Integration [43, 44], where diagrams are categorized according to the structure of their poles in frequency space, which is represented by some binary array structures. The Matsubara summations for multiple diagrams – with the same pole structure – are then carried out in a single run, since the result only depends on the structure of the poles. This leaves the momentum integrals to be completed which is then carried out by Monte Carlo methods.

The methods briefly described above follow a different ethos than "classical" DiagMC i.e. they organise diagrams prior to calculating, and therefore they do not fit into the regime of our code. While such approaches can reduce the computational complexity, and allow one to access more challenging physical regimes, here we maintain a more basic approach.

A key aspect of "classical" Diagrammatic Monte Carlo is that it is automatically in the thermodynamic limit, and therefore we see no finite size scaling effects. The only approximation that is made is the extrapolation to infinite order, for which there are some sophisticated techniques that can be applied e.g. the Páde approximant described in section 2.3. Another key aspect is that the dimension of the system we wish to investigate does not alter the algorithm. In practice this means we can investigate either 2d, or 3d systems without any extra overhead – except for some computational time for the extra momentum component – since this only amounts to using a different dispersion relation to calculate the non-interacting Green's function. These two aspects of the technique allow for application to a wide array of systems, and allow numerically exact investigations of regimes that is not possible with techniques such as DMFT, in which including non-local correlations is a challenge. This is somewhat dealt with by cluster DMFT [45], however cluster sizes are

still limited due to the exponential scaling of complexity with cluster size, which cannot be systematically improved upon.

3.1 Classical Diagrammatic Monte Carlo

In this section we discuss the details of Diagrammatic Monte Carlo, which employs a complex set of updates to sample the series of one-particle(two-particle) irreducible Feynman diagrams in order to sample the self-energy(vertex function) of a system. This can then be used in Dyson's(Bethe-Salpeter) equation to obtain the fully interacting Green's function, and thermodynamic properties of the system.

3.1.1 Markov Chain Diagrammatic Monte Carlo

The goal of Diagrammatic Monte Carlo is to sample a diagrammatic series stochastically. In an abstract sense we may write the diagrammatic series as [28],

$$Q(Y) = \sum_{m=0}^{\infty} \sum_{\mathcal{T}_m} \int \mathcal{D}(\mathcal{T}, Y, X_1, \ldots, X_m) dX_1, \ldots, dX_m \tag{3.1}$$

Where m denotes diagram order, and $\mathcal{T}_m$ denotes a given topology at order m. $\mathcal{D}$ is a diagram of a given topology $\mathcal{T}$, at order m, with external variables Y, and internal variables X. Such an expression cannot be solved analytically, therefore we sample via Markov Chain Monte Carlo (MCMC). We define a configuration as a diagram topology with fixed values for all variables X, and Y, i.e. $\mathcal{C} = (\mathcal{T}_m, X, Y)$. We implement an algorithm with a set of updates which takes configuration $\mathcal{C}_i$ to

configuration $\mathcal{C}_j$. Where $\mathcal{C}_j$ may differ from $\mathcal{C}_i$ due to a change in Y, a change in some internal variables X, a change in $\mathcal{T}_m$, or a combination of these. We point out that changes in configurations can alter the external momentum giving arbitrary momentum precision. Repeated application of the updates produces a Markov chain, which explores the configuration space in all dimensions: X, Y, and $\mathcal{T}_m$.

A Markov chain is a random walk through configuration space, produced by repeated application of updates, such that at any step n the current configuration $\mathcal{C}_n$ only depends on the previous configuration $\mathcal{C}_{n-1}$ i.e. the process is memoryless.

The transition for this process is given by a transition matrix

$$P(\mathcal{C}_n = j|\mathcal{C}_{n-1} = i) = P_{ji}. \tag{3.2}$$

The transition matrix P has the properties $P_{ji} \geq 0$, and $\sum_j P_{ji} = 1$, i.e. it is a stochastic matrix. The Markov chain starts with some initial configuration $\mathcal{C}_0$, drawn from a random initial distribution, which corresponds to a distribution vector p_{i_0} with the properties

$$0 \leq p_{i_n} \leq 1, \tag{3.3}$$

$$\sum_i p_i = 1. \tag{3.4}$$

Applying an update to this initial state is equivalent to multiplying on the left by the transition matrix, such that we obtain the $n = 1$ state,

$$p_j = \sum_i P_{ji} p_{i_0}, \tag{3.5}$$

where P_{ji} is the element of $\boldsymbol{P}$ on the jth row and ith column.

This represents a memoryless chain, where we may obtain the nth state by application

of P n times on the original distribution vector

$$p_{j_n} = \boldsymbol{P}^n p_{i_0}. \tag{3.6}$$

If the set of updates is ergodic – ergodicity is the statement that any state should be accessible in the configuration space in a finite number of updates – the distribution vector will converge to a stationary probability distribution.
We must therefore define a set of updates such that the stationary distribution coincides with the target distribution, which requires adherence to the detailed balance equation. Detailed balance states that a transition from one state to another, should be equal to the inverse transition. More generally for a stationary distribution π, we find

$$P_{ji}\pi_i = P_{ij}\pi_j, \tag{3.7}$$

which is a specific choice of the more general *global balance* condition

$$\sum_j P_{ji}\pi_i = \sum_i P_{ij}\pi_j. \tag{3.8}$$

However, detailed balance is a sufficient condition to ensure ergodicity, so long as we do not introduce periodic cycles to our Markov chain, which is handled by the Metropolis-Hastings algorithm and, therefore, not an issue.

Metropolis-Hastings Algorithm

The Metropolis-Hastings algorithm is a Markov chain algorithm that ensures detailed balance is adhered to, and also prevents periodic loops occurring by allowing

transitions $p_i = P_{ii}$, i.e. rejection of a move, to obtain the same configuration – which must be counted each time. It is perfect for such a system where direct sampling cannot be achieved, since the exact probability distribution is unknown.
To derive the algorithm we re-write the detailed balance equation as

$$\frac{P_{ji}}{P_{ij}} = \frac{\pi_j}{\pi_i}. \tag{3.9}$$

We then write the transition probability as two factors: the proposal distribution, and the acceptance distribution. The proposal distribution is the probability to propose state j given state i, denoted $\mathcal{P}_{ji}$, and the acceptance distribution is the probability to accept the newly proposed state j, denoted $\mathcal{A}_{ji}$ such that

$$P_{ji} = \mathcal{P}_{ji}\mathcal{A}_{ji}, \tag{3.10}$$

where we use the short-hand notation $\mathcal{P}_{ji} = \mathcal{P}(j|i)$, and $\mathcal{A}_{ji} = \mathcal{A}(j|i)$. Substituting these into the detailed balance equation we may express the ratio of the acceptance probabilities, $\mathcal{A}_R$, as

$$\mathcal{A}_R = \frac{\mathcal{A}_{ji}}{\mathcal{A}_{ij}} = \frac{\pi_j \mathcal{P}_{ij}}{\pi_i \mathcal{P}_{ji}}. \tag{3.11}$$

Detailed balance is then ensured by taking,

$$\mathcal{A}_{ji} = \min(1, \frac{\pi_j \mathcal{P}_{ij}}{\pi_i \mathcal{P}_{ji}}) = \min(1, \mathcal{A}_R). \tag{3.12}$$

The implementation of the Metropolis-Hastings algorithm for diagrammatic Monte Carlo, in general, follows these steps,

- Define initial diagram labelled as configuration $\mathcal{C}_0$.

- Propose an update to alter the diagram, such that $\mathcal{C}_0 \to \mathcal{C}_i$
- Calculate the acceptance probability, which amounts to the product of the ratio of the proposal probabilities for the forward, and reverse move, and the ratio of the new diagram weight, with the previous diagram weight.
- If the acceptance ratio is ≥ 1, accept the move.
- If the acceptance ratio is < 1, draw a random number $r \in [0, 1]$, and accept with probability r.

For implementation of the DiagMC specific algorithm in momentum space, we require a relatively large number of distinct MC moves to explore the configuration space.

Diagram Representation

Whilst the implementation details are described in the next chapter, the way in which diagrams are encoded for sampling is required to understand the Monte-Carlo updates, and we therefore discuss this now. Furthermore, the number of slots, and therefore propagators entering, and leaving a vertex is not hard-coded, however the updates are discussed in the context of vertices with four slots($n_v = 4$) to simplify the explanations.

Diagrams are made up of a combination of propagator lines and vertices [6]. We wish to calculate one- or two-particle Green's functions, by sampling either two- or four-point diagrams. These correspond to diagrams with two open ends, and four open ends respectively. However, from an algorithmic perspective it is easier to close the diagrams by implementing a *measurement line* [28], which connects the two open

ends for two-point diagrams, or, a *measurement vertex* for four-point diagrams. The measurement line(vertex) holds the external variables Y (see Eq. (3.1)), and weight of the diagram, which are used for recording measurements.

When simulating diagrams we represent propagators abstractly such that we store the origin, destination, propagator type e.g. normal or anomalous, and the momentum associated with the line. From this data we can calculate all properties required. We represent vertices as a vertex object containing $n_v = 4$ slots: two incoming, and two outgoing. We store the position of each slot – position represents $(\boldsymbol{r}, \tau)$, or τ when working in $(\boldsymbol{R}, \tau)$ or $(\boldsymbol{k}, \tau)$ space respectively – along with the corresponding quantum numbers at the slot, e.g. the spin of the propagator line entering the slot. We take the convention that the incoming slots are on the left of the vertex labelled 0 (top left) and 2 (bottom left) and the outgoing slots are on the right of the vertex labelled 1 (top right) and 3 (bottom right) - see Fig. 3.1. We also take the convention that the interaction line runs from the top, to the bottom of the vertex. Two possible internal connections are shown in Fig. 3.2. However, the interfaces implemented in our code allow for this to be altered by redefining the slot arrangements. This is done by simply defining a derived class to the *Generic Vertex*, with the desired slot definitions.

Propagator connectivity is implemented in the following fashion; as mentioned above, all vertices are given four slots labelled $[0, 3]$, each vertex is also given a unique label in the range $[0, N-1]$, where N is the maximal order of the diagram. The slots of the vertex are also given a location variable, which in the case of a 4-slot vertex is obtained by `(label << 2 + slot No.)`, where `x << n` is the left bit shift operator acting on x, equivalent to $2^n x$. Each vertex then holds the values corresponding to the locations where the outgoing(incoming) propagator ends(begins). Using the location, we can obtain the corresponding slot via a bit mask operation `(location & 0x3)`.

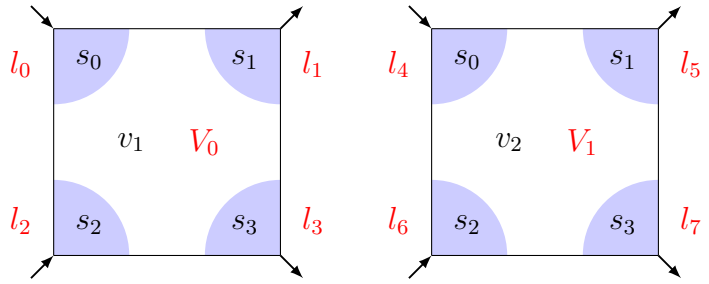


Figure 3.1: Schematic of labelling conventions used for the Hubbard model, more specifically two vertices numbered $1, 2$. s_n denotes a slot number, v_m the vertex number, $V_l = v_m - 1$ the vertex label, and l_k the absolute location in the diagram.

We keep a table of vertex objects holding all the relevant information regarding the current diagram. Monte Carlo updates then alter the diagram by changing the fields in the vertex objects. Fig. 3.3 shows how the diagrams in Fig. 2.2 are represented in our code.

As an example consider a first-order diagram with an instantaneous interaction

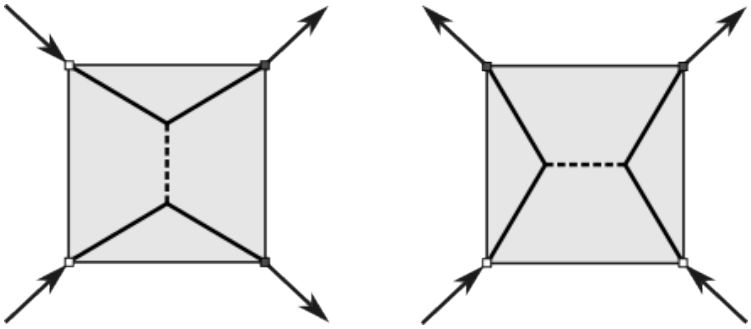


Figure 3.2: Two possible ways to internally connect a vertex. Vertex slots are indicated as white squares for incoming lines, and grey squares for outgoing lines. We use the connections shown on the left.

in imaginary time, along with its representation in the code, shown in Fig. 3.4 – this is a tadpole diagram which has zero momentum dependency, and as such it contributes a constant value to the self-energy. The diagram represents the Hartree term Un_σ, where U is the interaction term, and n_σ is the spin density. There are

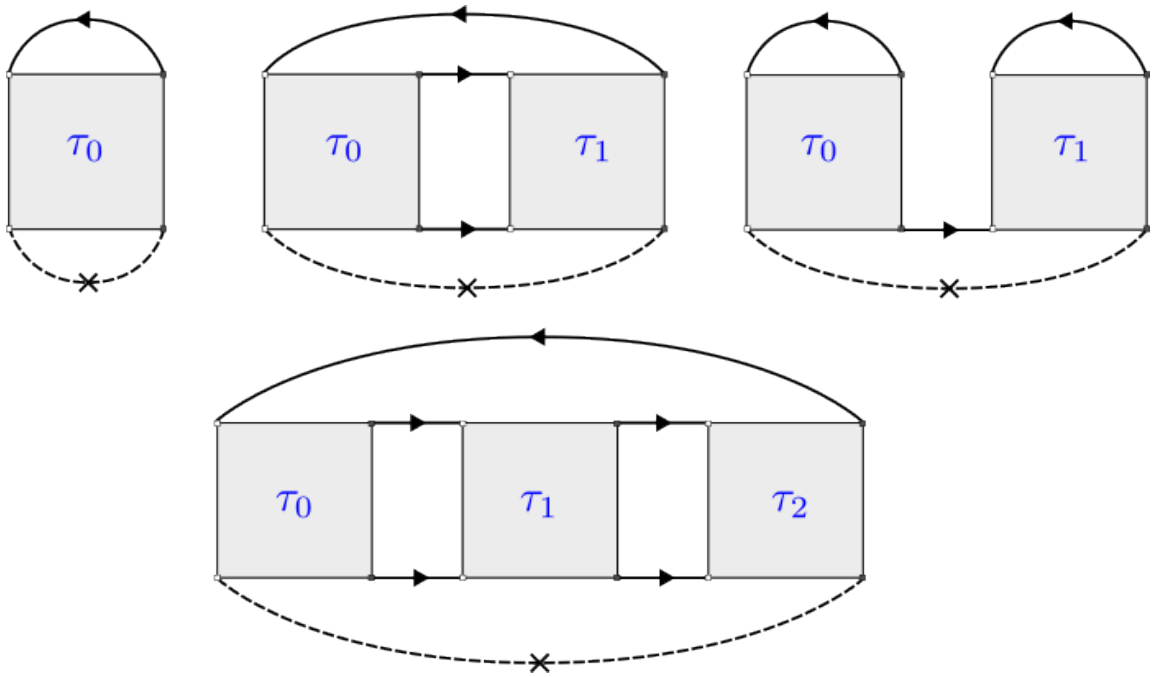


Figure 3.3: The same diagrams as shown in figure 2.2 as represented in our code. The dashed line indicates the measurement line which closes the diagrams. For brevity only one τ label is added, however each slot may have a different τ value associated with it, depending on the theory.

two propagators, where the dashed line represents the measurement line. We may therefore represent the diagram with a single vertex object, and a measurement line. The vertex has the following properties,

```
1  Momenta = [l, l, k, k]
2  Positions = [τ1,τ1,τ1,τ1]
3  PropagatorData = [G0(l,0),G0(l,0),G0(k,0),G0(k,0)]
4  VertexFunction = U
5  QNbrs = [1,1,0,0]
6  Connections = [l1,l0,l3,l2]
```

Where vectors of length four are indexed by the slot numbers $[0-3]$. For the spin

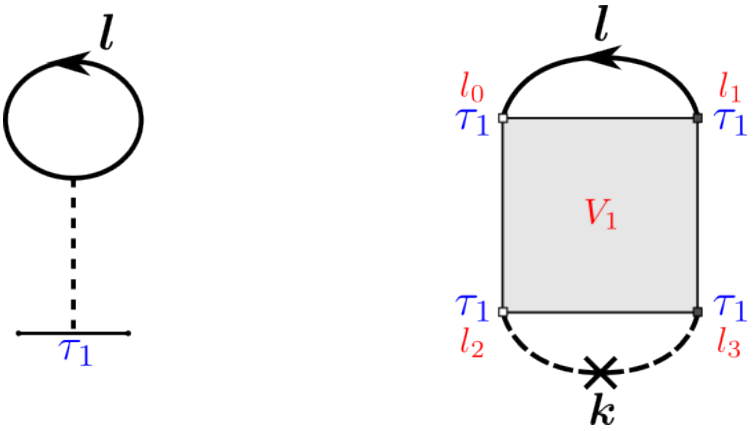


Figure 3.4: Comparison of first order diagram drawn in the standard fashion (without external propagators), and depiction of our abstract representation used in simulations.

quantum numbers, $1 = \uparrow$, and $0 = \downarrow$. The measurement line holds extra data for recording observations such as the diagram weight. However, in terms of the diagram, it holds the momentum, positions, and quantum numbers of the line(vertex). For the tadpole it would hold the following values:

```
Momentum = [k,0,0,0]
Positions = [τ1,τ1,τ1 − τ1,0]
QNbrs = [0,0,0,0]
```

Where a measurement line can be described by a single momentum (four components for a measurement vertex), the start and end positions in imaginary time, along with the imaginary time difference, and the spin of the line – this is represented by two numbers as a generic case must consider spin flip processes.

In summary, a vertex is represented by a box with two incoming and two outgoing slots. Propagators are defined by their start and end positions, and the diagram,

which is just the 1PI part, is closed via a measurement line which holds the external parameters Y.

3.1.2 Sectors

At first sight, adhering to momentum conservation looks to cause complications for defining efficient updates. If we were to always adhere to momentum conservation, we would have to alter the whole diagram simultaneously, making all updates very costly, especially at higher orders. By defining sectors, and allowing the diagram to traverse these sectors, we may break momentum conservation and create non-physical diagrams. This allows us to define local, less costly updates to explore the configuration space[2]. This is possible thanks to the worm algorithm [46]. The sectors we have implemented, following in the spirit of V. Houcke *et al.* [30] are:

- Sigma Sector, Σ – This sector consists of all connected irreducible diagrams, e.g. all 1-particle irreducible diagrams that contribute to the single particle properties of the system.
- Normalisation Sector, $\mathcal{N}$ – This sector consists of all diagrams in the set $\mathcal{S}_{\mathcal{N}}$, which depends on the normalisation method used.
- Worm Sector, $\mathcal{W}$ – This sector consists of all connected irreducible diagrams that have a worm line. The worm line allows for local momentum conservation whilst violating physical momentum conservation.

[2]Local updates can be thought of analogously to flipping a single spin in an Ising model Monte Carlo simulation, rather than updating all spins.

- High Order Sector, $\mathcal{H}$ – All diagrams with $N > 1$ are in this sector, where N is the number of interaction vertices present, or equivalently the diagram order. It is used as a way to trivially decline calls to enter norm, since we pick the convention that the norm diagram is of order $N = 1$, and we may not enter this configuration from any order greater than 1.

Certain updates will change the sector of the diagram, whilst others will not, e.g. *Enter Norm* takes the diagram from the physical sector Σ , into the norm sector $\mathcal{N}$. Our implementation optimizes the proposal of moves, such that we never propose moves that will be trivially rejected in a given sector. Note that only diagrams in the Σ sector are measured, and contribute to the self energy.

3.1.3 Updates

In this section we discuss the ergodic – actually, over complete – set of updates implemented in our code base, which follow that of [28, 30, 47]. This discussion describes the 'standard' set of updates, whereas in chapter 4 the implementation specific changes for updates are described. The updates are described in terms of their probabilities and the calculation of their acceptance ratio according to the Metropolis-Hastings algorithm. Examples of updates are given for diagrams in the context of the Hubbard model, as the interaction vertex is momentum independent and somewhat simplifies the update explanations. Moreover, benchmark data has been obtained for the Hubbard model on a square lattice (see chapter 5), and the specific examples have been implemented and tested.

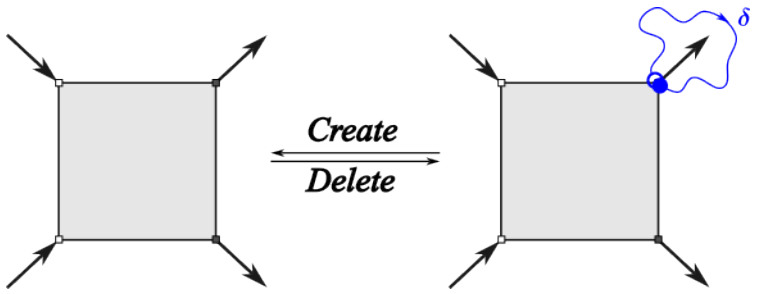


Figure 3.5: Depiction of the configuration change caused by the *Create/Delete worm* update.

Create/Delete Worm

The worm algorithm introduces an extra feature to the Feynman diagrams and, in doing so, increases the configuration space via the addition of the worm sector, as described above. The worm itself consists of two ends labelled Ira($\mathcal{I}$) and Masha($\mathcal{M}$)[3], attached together via a 'virtual string' carrying momentum $\boldsymbol{\delta}$. By moving one end of the worm across a vertex, or propagator, the momentum is altered by $\pm\boldsymbol{\delta}$ causing a local violation of momentum conservation. When the worm ends meet up again i.e. reside on the same slot of a vertex, there is a chance to delete the worm, which returns the diagram back to the physical sector, and ensures conservation of momentum is adhered to. All updates that alter a worm are trivially rejected when the diagram is physical i.e. when there is no worm present. The *Create Worm* update creates a pair of worm ends on a single slot of one of the available vertices as depicted in Fig. 3.5. We have a choice of $\mathcal{P}_C = 1/(4N)$ places to create the worm by picking one of the 4 slots, from N vertices. However exchanging $\mathcal{I}$ and $\mathcal{M}$ along with $\boldsymbol{\delta} \to -\boldsymbol{\delta}$ reduces the number of configurations by half, hence the choice becomes to $\mathcal{P}_C = 2/(4N)$. The momentum carried by the worm is drawn from a probability distribution $P_{\boldsymbol{\delta}}$. The probability distribution from which $\boldsymbol{\delta}$ is drawn, will vary depending on the the-

[3]These are named after N. Prokof'ev's daughters!

ory, e.g. for a centrosymmetric continuum model we may draw $\boldsymbol{\delta}$ in a sphere around the origin with decreasing weight as the magnitude of $\boldsymbol{\delta}$ gets larger, or with a uniform weight up to some cutoff. Whereas for a lattice theory it makes sense to draw $\boldsymbol{\delta}$ from the first Brillouin zone (BZ). The creation of a worm is associated with a weight parameter C_w, which is used to tune the number of un-physical diagrams by altering the acceptance ratio. The *Delete Worm* update simply removes the worm from the diagram if both $\mathcal{I}$ and $\mathcal{M}$ occupy the same vertex slot, with $\mathcal{P}_D = 1$. The *delete* update is rejected if the two worms do not occupy the same slot on the same vertex. The deletion of the worm moves the diagram from the worm sector to the physical sector. From the discussion on the Metropolis-Hastings algorithm we find the acceptance ratio of the create update to be

$$\mathcal{A}_{R_{CW}} = \frac{2NC_w}{P_{\boldsymbol{\delta}}}, \tag{3.13}$$

with the *Delete* update its inverse.

In practice for the Hubbard model, we draw $\boldsymbol{\delta}$ from a uniform distribution over the BZ, $P_{\boldsymbol{\delta}} = U([-\pi, \pi]^d)$, with a circle of radius $r = k_{\min}$ removed – The removal of vanishingly small worm momentum avoids the creation of disconnected graphs. We set the associated worm weight as $C_w = \frac{1}{4N(2\pi)^d}$, where d is the dimension of the model, to spend more time in the physical sector at higher orders, as many more measurements are required due to the number of internal diagram parameters.

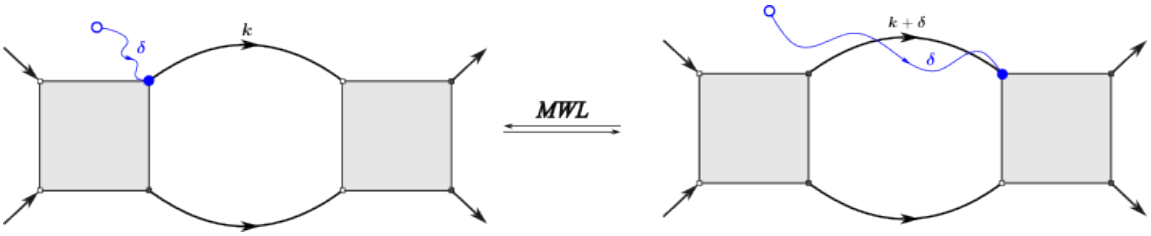


Figure 3.6: Depiction of the change in momentum of a propagator line as the worm is moved across it.

Move Worm Across Line

The *Move Worm Across Line* update moves one end of the worm across the propagator connected to the same slot as the worm end resides, altering the propagator's momentum as depicted in Fig. 3.6. This update has a proposal ratio of $\mathcal{P} = 1/2$, since we may move either end of the worm across the line. The update is self complementary, such that the proposal ratio of $\mathcal{P} = 1/2$ is cancelled out by the conjugate update. The weight ratio is given by the ratio of the propagator value after moving the worm, $G(\boldsymbol{k}')$, and the propagator value prior to moving the worm $G(\boldsymbol{k})$, where the temporal index has been suppressed since it is not altered. The new momentum of the line is given by $\boldsymbol{k}' = \boldsymbol{k} + s_w s_d \boldsymbol{\delta}$, where s_w is $+1(-1)$ if we move $\mathcal{I}(\mathcal{M})$, and $s_d = +1(-1)$ if we move with(against) the direction of the propagator. The acceptance ratio for this update is

$$\mathcal{A}_{R_{MWL}} = \frac{G(\boldsymbol{k}')}{G(\boldsymbol{k})}. \tag{3.14}$$

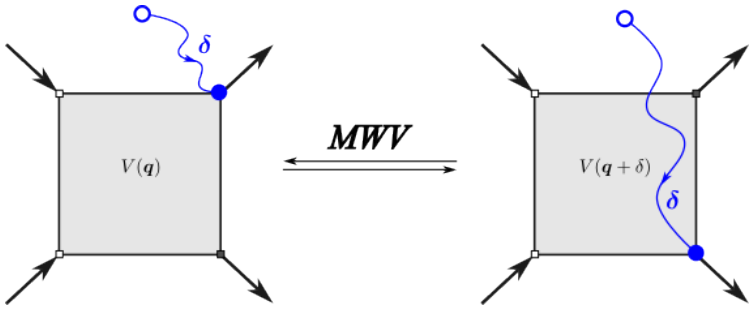


Figure 3.7: Depiction of the change in momentum of a vertex as the worm is moved across it vertically.

Move Worm Vertically Across Vertex

The *Move WormVertically Across Vertex* update moves one end of the worm from the upper(lower) to the lower(upper) slots of the vertex, e.g. from slot 1 to slot 3, as depicted in Fig. 3.7. This will, in general, depend on the specifics of the vertex, however the momentum change will be $\boldsymbol{q} \to \boldsymbol{q}' = \boldsymbol{q} + s_w s_d \boldsymbol{\delta}$, where s_w is defined as above, and $s_d = +1(-1)$ for a downward(upward) move. The definition of s_d also depends on the direction of the momentum transfer, however as stated earlier we fix this to be from the upper to lower part of the vertex. The update is self complementary reducing the proposal ratio to $\mathcal{P} = 1$, such that the acceptance ratio is given by

$$\mathcal{A}_{R_{MWV}} = \frac{V(\boldsymbol{q}')}{V(\boldsymbol{q})}. \tag{3.15}$$

For the Hubbard model the vertex is momentum independent, such that $V(\boldsymbol{q}') = V(\boldsymbol{q})$, and the move is trivially accepted with $\mathcal{A}_{R_{MWV}} = 1$

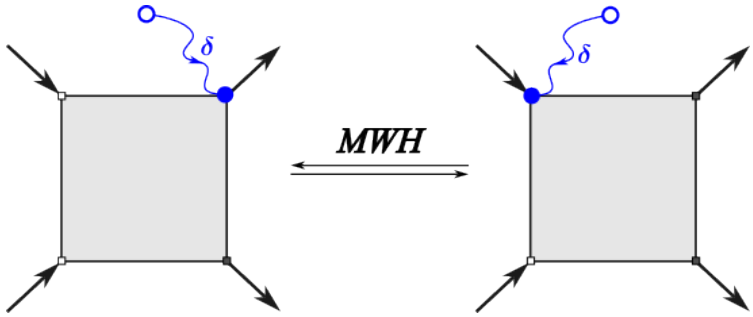


Figure 3.8: Depiction of the change in momentum of a vertex as the worm is moved across it horizontally.

Move Worm Horizontally Across Vertex

The *Move Worm Horizontally Across Vertex* update moves one end of the worm across the vertex that it resides, e.g. from slot 1 to slot 0, as depicted in Fig. 3.8. If the vertex depends on the incoming and outgoing momentum, the vertex value will be altered. In general the momentum dependence of the vertex will depend on the vertex type, and the acceptance ratio will follow that of the *Move Worm Vertically Across Vertex* update. However, defining the interaction to go from the upper to the lower part of the vertex makes this update trivial, and with the slot conventions taken here, this update has no effect on the vertex. The Hubbard vertex value is independent of the momentum carried across the vertex, therefore, since this update is self complementary, it is trivially accepted with $\mathcal{A}_{R_{MWH}} = 1$

Shift Vertex Position

Although not necessary for ergodic sampling, the *Shift Vertex Position* update picks a random slot(s) of a vertex and moves its position(s), this is depicted in Fig. 3.9. In $\boldsymbol{k}, \tau$ space this corresponds to altering the τ value of the given slot(s). However,

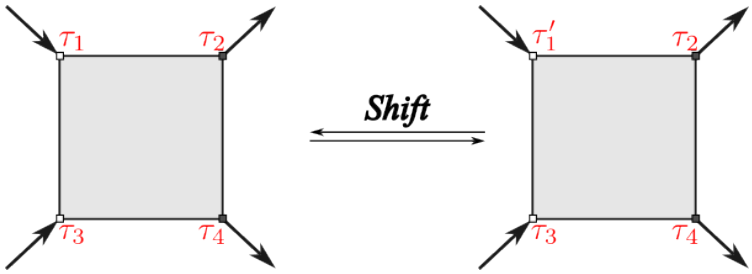


Figure 3.9: Depiction of the configuration change when the *Shift Position* update is performed on the upper incoming slot labelled τ

in $\boldsymbol{r}, \tau$ this could correspond to moving both spatial and temporal positions. The update picks a slot(s) of a vertex, out of N vertices, and a new position from some distribution P_p, such that the proposal probability is $\mathcal{P} = P_p/(4N)$. However, this move is self complementary, and the proposal ratio reduces to $\mathcal{P} = 1$. The propagator(s) connected to the affected slot(s) are recalculated, and the weight is given by the ratio of the new vertex value and propagator values, with the old vertex value and propagator values. Defining s_i as a shifted slot, n_s as the number of affected slots, and G_{s_i} as the propagator connected to that slot, the acceptance ratio for a generic vertex is,

$$\mathcal{A}_{R_{SV}} = \frac{\prod_i^{n_s} G_{s_i}(\tau')}{\prod_i^{n_s} G_{s_i}(\tau)} \frac{V(\tau')}{V(\tau)}, \tag{3.16}$$

where τ' is the newly drawn imaginary time value, and τ the original value.

The Hubbard model interaction is a delta function in time, such that this update moves all vertex slots i.e $n_s = 4$. The vertex value is unaffected, however all four propagators require recalculating, leading to an acceptance ratio

$$\mathcal{A}_{R_{SV}} = \frac{\prod_{i=0}^{3} G_{s_i}(\tau')}{\prod_{i=0}^{3} G_{s_i}(\tau)}. \tag{3.17}$$

This update is computationally expensive when compared to other updates. Due to this we, extend the optimized drawing of a vertex time proposed by Gukelberger [47]

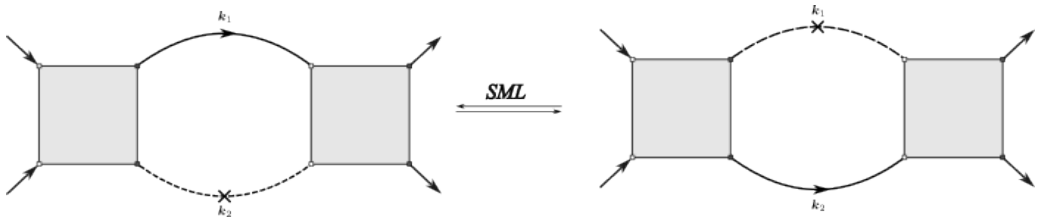


Figure 3.10: Depiction of the configuration change when sampling two-point diagrams, caused by the *Swap Measurement* update.

– discussed at the end of the updates section – to this update. However, since this update is not required for ergodicity, we call it with a low probability to improve computational efficiency.

Swap Measurement

The *Swap Measurement* update swaps the measurement line(vertex) with one of the physical propagators(vertices). An example of a line swap is shown in Fig. 3.10. Since we can sample with either a measuring propagator, vertex, or both – not simultaneously – we must decide which type of object to swap. We treat vertices and propagators with equal weights, and choose an object via the generation of a uniform random number. The move is self-complementary, therefore the proposal ratio is $\mathcal{P} = 1$. The weight, and therefore acceptance ratio, is

$$\mathcal{A}_{R_{SM}} = \frac{F_{new}}{F_{old}}, \tag{3.18}$$

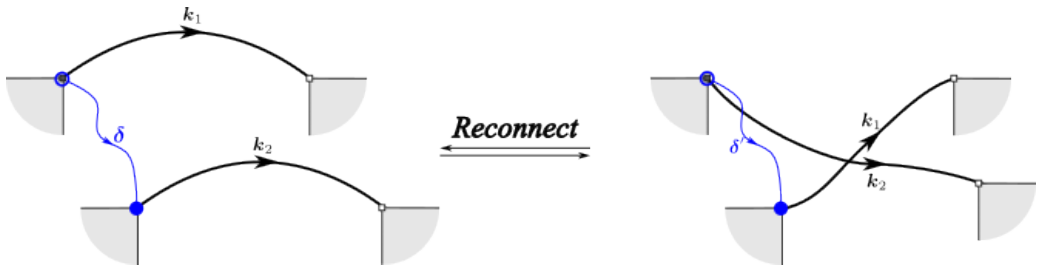


Figure 3.11: Depiction of configuration change caused by the *Reconnect* update. Only the corner of the vertices that are involved are shown for clarity.

where F represents either a measurement line or measurement vertex. For two-point diagrams in the Hubbard model, we use a measurement line, and therefore

$$\mathcal{A}_{R_{SM}} = \frac{G_{new}}{G_{old}}. \tag{3.19}$$

When sampling an un-polarised system we may safely turn the *swap measurement* update off without breaking the ergodicity requirement, since $\Sigma_{\uparrow\uparrow} = \Sigma_{\downarrow\downarrow}$. However, this update is necessary when sampling self-energies in a polarized system.

Reconnect

The *Reconnect* update selects two propagators connected to slots where the worm ends reside, and swaps their ends, as shown in Fig. 3.11. This update is the only update that alters the number of fermionic loops in the diagram, and is therefore required for ergodicity. It must be carried out in the worm sector as swapping two lines will result in breaking momentum conservation, and therefore the update is trivially rejected in the physical sector. When swapping the connections of the lines, the worms momentum must alter by the difference between the two propagator

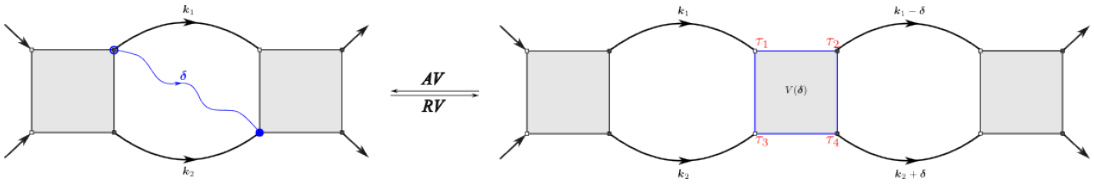


Figure 3.12: Depiction of configuration change caused by the *Add/Remove* update. The newly added vertex is highlighted in blue for clarity.

momenta. Therefore $\boldsymbol{\delta} \to \boldsymbol{\delta}' = s_d(\boldsymbol{k} - \boldsymbol{k}')$, where $\boldsymbol{k}(\boldsymbol{k}')$ is the momentum of the line where $\mathcal{I}(\mathcal{M})$ resides, and $s_d = 1(-1)$ when the worm is at the origin(destination) of the propagator line. The move is self complementary such that the acceptance ratio is,

$$\mathcal{A}_{R_R} = -\frac{G^0_{\text{new}}(\boldsymbol{k}')G^1_{\text{new}}(\boldsymbol{k})}{G^0_{\text{old}}(\boldsymbol{k})G^1_{\text{old}}(\boldsymbol{k}')} \tag{3.20}$$

A minus sign always accompanies this update, since the *reconnect* update alters the number of fermion loops by exactly one, which according to the Feynman rules requires a factor of -1.

Add/Remove Vertex

The *Add/Remove Vertex* update changes the order of the diagram by adding or removing a vertex at a random position in the diagram. In the case of $\boldsymbol{k}, \tau$ sampling, this update corresponds to adding/removing a vertex at time τ, an example is shown in Fig. 3.12.

The removal of a vertex is always rejected when the diagram is in an un-physical sector. If the diagram is in the physical sector, the *Remove* update (only applicable to diagrams of order $N \geq 2$, as there is no need to sample the non-interacting propagator) randomly chooses one of the interaction vertices to remove, via a uniform

distribution. This leaves four unconnected slots which must be reconnected according to the internal connectivity of the removed vertex. The removal of a vertex causes a violation of momentum conservation, which is remedied by appointing a pair of worm ends $\mathcal{I}$ and $\mathcal{M}$ – carrying the excess momentum of the removed interaction vertex – to the relevant slots. There is a binary choice to place either $\mathcal{I}$ or $\mathcal{M}$ on the upper or lower line, and for each worm end a further binary choice of which end of a propagator to place them. However, we pick the convention that $\mathcal{I}$ is always placed on the upper line and $\mathcal{M}$ on the lower line, such that the momentum carried by the worm is identical to that of the removed vertex. This seemingly innocuous convention requires an additional factor $\mathcal{P}_{RV} = 2$, since the Markov chain produces configurations with $\mathcal{I}$ on both the upper and lower lines, yet the *Remove* update cannot. Therefore, we can only produce half the diagrams in the configuration space for a given order. This convention leaves just two binary choices for the position of $\mathcal{I}$ and $\mathcal{M}$ to be placed, and hence a proposal probability of $\mathcal{P}_{RV} = 1/4N$.

In a representation that conserves momentum, e.g. $(\boldsymbol{k}, \tau)$, the addition of a vertex is trivially rejected if the diagram is in the physical sector i.e. we require worms to be present to perform this update. Conversely if the representation does not conserve momentum the add vertex update may always be called, e.g. sampling in real space. The *Add Vertex* update places an interaction vertex in the section of the diagram where the worms reside. The momentum through the new interaction vertex is the worm momentum $\boldsymbol{q} = \boldsymbol{\delta}$. The two propagators adjacent to the worm ends are removed, and replaced by four propagators. The worm is removed, and the new interaction vertex added at a time drawn from some distribution P_τ, adding a factor of $P_\tau d\tau$ to the proposal probability. The four propagators are then connected to the new vertex according to the requirements of the theory.

To be completely generic we must account for theories that do not conserve quantum

numbers when a new vertex is introduced. The quantum numbers at each slot of the new vertex will be drawn from a distribution $P_{\lambda_0,\ldots,\lambda_3}$ – where λ is an arbitrary quantum number – determined by the quantum numbers at the ends of the propagators prior to the update.

The acceptance ratio is determined by the values of the diagram configurations, local to the update, prior to, and post the proposed update. The *Add Vertex* update removes two propagator lines and adds an interaction vertex, and four new propagators whose values are determined by momentum conservation, resulting in a change of diagram weight: $G_0^{\text{old}} G_1^{\text{old}} \to V(\boldsymbol{q}) \prod_{i=0}^{3} G_i^{\text{new}}$. Following the diagrammatic rules for the transition from a diagram with N interaction vertices to $N+1$ there is a factor of $-d^d\boldsymbol{p}d\tau/(2\pi)^d$. The update also removes the worms contributing a factor of $1/c_w(N)d^d\boldsymbol{\delta}$ to the weight ratio, hence the acceptance ratio is

$$\mathcal{A}_{R_{AV}} = \frac{-P_\lambda}{4NP_\tau d\tau} \frac{V(\boldsymbol{q}) \prod_{i=0}^{n_v} G_i^{\text{new}}}{G_0^{\text{old}} G_1^{\text{old}}} \frac{d^d\boldsymbol{q}d\tau}{(2\pi)^d} \frac{1}{C_w d^d\boldsymbol{\delta}}, \tag{3.21}$$

where C_w is as defined in section 3.1.3.

In the case of the Hubbard model we choose the uniform distribution $P_\tau = U([0,\beta])$. There are no quantum numbers to draw, since interactions only occur between anti-parallel spins, with no spin flip processes, therefore P_λ reduces to 1, and the interaction is momentum independent such that $V(\boldsymbol{q}) = U$.

Optimized distribution for drawing vertex imaginary-time

The use of a uniform distribution to obtain the imaginary time associated with the added vertex in the *Add/Remove Vertex* update leads to low acceptance ratios when

sampling at low temperatures. This occurs when using a uniform distribution because the time-ordered non-interacting Green's function has exponential dependence on imaginary time:

$$G_0(k,\tau) = \Big[-\theta(\tau)(1 - f(\epsilon_{\boldsymbol{k}}) + \theta(-\tau)f(\epsilon_{\boldsymbol{k}})\Big] e^{-\epsilon_{\boldsymbol{k}\sigma}\tau/\hbar}, \tag{3.22}$$

where $\theta(\tau)$ is the Heavy-side step function, and $f(\epsilon_{\boldsymbol{k}})$ is the Fermi-Dirac function. For certain times we can expect to be at the tail of a Green's function, which will contribute only a small amount to the acceptance ratio, resulting in many rejections. To alleviate this problem we follow the work of Gukelberger [47] and draw τ from an exponential distribution. This is complicated by the fact that four propagators depend on the time of a single interaction vertex. To choose a new time we consider segments of time in interval $\tau \in [0, \beta)$. We draw the segment from a distribution with weights

$$w_s = \frac{1}{\mathcal{N}} \int_{\tau_s}^{\tau_{s+1}} d\tau G_0(\boldsymbol{k}_0, \tau - \tau_0) \ldots G_0(\boldsymbol{k}_3, \tau_3 - \tau), \tag{3.23}$$

where $\mathcal{N} = \sum_s w_s$ is the normalisation factor. A time inside the interval $\tau \in [\tau_s, \tau_{s+1}]$ is drawn from an exponential distribution, increasing the probability of an add vertex move. We extend this optimisation to the *Shift Position* update to further improve overall acceptance rates.

By repeated application of the above updates to an initial configuration via a Markov chain, we traverse the configuration space which allows us to record the self-energy of the one-particle irreducible Feynman diagrams to arbitrary precision. The range of momentum values we may acquire is dependent on the distribution from which we draw the momentum of the worm, $\boldsymbol{\delta}$. The measurements obtained depend

on the observable class implemented, which will be discussed in chapter 4.

3.2 Connected Determinant Diagrammatic Monte Carlo

Connected determinant diagrammatic Monte Carlo is an extension of determinant diagrammatic Monte Carlo (DDMC). DDMC calculates the thermal average of an operator O, as a ratio of determinants formed via expansion of the partition function in the interaction U, when written in terms of the action $S = S_0 + S_I$. The thermal average of an operator O is

$$\langle O \rangle = \frac{\mathrm{Tr}[e^{-\beta H} O]}{Z}. \tag{3.24}$$

Z in terms of the action is,

$$Z = \mathrm{Tr}[e^{-\beta H}] = \int \mathcal{D}[c^\dagger, c] e^{-S[c^\dagger, c]}, \tag{3.25}$$

where $\mathcal{D}[c^\dagger, c]$ denotes functional integration. The action for the Hubbard model reads

$$S_0 = \sum_{\boldsymbol{xy}} \int_0^\beta \int_0^\beta c^\dagger_{\boldsymbol{x}}(\tau)[G^{-1}_{0,\boldsymbol{xy}}(\tau - \tau')] c_{\boldsymbol{y}}(\tau') d\tau d\tau' \tag{3.26}$$

$$S_I = U \sum_{\boldsymbol{x}} \int_0^\beta n_{\boldsymbol{x}\uparrow}(\tau) n_{\boldsymbol{x}\downarrow}(\tau) d\tau, \tag{3.27}$$

where S_0 is the free (bilinear) part of the action, and S_I the interacting part. $G_{0,\boldsymbol{xy}}$ is the non-interacting Green's function connecting lattice site $\boldsymbol{x}_i$, and $\boldsymbol{x}_j$, and $n_{\boldsymbol{x},\sigma} =$

$c^\dagger_{\boldsymbol{x},\sigma}c_{\boldsymbol{x},\sigma}$ is the number operator for electrons with spin σ. Expanding the action in U (as previously done in section 2.1) , we may write the partition function as

$$Z = Z_0 \sum_{n=0}^{\infty} \frac{(-U)^n}{n!} \sum_{\boldsymbol{x}_1 \ldots \boldsymbol{x}_n} \int_0^\beta d\tau_1 \ldots d\tau_n \langle n_{\boldsymbol{x}_1\uparrow}(\tau_1) n_{\boldsymbol{x}_1\downarrow}(\tau_1) \ldots n_{\boldsymbol{x}_n\uparrow}(\tau_1) n_{\boldsymbol{x}_n\downarrow}(\tau_n)\rangle_0, \tag{3.28}$$

where $Z_0 = \int \mathcal{D}[c^\dagger, c] e^{S_0[c^\dagger,c]}$, and the average is over the non-interacting part of the action. Equation (3.28) generates $(n!)^2$ closed diagrams, which can be represented by non-interacting Green's functions connecting a configuration of vertices $V = \{(\boldsymbol{x}_1, \tau_1) \ldots (\boldsymbol{x}_n, \tau_n)\}$. By application of Wick's theorem the partition function may be written as a product of determinants,

$$Z = Z_0 \sum_{n=0}^{\infty} \frac{(-U)^n}{n!} \sum_{V_n} \det D_\uparrow(V_n) \det D_\downarrow(V_n), \tag{3.29}$$

with

$$\sum_{V_n} = \sum_{\boldsymbol{x}_1 \ldots \boldsymbol{x}_n} \int_0^\beta d\tau_1 \ldots d\tau_n,$$

where $D_\sigma(V_n) = \{G_{0,}(\boldsymbol{x}_i - \boldsymbol{x}_j, \tau - \tau')\}$ is an $n \times n$ matrix of non-interacting Green's functions. Taking O to be the single particle Green's function for an unpolarised system, one of the determinants obtains an extra row and column corresponding to the extra creation and annihilation operators, becoming $\tilde{D}_\sigma(\tilde{V}_n)$, an $(n+1) \times (n+1)$ matrix, with $\tilde{V}_n = (V_n; \boldsymbol{x}, \tau)$ [40, 48, 49]. The expectation value of O, is then,

$$\langle O \rangle = \frac{\sum_{n=0}^{\infty} \frac{(-U)^n}{n!} \sum_{V_n} \det \tilde{D}_\uparrow(\tilde{V}_n) \det D_\downarrow(V_n)}{\sum_{n=0}^{\infty} \frac{(-U)^n}{n!} \sum_{V_n} \det D_\uparrow(V_n) \det D_\downarrow(V_n)}. \tag{3.30}$$

The numerator, then, corresponds to both connected and disconnected diagrams with two open ends (all two-point diagrams), and the denominator all closed diagrams –

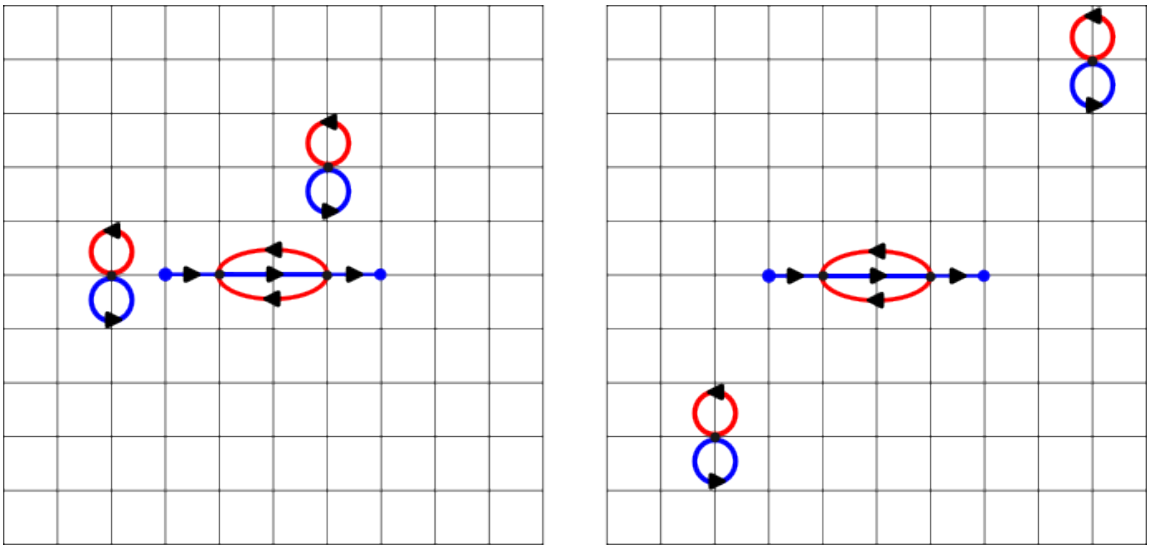


Figure 3.13: Representation of a single $n = 4$ configuration. Line colours denote spin, black circles are vertices, and the blue circles denote the external points introduced by the extra creation and annihilation operators. Both the configurations contribute weight w to the partition function.

as described in chapter 2. That is, for a given order n, the determinants correspond to all possible diagram topologies connecting n interaction vertices in configuration V. Both the numerator and denominator are sampled in DDMC, and the ratio taken at the end. The configuration of vertices V is obtained via Monte-Carlo, and the weight of a configuration is given as its contribution to the partition function. It is this property that restricts this method from being used in the thermodynamic limit. To understand this, consider the fourth order configuration of vertices in Fig. 3.13, where two diagrams are disconnected. On the left hand side the diagrams are close to the centre of the lattice. These diagrams contribute some weight w to the partition function. However, the configuration with the same set of diagrams, where the disconnected pieces are separated by a large number of lattice sites, shown on the right hand side, contributes the same weight w. The consequence of this being that the disconnected diagrams must be integrated across the whole lattice, which is

not achievable in the thermodynamic limit. Thus limiting the technique to relatively small lattice sizes.

The disconnected diagrams give redundant information, and from the previous discussion of the Linked Cluster theorem, we know that the disconnected diagrams may be factored out. The issue is, how to remove them from the calculation of the determinant. Rossi realised that a recursive procedure [41, 50] could be introduced to subtract the disconnected diagrams, so that simulations in the thermodynamic limit are possible. The subtraction method is nicely explained via set theory nomenclature. Let $C_E(V)$ be the sum of all connected diagrams with n vertices situated at space-time positions $V = \{(\boldsymbol{x}_1, \tau_1) \dots (\boldsymbol{x}_n, \tau_n)\}$ connected to some external points E – where the external points come from the addition of the creation and annihilation operators introduced by the operator O. Let $D_E(V)$be the sum of all connected and disconnected diagrams, and $D_\emptyset(V)$ the set of diagrams not connected to any external points i.e. the grand partition diagrams. Then, we may note that any disconnected diagram is made up of a connected part, which we may write as a proper subset $S \subsetneq V$, along with another part consisting of connected and/or disconnected diagrams, in the remaining $V \setminus S$. The product $D_\emptyset(V \setminus S)C(S)$, therefore contains all disconnected diagrams for a subset of vertices S. By subtracting the sum of the product over all subsets, we arrive at the formula for the connected only diagrams, for a configuration of vertices V,

$$C_E(V) = D_E(V) - \sum_{S \subsetneq V} D_\emptyset(V \setminus S) C_E(S). \tag{3.31}$$

Here $C(S)$ is found by first calculating $D(S)$ for all subsets S, then applying the formula recursively.

For a four point correlation function such as the spin structure factor, the determinant

must be extended by two rows and columns such that $\tilde{D}_\sigma(\tilde{V}_n)$ is an $(n+2)\times(n+2)$ matrix [49]. This leads to a slightly different recursive formula, as now the expectation value corresponds to all four point diagrams [51], and we must not sample any two point diagrams. For V internal vertices, and four external vertices labelled i, i', o, o', the recursion relation becomes [21],

$$C_{ii',oo'}(V) = D_{ii',oo'}(V) - \sum_{S\subsetneq V} D_\emptyset(V\setminus S)C_{ii',oo'}(S) - \sum_{S\subset V} C_{i,o}(S)C_{i',o'}(V\setminus S), \quad (3.32)$$

where $C_{i,o}(V)$ is all connected diagrams that have only two external vertices.
The complexity in evaluating $C(V)$ scales like 3^n [41, 48], – The calculation of $D(S)$ for all subsets S scales as $2^n n^3$, where n^3 is the cost to compute a determinant, with 2^n to calculate, but the leading scaling comes from the calculation of $C(S)$ as 3^n – such that the cDet algorithm provides a way to compute all diagrammatic contributions at order n in polynomial time. This allows cDet to reach orders much higher than classical diagMC in which complexity scales factorially with diagrammatic order.

In practice the matrix of non-interacting Green's functions $G_{0,}(\boldsymbol{x}_i - \boldsymbol{x}_j, \tau - \tau')$ is calculated on a grid of size $N_G \times N_G$, providing Green's functions spanning all combinations of lattice sites i, j. An initial configuration of vertices $\tilde{V}_{0,n}$ is drawn, and the matrices $\tilde{D}_\sigma(\tilde{V}_{0,n})$ are constructed. The recursive procedure is then carried out to remove disconnected diagrams, leaving only diagrams contributing to the observable. A Markov chain Monte Carlo scheme, implementing Metropolis-Hastings updates, provides a random walk through the space of configurations V_n, resulting in the calculation of the series coefficient of O, which are estimated from the average sign, $a_n = \sum_{V\in \mathrm{MC}} \mathrm{sign}(C(V))$, where MC stands for Markov chain. This process is then repeated – except for the generation of the Green's functions – for orders n,

until convergence is reached, to obtain a series expansion for the observable O.

The cDet updates are much simpler when compared with DiagMC; however, each Monte Carlo step is costly, as the disconnected diagrams must be removed. For ergodic sampling at constant order, two updates are required:

- Update New Space - A random vertex is selected from n vertices, and its position on the lattice is changed, where the new location differs from the old location by ± 1.
- Update New Time - A random vertex is selected from n vertices, and its imaginary time value is changed by drawing $\tau \in [0, \beta]$ from a uniform distribution.

However, since only the connected diagrams are calculated, and not the full ratio in Eq. (3.30), a normalisation method is required, and two more moves are implemented:

- Update Physical to Norm - Move from the physical to the normalisation sector. The normalisation diagram is the current diagram weight multiplied by the probability of the vertices being on sites $\boldsymbol{x}_i \dots \boldsymbol{x}_n$, when drawn from a Gaussian distribution centred on the central lattice site.
- Update Norm To Physical - Move from the normalisation sector to the physical sector.

Chapter 4

Diagrammatic Monte Carlo Implementation

As stated in the Introduction, much effort has been put into creating a DiagMC implementation that is:

1. Not restricted to a single theory.
2. Can sample two- and four-point diagrams.
3. Can handle both normal and anomalous propagators
4. Is easily extended to various lattice geometries, or even continuous space.

For such an implementation, it is crucial to create well-defined interfaces that incorporate the requirements of different theories. This is achieved via a C++ implementation, leveraging pointers to provide flexibility. For instance, a *GenericDiagram*

class serves as a base for all diagram types. By defining interfaces with pointers to the generic diagram objects, the top-level classes require no konwledge of theory specific details to operate.
In this chapter, we present modifications to the standard set of Monte Carlo updates introduced in the previous chapter, we discuss some of the specific implementation of our code, and the use of buffered measurements when recording observables.

4.1 Alterations to standard Updates

Well-defined interfaces may be crucial for a flexible code base, however to remain generic all MCMC updates must be modifiable. Modifications can be made by overriding functions[1] in different ways. For instance all proposal ratios and weights are easily alterable as each parameter – except for literals – is obtained from a function that can be overridden. As an example consider the uniform proposal distribution used in the *Create Worm* update, P_{δ}. The function that draws momentum from this distribution can be overridden to draw from any distribution. Moreover, the function that performs the update itself is also built on an abstract interface and can easily be modified if necessary. In short, all updates are based on an abstract interface that defines parameters covering most theories, though some edge cases may not be accounted for.

[1] The concept of overriding functions allows derived classes to redefine functions that a base class implements. A simple example of a derived class would be the class *Circle*, associated with the base class *Shape*.

4.1.1 Swap Measurement Alteration

One way to reduce the variance of observables is to include the basis function – we project measurements onto basis functions to avoid 'binning', this is detailed in section 4.9.1 – in the calculation of the diagram weight. With the inclusion of the basis function the diagram weight is

$$W = \prod_{i=1}^{N} V(\boldsymbol{q}_i) \prod_{j=1}^{2N-1} G_{0,j}(\boldsymbol{k}_j, \tau) B_l(\boldsymbol{k}_Y, \tau_Y). \tag{4.1}$$

Here N is the number of interaction vertices, and B_l represents one of the products of spatial and temporal basis functions given by $\{u_m(\boldsymbol{k}_Y) \otimes g_n(\tau_Y)\}$, with a linear index l. This functionality extends the definition of the measurement line to include the currently selected basis function weight, and the linear index of the currently selected basis function. We therefore must extend the set of updates to enable switching of the basis function index. This naturally fits in as an extension of the *Swap Measurement Line* update, which we call the *Swap Measurement Basis* update. The update proposes a new basis function by drawing a random number in the range $[0, L)$ – with L the total number of basis functions – from a uniform distribution. This is a self complementary update such that $\mathcal{P} = 1$. The acceptance ratio for the swap of a basis function is simply

$$\mathcal{A}_{R_{SMB}} = \frac{B_{l'}(\boldsymbol{k}, \tau)}{B_l(\boldsymbol{k}, \tau)}, \tag{4.2}$$

where l' is the newly drawn linear index, and l the previous linear index. Each measurement is then only projected onto the basis function included in the diagram weight, whereas we sample contributions to the overlap with each basis function, at

each measurement step, if this option is turned off. This is an optional update, and when turned on is called alongside the *Swap Measurement Line* update at a user defined rate. This option reduces the variance on individual basis functions at the cost of requiring more MC steps to project onto all basis functions sufficiently. For lattices with high symmetry, the number of basis functions required is generally low, however this is not the case for reduced symmetry systems.

4.1.2 Add/Remove Vertex Alterations

In the previous chapter, we noted that we take the convention that when a vertex is removed, we always place $\mathcal{I}$ on the upper line. We impose some further conventions on the *Add/Remove Vertex* update that make cases where the measurement line or anomalous propagators are involved simpler. If one of the propagators connected to a vertex that is to be removed is the measurement line, we take the convention that the update preserves the momentum of the measurement line. This convention leads to a unique choice for the location of one end of the worm, and a binary choice for the other end. This reduces the proposal probability to $\mathcal{P}_{RV,M} = 1/2N$ - Where the subscript M denotes the inclusion of the measurement line in the update.
For the case of a vertex with a single incoming and outgoing anomalous line, we take the convention to leave the momentum of these lines untouched, and therefore have a unique choice for the locations of $\mathcal{I}$ and $\mathcal{M}$. The worm ends then must connect to the slots on the remaining vertices that contained the normal lines. The proposal probability is therefore $\mathcal{P}_{RV,A} = 1/N$.

4.2 Update Validity Checks

The updates involved in DiagMC are fairly complex for a single theory, when generalising this, it becomes even more complicated. We therefore implement debug checks that may be turned on/off by building the program with a specific debug flag. When an update is performed in debug mode the update, its reverse, and the reverse of the reverse update are performed. For example, consider the *Add Vertex* update, this update is performed and the location of the removed worms stored. The *Remove Vertex* update (reverse update) is then immediately performed, and places the worm ends at the predefined locations stored from the *Add Vertex* update, producing the initial diagram prior to the *Add Vertex* update – if the move is implemented correctly. The *Add Vertex* update (reverse of the reverse update) is then performed on the configuration that the *Remove Vertex* update produced, giving the final result of the update debug cycle. At each step of the cycle the diagram details are recorded, e.g. diagram sign, weight etc., and compared with the corresponding configuration in the cycle. Such an implementation both ensures that the currently implemented updates are correct, and that future theory specific overrides can be easily debugged. In addition to the debug tests, we implement a range of unit tests on the many custom data structures defined in the code, which we run using the Google Test framework.

4.3 Diagram Validity Checks

When performing updates we require the new configuration to be a properly formed irreducible Feynman diagram, i.e. have the correct connections. Therefore, when performing certain updates, we perform a validity check on the diagram prior to

accepting the new configuration. This also turns out to be a useful method when debugging updates. The main checks performed are that of irreducibility, and the detection of tadpole diagrams. However when performing simulations with dressed propagators we must also check for self energy insertions.

To check for bare tadpoles it is sufficient to check that the destination of any single propagator is not the same vertex as its origin, which is a set of $(2N-1)$ operations, since we only need to check each line once. Alternatively, we may check for a vertex that transfers zero momentum.

Checking for one-particle irreducibility is more costly since we must compare the momentum of $(2N-1)$ propagators with that of the measurement line, i.e. the diagrams external momentum. This check is performed in both the physical and worm sector, therefore we must also take the worm momentum into account.

Self energy insertions are detected by checking for two propagators having equal momentum. Although this can occur without a self energy insertion being present, the set of diagrams that have this property is vanishingly small, and therefore our results are unaffected by rejecting all such diagrams.

We do not sample tadpoles since they provide a large, but trivial contribution to the self energy due to their momentum independence. Furthermore they massively increase the configuration space as each diagram of order $N \geq 2$ may contain propagators dressed with a tadpole insertion. We therefore disallow all tadpole diagrams, which corresponds to a shift in chemical potential. For the Hubbard model, the tadpole evaluates to Un_σ (the Hartree term) where n_σ is the density of a given spin, we therefore sample at chemical potential,

$$\mu' = \mu - Un_\sigma, \tag{4.3}$$

with μ the non-interacting chemical potential, such that for the half filled square lattice Hubbard model at $U = 1$, $\mu' = 0$.

4.4 Scaled Integers

When checking diagrams for 1-particle-irreducibility, or self-energy insertions, we must check the equality of many propagators. The obvious variable type to store momentum is a float. However, due to the binary storage of numbers it is not possible to reliable compare floating point numbers, e.g. for $a = 0.3$ and $b = 0.2 + 0.1$, $a == b$ returns false, due to floating point representation. One way to approach these comparisons is to define some threshold value, such that if the absolute difference between two floats is lower than the threshold we consider them identical. This requires knowledge of the magnitude of the numbers a-priori, and as such is not a global solution. We may use machine precision *eps* for the threshold, however the value can alter depending on the underlying architecture of the machine, mainly 32- vs 64-bit differences. We therefore implement what we call *Scaled Integers*. We represent float values in the range $(-MaxValue, MaxValue]$ with the granularity of a long integer. This results in a periodic number over this interval under addition, via integer overflow. We define a scale factor as `MaxValue/INT64_MIN`, where `INT64_MIN` $= (-2^{63} + 1)$. The real value is then stored as a long given by `Value=Val/ScaleFactor`. In this way we can compare values with the scaled integer equality operator, without having to worry about undetermined behaviours due to varying machine precision on different systems. This also doubles as a way to produce periodic values, which is useful for both momentum – when working on a lattice – and imaginary time. Moreover, Scaled Integers remove the need to manually check

bounds on such values when performing calculations, e.g. ensuring anti-periodicity of $G(\boldsymbol{k}, \tau)$.

4.5 Code Structure & Implementations

As stated in the abstract, the goal of the project is to create a code base – that will eventually be released – that can perform DiagMC simulations for different theories with minimal work by the user. To this end much time has been spent working on interfaces that are generic enough to encompass all but edge case scenarios. As such the code is structured in a rather complex way. Fig. 4.1 shows a basic overview of the most important high level classes. Note that all these classes are derived from abstract classes that enforce their interface in a purely virtual manner[2], these have been left out of the diagram for brevity. The code base is implemented in C++, which is chosen since this is one of the most sophisticated object-oriented programming languages. The availability of templates, and abstract classes allows us to make things as generic as possible. This is achieved by "templating" all classes with parameters that are theory dependent, and instantiating all theory dependent variables as pointers to their abstract class. Interfaces for functions are then based on the abstract class pointers, allowing us to freely pass specific implementations across classes.

Below we briefly discuss the implementation of the base classes, and some functionality.

[2]A pure virtual function enforces an interface but does not provide a definition.

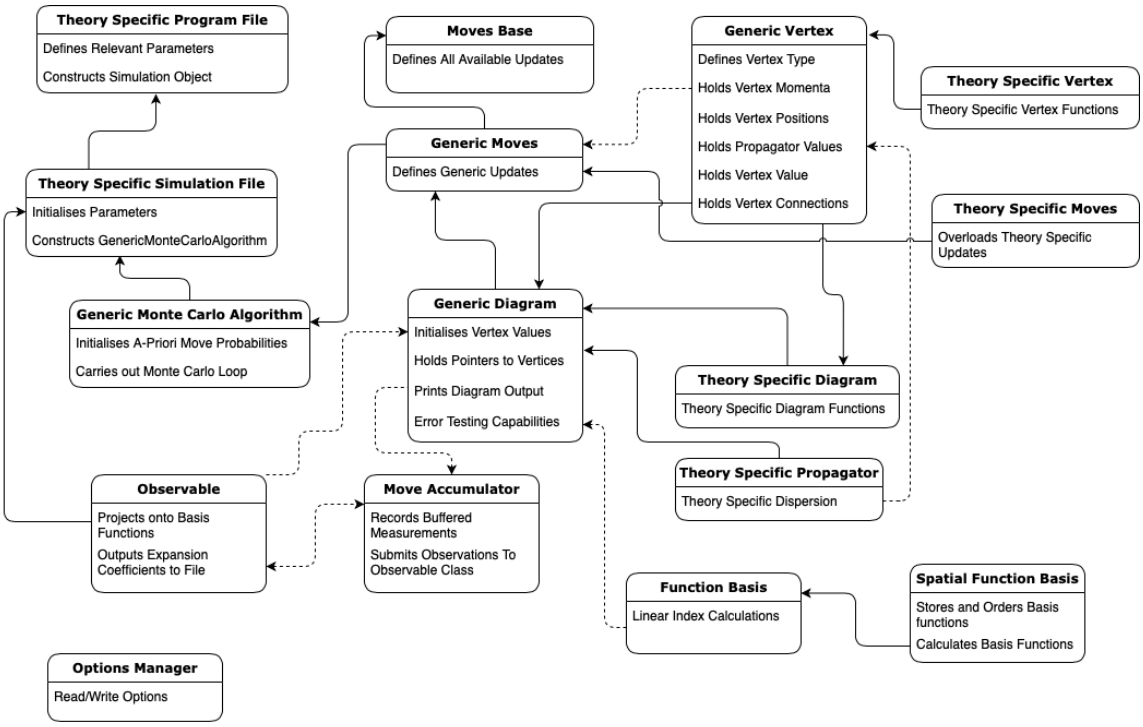


Figure 4.1: UML type diagram of top-level classes. All classes have a dependency on the Option Manager class, which has been disconnected for clarity. Solid lines indicates an association. Whilst dotted lines indicate a dependency. Lines point in the direction of the association/dependency

4.5.1 Updates/Moves

The *GenericMoves* class implements the updates described in chapter section 3.1.3. The updates defined in this class are generic, since they obtain all relevant information from the theory-specified *Diagram* and *Vertex* classes. The calculation of the acceptance ratios depends on the internal connection of the vertex, and therefore is handed off to the *DiagramWeightEvaluator* class to avoid hard-coding a specific case. *GenericMoves* is derived from *GenericMovesBase* which lists all available updates, and defines accessor function interfaces.

4.5.2 Vertices

The *GenericVertex* class defines the data structure of both vertices and propagators, describing connectivity of vertices, and propagator values. This class defines the number of slots on the vertex, and holds a unique label identifying the vertex. All relevant information required by the *Diagram* and *Update* classes is obtained from the accessor routines defined in *GenericVertex*. Each vertex holds data on its internal connections, connections of the propagators associated with its slots, and the associated propagators value, momentum, and quantum numbers.

4.5.3 Diagrams

The *Diagram* class brings the *Vertex*, *Propagator*, *Accumulator* and *Observable* classes together. It defines all functions for calculating vertex and propagator values. The *Diagram* class defines the construction of the initial diagram with which the simulation begins, or allows for cloning of a diagram that is saved in a hdf5 file – this option allows us to store diagrams at arbitrary orders, and then begin simulations from those orders. The *Diagram* class holds an array of pointers to vertex objects, and therefore has access to all the information about the diagram. The array of vertex pointers is used to access information about "active" vertices. Since the diagram order can alter during a simulation, we must have at least N vertex objects defined. We define an active vertex as one that is currently in the diagram, whereas a non-active vertex is one that is currently not part of the diagram, e.g. a vertex removed via the remove vertex update. In this way we can avoid costly construction and deletion of vertex objects by simply updating an array of pointers, and only accessing relevant vertices

at any given time. Furthermore, all observations are recorded via a function defined in the *Diagram* class, as well as application of normalisation to the data – if the norm diagram method is used. The *Diagram* class is derived from *DiagramData* which defines the measurement line(vertex) properties, worm functionality, and sector flags. The *DiagramData* class is responsible for holding the data that the *Diagram* class uses, it is therefore a useful class to 'dump', when running into debugging issues [52].

4.5.4 Observables

Observables are created via an intermediate class, the *ObservableManager*. The idea is to implement an observable manager for individual theories, which holds information on all available observable classes that are applicable to the theory at hand. The observable manager does not contain an abstract interface layer, since it is difficult to consider observable needs for all theories in a generic sense.

Observables are currently all derived from the *AbstractGenericSelfEnergyObservable* class which defines an interface for asking if the observable is based on basis function expansion or binning, accessor functions for obtaining the number of available basis functions and to set the current basis function index, an interface for recording and finalizing measurements, and interfaces for exporting data in different formats such as GNUplot, or HDF5 file types.

Furthermore, observables instantiate *Grid* classes, which deal with storing the recorded data. We define multiple of such classes. For a simple test case we define a *Histogram* grid class which records data in a histogram fashion. This is the simplest grid base class which does not perform any error calculations other than the naive mean calculation. The *GridBasedObservable* class is more sophisticated, and comes in two

flavours. One that implements tensor bins – used to record multiple observations enumerated with a given set of indices – and one that does not. Tensor binning is used when combining both spatial and temporal basis functions, as the product of each must be considered. Both grid classes calculate the jack-knife average by implementing "time" bins which can hold x amount of observations, these then get folded back onto each other via a jack-knife analysis, as described in section 4.12.

4.5.5 Move Accumulator

The *MoveAccumulator* class is the interface between the *GenericDiagram* and *Observable* classes. It is passed a pointer to the diagram class, and the measurement line(vertex) to obtain the current weight of the diagram, along with the re-weighting factor. The move accumulator stores the number of positive and negative diagrams recorded since the measurement line(vertex) has been altered. Upon altering the measurement line the move accumulator invokes the *Observe* function on the given observable. The move accumulator is therefore the practical implementation of the "buffered measurements" – see section 4.10.

4.5.6 Sectors

The sectors mentioned in section 3.1.3 are implemented as flags, which we define as a *Diagram State*. The diagram state holds a flag indicating the sector(s) we are currently in, which are implemented as an enumeration [52]:

```
enum StateFlags
{
SigmaSector = 0x1;
WormSector = 0x2;
HighOrderSector = 0x4;
NormSector = 0x8;
}
```

The single enumeration allows us to uniquely identify which sectors we are in with a single flag, e.g. if the flag is set to 5, the diagram is both physical (Σ sector) and of order $N > 1$ ($\mathcal{H}$ sector).

4.5.7 Monte Carlo Algorithm

The *GenericMonteCarloAlgorithm* class defines the execution of the Markov chain. This class also records information on proposal and acceptance rates for simulations, which is useful for tuning parameters for production runs. This class implementents the random choice for the next type of Monte Carlo move to be applied. Rather than randomly picking from all available moves, the sector of the diagram is queried, and only moves that are available in the current sectors are chosen from. This increases the acceptance ratio of moves, when compared to a naive method of obtaining the next move, since we are not trivially rejecting proposed moves which cannot occur in a given sector. Moreover, we define the a-priori proposal ratio of updates to be a user defined value, which is accounted for when drawing the next update. The function defining the available moves in each sector is a virtual function that can be overloaded for specific theories, if required.

4.6 Observable matrices

The *Diagram* class requires access to the observables to record measurements. We build an $n \times n$ matrix of pointers to the observables where n is both theory and observable specific. For the Hubbard model self-energy observables, we create the following matrix

$$\begin{bmatrix} \Sigma_{\uparrow} & \Sigma_{\uparrow\downarrow} \\ \Sigma_{\downarrow\uparrow} & \Sigma_{\downarrow} \end{bmatrix}.$$

Here the diagonals point to observables for up, and down spins of standard propagators, and the off diagonals to anomalous propagator observables. In the normal state we do not consider anomalous propagators and the off-diagonal pointers are empty. If the system is polarized the diagonal elements are two distinct observables, whereas an unpolarised system i.e. $\delta\mu = 0$, has $\Sigma_{\uparrow} \equiv \Sigma_{\downarrow}$ and all measurements are recorded in a single observable class. For the unpolarised case this implementation avoids the double counting of each observable, and we may also reduce the number of MC updates by turning off the *Swap Measurement Line* update.

4.7 Shift Position Sampling Biases at Second Order

The literature on diagMC very rarely discusses issues introduced by the Markov-chain sampling of diagrams. An issue that has arisen in our DiagMC code is the biasing of the τ dependence when drawing new vertex times in the interval $[0, \beta]$ via the *Shift Position* update in the $\boldsymbol{k}, \tau$ space representation.

This issue arises when sampling self-energy diagrams corresponding to the single particle Green's function. As discussed above, such self energy diagrams are "am-

putated", i.e. have their external non-interacting propagators removed. Instead of sampling these directly we close the diagram via a dummy line called the *measurement line*, which holds the diagram's external momentum and τ dependence. We denote $\Delta\tau = \tau_2 - \tau_1$ as the τ dependence of the measurement line, where τ_1 is the time corresponding to the vertex slot where the measurement line begins, and similarly τ_2 where the measurement line ends.

When shifting an internal vertex - defined as a vertex that does not connect to the measurement line - this update produces the desired result i.e. repeated application of this update is equivalent to integrating the internal τ over the interval $[0, \beta]$, which is required to compute the contribution from the diagram. When this update acts on a vertex which has the measurement line attached, we find that there is a bias in the a-priori probability as far as $\Delta\tau$ is concerned. The issue arises as we do not directly draw $\Delta\tau$, instead we draw either τ_1 or τ_2, and as a consequence of this we can only obtain $\Delta\tau = \pm\beta$ when one vertex with the measurement line attached, resides at $\tau_{1(2)} = 0$, and the other vertex with the measurement line attached at $\tau_{2(1)} = \beta$.

Consider the case in which we are shifting the vertex attached to the origin of the measurement line. This corresponds to drawing τ_1 in the interval $[0, \beta]$. Assuming that values of τ_1 are evenly distributed in the interval $[0, \beta]$ in the course of our calculation, and due to the overall invariance of diagram amplitudes under simultaneous translations of all vertices, a uniform choice of $\tau_2 \in [0, \beta]$ implies that *Shift Position* updates which yield $\Delta\tau$ occur with a probability

$$P(\Delta\tau) = \begin{cases} c(\beta - (\tau_2 - \tau_1)) & \Delta\tau > 0 \\ c(\beta + (\tau_2 - \tau_1)) & \Delta\tau < 0, \end{cases}$$

where c is the normalisation value. Writing the piecewise conditions explicitly in terms of the values we actually draw - τ_1, τ_2,

$$P(\tau_2 - \tau_1) = \begin{cases} c(\beta + (\tau_2 - \tau_1)) & 0 < \tau_2 < \tau_1 \\ c(\beta - (\tau_2 - \tau_1)) & \tau_1 < \tau_2 < \beta. \end{cases}$$

The probability distribution function (PDF) is shown in figure 4.2. This leads to

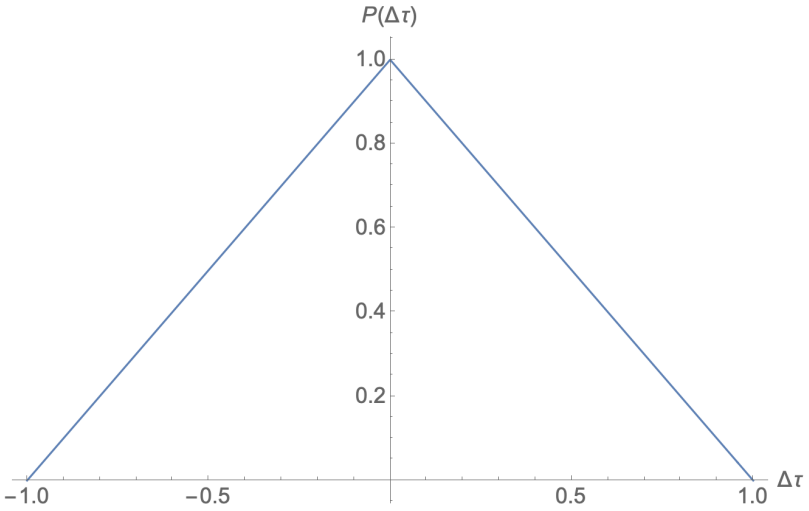


Figure 4.2: Probability distribution of drawing $\Delta\tau$ when τ_2, and τ_1 are both independently drawn from the interval $[0, \beta]$

bias sampling towards $|\Delta\tau|$ taking on smaller values. As a consequence of this we find that there is no amplitude for the self-energy observable near $\pm\beta$. Fig. 4.3 shows the sampled self-energy, $\Sigma(\tau)$, for a constant momentum in the BZ, where the range $[-\beta, 0)$ has been shifted in the range $(1, 2]$. We find that $\Sigma(\tau \to \pm\beta) \to 0$.

If the shift position move touches on the measurement propagator, then one way to overcome this issue is to update both vertices attached to it by drawing the value of $\Delta\tau$ directly in the range $[0, \beta]$. In this instance we would assign one of the two

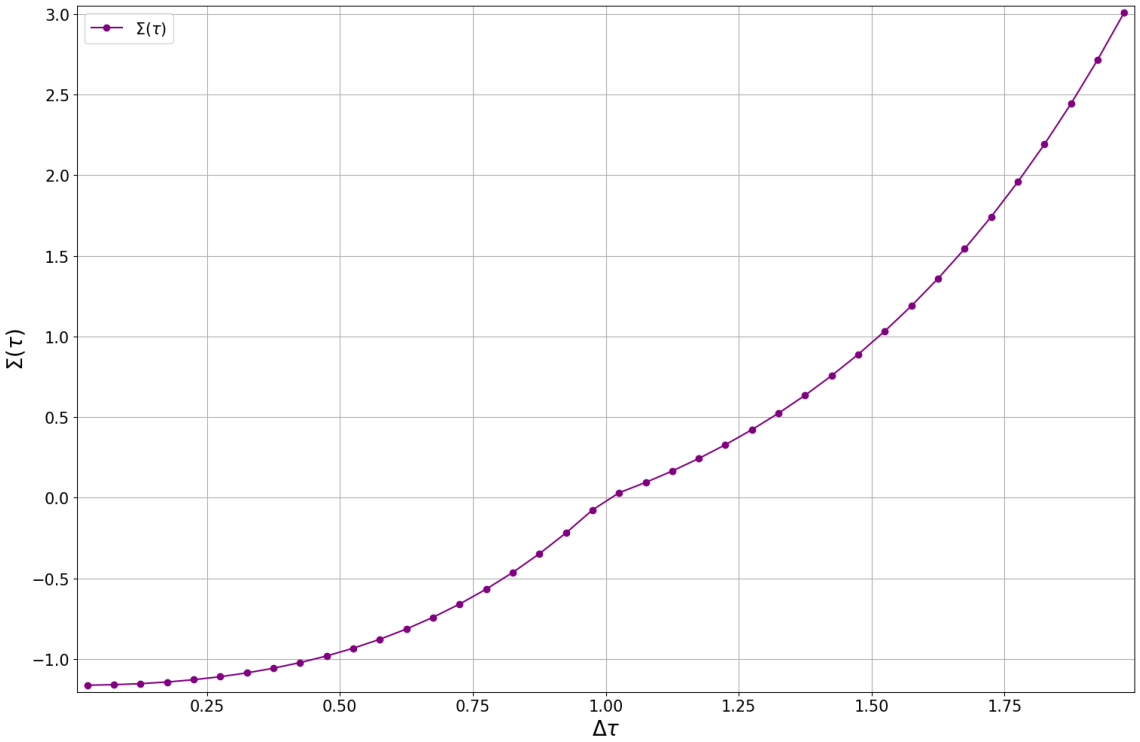


Figure 4.3: Second order momentum independent self-energy obtained via only the *Shift Position* update drawing a single τ value, showing the self-energy amplitude tending to zero as $\Delta\tau$ tends towards $\pm\beta$. On the $\Delta\tau$ axis the interval $[0, 1]$ represents $[0, \beta]$, and $(1, 2]$ represents $(-\beta, 0)$.

vertices to a value in the range $\tau = \beta - \Delta\tau$. The vertex connected to the other end of the measurement line is then assigned the value $\tau' = \tau + \Delta\tau$.

However we still need to shift internal vertices one at a time to sample the integration over τ. Therefore it was proposed that a combination of these updates would achieve the desired results - note that at second order we are required to draw $\Delta\tau$ 100% of the time as there are no internal vertices. The combinations of these moves does indeed reconcile this problem. However the combination of such moves is somewhat unsatisfactory, as it requires tweaking the probability of drawing one of the two moves depending on the diagram order.

A more satisfactory approach to remove the implicit bias from the proposal probability would be, on average, to push the vertices apart by drawing the new vertex position from the inverse of the above PDF. This requires drawing new times for vertices connected the measurement line from the probability distribution,

$$P(\tau_2) = \begin{cases} c_i/(\beta + \tau_2 - \tau_1) & 0 < \tau_2 < \tau_1 \\ c_i/(\beta - \tau_2 + \tau_1) & \tau_1 < \tau_2 < \beta, \end{cases}$$

To obtain random values for the new vertex time from this PDF, we require the CDF, and the *inversion method*.

Calculating the normalisation factor, c, using the fact that $\int_{-\infty}^{\infty} P(\tau_2) = 1$ we find,

$$P(\tau_2 < \tau_1) + P(\tau_2 > \tau_1) = c_i \int_0^{\tau_1} \frac{1}{(\beta + \tau_2 - \tau_1)} d\tau_2 + c_i \int_{\tau_1}^{\beta} \frac{1}{(\beta - \tau_2 + \tau_1)} d\tau_2 = 1, \tag{4.4}$$

leading to

$$c_i = \frac{1}{\ln\left(\frac{\beta}{\beta - \tau_1}\right) + \ln\left(\frac{\beta}{\tau_1}\right)}. \tag{4.5}$$

We find the CDF via $F(\tau_2) = \int_{-\infty}^{\tau_2} P(\tau_2)$. In the range $0 < \tau_2 < \tau_1$,

$$F(\tau_2) = \int_0^{\tau_2} \frac{1}{(\beta + \tau' - \tau_1)} d\tau' = \ln\left(1 + \frac{\tau_2}{\beta - \tau_1}\right), \tag{4.6}$$

for $\tau_1 < \tau_2 < \beta$,

$$F(\tau_2) = F(\tau_2 = \tau_1) + \int_{\tau_1}^{\tau_2} \frac{1}{(\beta - \tau' + \tau_1)} d\tau' = \ln\left(\frac{\beta}{\beta - \tau_1}\right) + \ln\left(\frac{\beta}{\beta - \tau_2 + \tau_1}\right). \tag{4.7}$$

And therefore the CDF is given by,

$$F(\tau_2) = \begin{cases} c_i \ln\left(1 + \frac{\tau_2}{\beta - \tau_1}\right) & 0 < \tau_2 < \tau_1 \\ c_i \Big[\ln\left(\frac{\beta}{\beta - \tau_1}\right) + \ln\left(\frac{\beta}{\beta - \tau_2 + \tau_1}\right) \Big] & \tau_1 < \tau_2 < \beta. \end{cases}$$

The inversion method states that we draw a uniform random number in the interval $r = [0, 1]$, and set this equal to $F(\tau_2)$ to obtain τ_2 given r. Carrying out this procedure for the CDF we obtain,

$$\tau_2 = \begin{cases} (\beta - \tau_1)(\exp(\frac{r}{c}) - 1) & 0 < r < c_i \ln\left(1 + \frac{\tau_1}{\beta - \tau_1}\right) \\ \beta + \tau_1 - \frac{\exp(\frac{-r}{c})\beta^2}{\beta - \tau_1} & c_i \ln\left(1 + \frac{\tau_1}{\beta - \tau_1}\right) < r < \beta. \end{cases}$$

One thing that must be considered when drawing from such a distribution is if there is a change in the proposal ratio, as detailed balance must be adhered to. This is easily checked by comparing the move to its inverse. given a τ_1 and τ_2, we draw a new position τ_2', as the new time for the vertex associated with the current time τ_2. The inverse of this is to draw τ_2 given τ_2'. This leads to a factor in the proposal ratio,

$$\mathcal{P} = \frac{\beta - (\tau_2' - \tau_1)}{\beta - (\tau_2 - \tau_1)}. \tag{4.8}$$

Which again, is only required when we are shifting a vertex that connects to the measurement line.

Mathematically, we can also extend the integration over internal variables to the interval $[-\beta, \beta]$, as all diagram amplitudes are conserved under translations of vertex times by β - a consequence of the anti-symmetry of fermion lines. This turns out to be the most elegant solution as no balancing of updates is required, making the sampling process more autonomous. This issue was not entirely trivial to find, and

eluded our bug finding approach for some time, such that we believe it to be worthy of documenting.

4.8 Observables

This section follows closely Section III in Van Houcke *et al* [30]. Our implementation of observables projects measurements onto symmetry-adapted basis functions according to the lattice geometry at hand. We have two different implementations to treat this: We either project onto all possible basis functions (see section 4.9), via a scalar product upon every recorded measurement, or alternatively we include the basis function amplitude in the MC weight function. By including the basis function in the MC weight, the acceptance ratio of updates is dependent on the currently selected basis function. This in turn reduces the overall variance of measurements, at the cost of the expansion of the configuration space – there is no free lunch.
To evaluate the diagrammatic expansion, we must, for all external variables Y, carry out the sum over all topologies $\mathcal{T}$, and integrate over all internal variables X. This boils down to calculating overlaps of the form

$$\mathcal{A}_{Q,g_l} = \int dY \mathcal{Q}(Y) g_l(Y), \tag{4.9}$$

where $\mathcal{A}_{Q,g_l}$ denotes the overlap of the observable $\mathcal{Q}$ onto the basis function g_l. Writing the observable in terms of Feynman diagrams we find,

$$\mathcal{A}_{Q,g_l} = \sum_k \sum_{\mathcal{T} \in S_\mathcal{Q}} \int dX dY \mathcal{D}(\mathcal{T}, X, Y) g_k(Y) \delta_{k,l} 1_{\mathcal{T} \in S_\mathcal{Q}}. \tag{4.10}$$

Extending the definition of a configuration to include a basis index k,

$$\mathcal{C} = (\mathcal{T}, X, Y, k), \tag{4.11}$$

such that,

$$\int d\mathcal{C} = \sum_k \sum_{\mathcal{T}} \int dX dY. \tag{4.12}$$

Here we have defined $S_{\mathcal{Q}}$ to be the set of all irreducible diagrams.

We may re-write this as a weighted average over configurations[3] obtaining,

$$\mathcal{A}_{Q,g_l} = \int d\mathcal{C} |\mathcal{D}(\mathcal{C}) g_k(Y)| \mathrm{sgn}[D(\mathcal{C}) g_k(Y)] \delta_{k,l} 1_{\mathcal{T} \in S_{\mathcal{Q}}}. \tag{4.13}$$

To evaluate this via a Monte Carlo algorithm we should re-write this as,

$$\mathcal{A}_{Q,g_l} = \int d\mathcal{C}\ w(\mathcal{C})\ A_{\mathcal{Q},g}(\mathcal{C}), \tag{4.14}$$

taking,

$$w(\mathcal{C}) = |\mathcal{D}(\mathcal{C}) g(Y)| R(\mathcal{C}), \tag{4.15}$$

where $R(\mathcal{C})$ is some arbitrary positive re-weighting function, we find that Eq. (4.13) and Eq. (4.14) agree if we set,

$$A_{\mathcal{Q},g_l}(\mathcal{C}) = \frac{\mathrm{sgn}[\mathcal{D}(\mathcal{C}) g_k(Y)] \delta_{k,l} 1_{\mathcal{T} \in S_{\mathcal{Q}}}}{R(\mathcal{C})}. \tag{4.16}$$

[3] note that only cases where both the diagram and the possible basis functions are real, has been implemented, complex cases are to be addressed in future updates

The average over n configurations will then approach the exact result in the large-n limit,

$$\mathcal{A}_{Q,gl} = \mathcal{Z} \lim_{n\to\infty} \frac{1}{n} \sum_{i}^{n} A_{\mathcal{Q},gl}(\mathcal{C}_i). \tag{4.17}$$

The basis functions used for the momentum/spatial dependence are those of the lattice point group symmetry, and we define them to be orthogonal such that,

$$B \int_{BZ} u_k^*(\mathbf{p})\ u_{k'}(\mathbf{p}) = \delta_{k,k'}, \tag{4.18}$$

with B the normalisation factor. By setting $g_k(Y) = \sqrt{B} u_k(\mathbf{p})$ we find the expansion coefficients $\mathcal{Q}_l = \sum_k \int dY\, \mathcal{Q}(Y) g_k(Y) \delta_{k,l}$. Which allows calculation of an observable $\mathcal{Q}$ via,

$$\mathcal{Q}(\mathbf{p}, \tau) = \sum_k \mathcal{Q}_k\ u_k^*(\mathbf{p}). \tag{4.19}$$

4.8.1 Observable Normalisation

If we are able to compute $\mathcal{Z}$ we can then obtain the normalised observable via our DiagMC simulations. However in general we do not know the overall weight, so we must find some relations to $\mathcal{Z}$ that will allow us to normalise our observables. We implement two different methods for normalising in our code.

Method 1: We extend our configuration space to include a normalisation sector, in which we create an artificial diagram whose value is known analytically, or by some simple numerical methods, given by

$$\mathcal{Z}_N = \int_{S_N} dC w(\mathcal{C}). \tag{4.20}$$

By recording how many times we enter this normalisation sector as $\mathcal{N} = \sum_{i=1}^{n} 1_{\mathcal{C}_i \in S_{\mathcal{N}}}$, we can replace the dependence of $\mathcal{Z}$ via the relation $\mathcal{Z}_N/\mathcal{Z} = \lim_{n\to\infty} \mathcal{N}/n$, leading to

$$\mathcal{A}_{Q,g_l} = \mathcal{Z}_{\mathcal{N}} \lim_{n\to\infty} \frac{1}{\mathcal{N}} \sum_{i}^{n} A_{\mathcal{Q},g_l}(\mathcal{C}_i) = \frac{\mathcal{Z}_{\mathcal{N}}}{\mathcal{N}} \tilde{\mathcal{A}}_{\mathcal{Q}}, \tag{4.21}$$

with $\tilde{\mathcal{A}}_{\mathcal{Q}} = \lim_{n\to\infty} \sum_{i}^{n} A_{\mathcal{Q},g_l}(\mathcal{C}_i)$. The normalisation diagram is arbitrary, but in practice we take this to be the Hartree diagram with constant propagator values for the Hubbard model. This option works perfectly well for low orders, however, for higher orders, it starts to become difficult to traverse from order N to the normalisation sector such that we increment the norm counter $\mathcal{N}$ sufficiently.

Method 2: We limit the simulation to diagrams that are at the target diagram order m, and $m-1$. We then obtain observables for a single order m, using the $m-1$ order to normalise the results. We choose the normalisation as the integral of the absolute value of the self energy, since this is a robust observable, as it does not suffer from a sign problem.

Let the normalised overlap of the absolute value of the self energy be denoted as $\mathcal{A}_{|\Sigma|} \equiv \int dY |\Sigma(Y)| = |\Sigma|$ for brevity, and let the non-normalised absolute value of the self energy be the sum over all configurations which have order equal to the target order m, which we denote,

$$|\tilde{\Sigma}|_m^{(l,l+1)} = \lim_{n\to\infty} \sum_{i}^{n} \frac{\delta_{O_{\mathcal{C}_i},m}}{R(\mathcal{C}_i)}. \tag{4.22}$$

Here n is the number of configurations sampled, $O_{\mathcal{C}_i}$ denotes the order of the configuration being measured, and l is either equal to m, or $m-1$, since we require the absolute value of the self energy from sampling of orders $m-1, m$ and $m, m+1$

separately, to carry out the normalisation. Following Eq. (4.21) we may write

$$|\Sigma|_m^{(l,l+1)} = \frac{\mathcal{Z}_{\mathcal{N}_l}}{\mathcal{N}_l^{(l,l+1)}} \, |\tilde{\Sigma}|_m^{(l,l+1)}. \tag{4.23}$$

We assume that $\mathcal{Z}_{\mathcal{N}_1}$ is known, and that since $|\Sigma|_m$ is an observable $|\Sigma|_k^{(m,m+1)} = |\Sigma|_m^{(m-1,m)}$. As an example, consider the calculation of the absolute value of the self energy at third order, normalised by the second order contribution:

$$|\Sigma|_3^{(2,3)} = \frac{\mathcal{Z}_{\mathcal{N}_2}}{\mathcal{N}_2^{(2,3)}} \, |\tilde{\Sigma}|_3^{(2,3)}, \tag{4.24}$$

$\mathcal{Z}_{\mathcal{N}_2}$ is unknown, so we must obtain it in terms of $\mathcal{Z}_{\mathcal{N}_1}$, we require both

$$|\Sigma|_2^{(1,2)} = \frac{\mathcal{Z}_{\mathcal{N}_1}}{\mathcal{N}_1^{(1,2)}} \, |\tilde{\Sigma}|_2^{(1,2)}, \tag{4.25}$$

and

$$|\Sigma|_2^{(2,3)} = \frac{\mathcal{Z}_{\mathcal{N}_2}}{\mathcal{N}_2^{(2,3)}} \, |\tilde{\Sigma}|_2^{(2,3)}. \tag{4.26}$$

Since $\mathcal{Z}_{\mathcal{N}_1}$ is known, and $|\Sigma|_2^{(1,2)} = |\Sigma|_2^{(2,3)}$ we obtain

$$\mathcal{Z}_{\mathcal{N}_2} = \frac{|\Sigma|_2^{(2,3)} \mathcal{N}_2^{(2,3)}}{|\tilde{\Sigma}|_2^{(2,3)}} = \frac{|\Sigma|_2^{(1,2)} \mathcal{N}_2^{(2,3)}}{|\tilde{\Sigma}|_2^{(2,3)}}, \tag{4.27}$$

and therefore,

$$|\Sigma|_3^{(2,3)} = \frac{|\Sigma|_2^{(1,2)}}{|\tilde{\Sigma}|_2^{(2,3)}} |\tilde{\Sigma}|_3^{(2,3)}. \tag{4.28}$$

However,

$$|\Sigma|_2^{(1,2)} = \frac{\mathcal{Z}_{\mathcal{N}_1}}{\mathcal{N}_1^{(1,2)}} \, |\tilde{\Sigma}|_2^{(1,2)}, \tag{4.29}$$

hence

$$|\Sigma|_3^{(2,3)} = \frac{\mathcal{Z}_{\mathcal{N}_1}|\tilde{\Sigma}|_2^{(1,2)}}{\mathcal{N}_1^{(1,2)}|\tilde{\Sigma}|_2^{(2,3)}}|\tilde{\Sigma}|_3^{(2,3)}, \tag{4.30}$$

which becomes a telescopic product at arbitrary order. Generically we may write the normalisation factor as

$$\mathcal{Z}_{\mathcal{N}_l} = \frac{\mathcal{N}_l^{(l,l+1)}|\Sigma|_l^{(l-1,l)}}{|\tilde{\Sigma}|_l^{(l,l+1)}}. \tag{4.31}$$

We may then use the normalised absolute value of the self-energy to normalise any observable, as follows,

$$\mathcal{A}_{\mathcal{Q},m}^{m-1,m} = \frac{|\Sigma|_m^{(m-1,m)}}{|\tilde{\Sigma}|_m^{(m-1,m)}}\tilde{A}_{\mathcal{Q},m}^{m-1,m}, \tag{4.32}$$

where m is the order of the observable we are interested in.

As a further example, considering the fourth order self energy, in which the overlap we take is with all two point diagrams,

$$\mathcal{A}_{\Sigma_4}^{(3,4)} = \frac{\mathcal{A}_{|\Sigma|_4}^{(3,4)}}{|\tilde{\Sigma}|_4^{(3,4)}}\mathcal{A}_{\tilde{\Sigma}_4}. \tag{4.33}$$

Since we directly record $|\tilde{\Sigma}|_4^{(3,4)}$, we then must use the recursive relationship defined above, to obtain $\mathcal{A}_{|\Sigma|_4}^{(3,4)}$.

Defining $\mathcal{Z}_1 = R(1)Un = \mathcal{A}_{|\Sigma|_1}$, where n is the density given by $\int_{\boldsymbol{k}} G_\sigma^0(\boldsymbol{k}, \tau = 0^-)$, we find

$$\frac{\mathcal{A}_{|\Sigma|_4}^{(3,4)}}{|\tilde{\Sigma}|_4^{(3,4)}} = \frac{R(1)Un}{|\tilde{\Sigma}|_1^{(1,2)}}\frac{|\tilde{\Sigma}|_2^{(1,2)}}{|\tilde{\Sigma}|_2^{(2,3)}}\frac{|\tilde{\Sigma}|_3^{(2,3)}}{|\tilde{\Sigma}|_3^{(3,4)}}, \tag{4.34}$$

and hence our normalised self energy observable is given by,

$$\mathcal{A}_{\Sigma_4}^{(3,4)} = \frac{R(1)Un}{|\tilde{\Sigma}|_1^{(1,2)}}\frac{|\tilde{\Sigma}|_2^{(1,2)}}{|\tilde{\Sigma}|_2^{(2,3)}}\frac{|\tilde{\Sigma}|_3^{(2,3)}}{|\tilde{\Sigma}|_3^{(3,4)}}\mathcal{A}_{\tilde{\Sigma}_4}. \tag{4.35}$$

This example shows explicitly the occurrence of a telescopic product of the preceding ratios of $|\tilde{\Sigma}|$. In simple terms this method boils down to running the Monte Carlo simulation at each pair of subsequent diagram orders up to the required maximum order, such that we have the set of Monte Carlo runs

$$\{(O_1, O_2), (O_2, O_3), (O_3, O_4), \ldots (O_{m-1}, O_m)\}$$

For certain theories, such as the Hubbard model on the square/cubic lattice at half filling, the sum of all odd order diagrams vanishes, and therefore sampling odd orders for normalization purposes is a waste of CPU time. In the future we plan to implement *Add/Remove* updates that traverse multiple orders at once, for such situations. To use this method to normalise we must restrict diagram order to that of the target order k, and $k-1$, therefore we require a valid diagram to start from. The first two order diagrams are easily implemented via momentum conservation rules, and picking random τ values. However for higher orders this is not feasible. We therefore implement a diagram generator Monte Carlo algorithm which is restricted to the updates *Create/Delete Worm*, *Move Worm* (all directions), and *Add/Remove Vertex*, this traverses from $k = 1(2)$, to a user defined $k = n$, and upon reaching an order not reached before, stores the diagram in a HDF5 file. Cloning from a HDF5 file is implemented into the generic algorithm, and the simulation can be started from some arbitrary order using this process. The theory specific details are template parameters to the generator program, and therefore work for any theory. The clone diagram function is based on a *GenericDiagram* pointer, and therefore extending to a new type of diagram is as easy as implementing a single function, with a case definition to call that function.

4.9 Basis Functions - Group Theory

We wish to sample the observables on a minimal set of basis functions that respect the point group symmetry of the underlying lattice. This allows not only efficient storage of data, but a simple way to expand over any path in momentum space desired. The basis functions are used to calculate the overlap with the measurement line each time the measurement line is changed, these are also the basis functions that the *Swap Measurement Basis* update selects from. The approach we have taken allows us to use global basis functions, avoiding binning of the Brillouin zone with basis functions calculated in each bin, which leads to discontinuities of the function between bins. There are also various other problems with binning, such as the size of the bin, and where to place the bin edges.
To obtain the basis functions for point groups requires knowledge of group theory [53, 54], the basics of which will be outlined here.

A *group* is a collection of elements that obey certain rules. To form a group $\mathcal{G}$, elements must be closed under multiplication. There must exist one element, which is the indentity e, that commutes with all other elements. Elements must be associative, and each element must have a reciprocal. Here we are concerned with finite groups of order h. Elements in a group are categorized into classes, and each element corresponds to a symmetry operation. Specifically, we are interested in the point-group symmetry of the Bravais-lattices where symmetry operators perform rotations, reflections, or inversions etc. on symmetry elements, such as points or lines.
A group representation assigns a matrix to each group element in such a way that the multiplication of matrices mirrors the multiplication of group elements
If the representation matrices of the group can be turned into block form via a

similarity transformation they are called a reducible representation, as we can multiply corresponding blocks of each matrix separately. If we cannot find a similarity transform that reduces all matrices of a given representation to block form, then the representation is said to be irreducible (an irreducible representation is often called an irrep). There is a finite set of irreps for each group, which can be found in the literature, that are grouped into *character tables*. The character table of an irrep is obtained by taking the trace of the matrix representation of the symmetry operation R, with $R \in \mathcal{G}$. If we define the symmetry matrix representations $D(R)$, then the character for the symmetry operation i is,

$$\chi(R_i) = \sum_{\alpha} D^i_{\alpha\alpha}(R_i). \tag{4.36}$$

With the character we may define the projection operator,

$$P^i_\alpha = \frac{l}{h} \sum_{R \in \mathcal{G}} \chi^i_\alpha(R) R, \tag{4.37}$$

where l is the dimension of the irrep. This operator transforms a set of basis functions ψ to a new basis ϕ,

$$\phi^i_\alpha = P^i_\alpha \psi^i, \tag{4.38}$$

Where i indexes the irrep, and α indexes the symmetry operation. The new basis functions transform under symmetry operations according to the αth row of the ith irrep. For irreps that have $l > 1$, the projection operator should be applied to each row, creating l basis functions for each irrep.

4.9.1 Spatial basis functions for the square lattice

We define our unadapted basis to be the plane wave (complete) basis

$$f(\boldsymbol{k}, \boldsymbol{r}) = \exp\Big(i\boldsymbol{k}\cdot\boldsymbol{r}\Big), \tag{4.39}$$

where $\boldsymbol{r}$ is a vector of length equal to the dimension we are working in, and consists of lattice positions, which we take as integer values, e.g. $\boldsymbol{r} = (n, m)$ in $d = 2$. By application of the projection operator, we obtain basis functions that transform under symmetry operations corresponding to the irreps. As an example, consider the square lattice, which corresponds to the symmetry group D_4. The D_4 group consists of 8 elements: The identity, three rotations around the principal(z) axis $(\pi/2, \pi, 3\pi/2)$, and four reflections along the x, y, xy, and $-xy$, axes. Application of the projection operator yields six basis functions, that transform according to the D_4 irreducible representations (A_1, A_2, B_1, B_2, E),

$$\phi^{A_1}_{n,m} = N_{n,m}\Big(\cos(nk_y)\cos(mk_x) + \cos(nk_x)\cos(mk_y)\Big), \quad 0 \le m \le n \le r_{\max}. \tag{4.40}$$

The normalisation factor $N_{n,m}$ is obtained by performing the integral $N^2 \int_{\mathrm{BZ}} |\phi(\boldsymbol{r}, \boldsymbol{k})|^2 = 1$, with $N_{0,0} = 1/2\pi$, $N_{n,0} = N_{n,n} = 1/\pi$, and $N_{n,m} = \sqrt{2}/\pi$.

$$\phi^{A_2}_{n,m} = N_{n,m}\Big(\sin(nk_y)\sin(mk_x) - \sin(nk_x)\sin(mk_y)\Big), \quad 1 \le m < n \le r_{\max}, \tag{4.41}$$

with normalisation factor $N_{n,m} = \sqrt{2}/\pi$.

$$\phi^{B_1}_{n,m} = N_{n,m}\Big(\cos(nk_x)\cos(mk_y) - \cos(nk_y)\cos(mk_x)\Big), \quad 0 \le m < n \le r_{\max}, \tag{4.42}$$

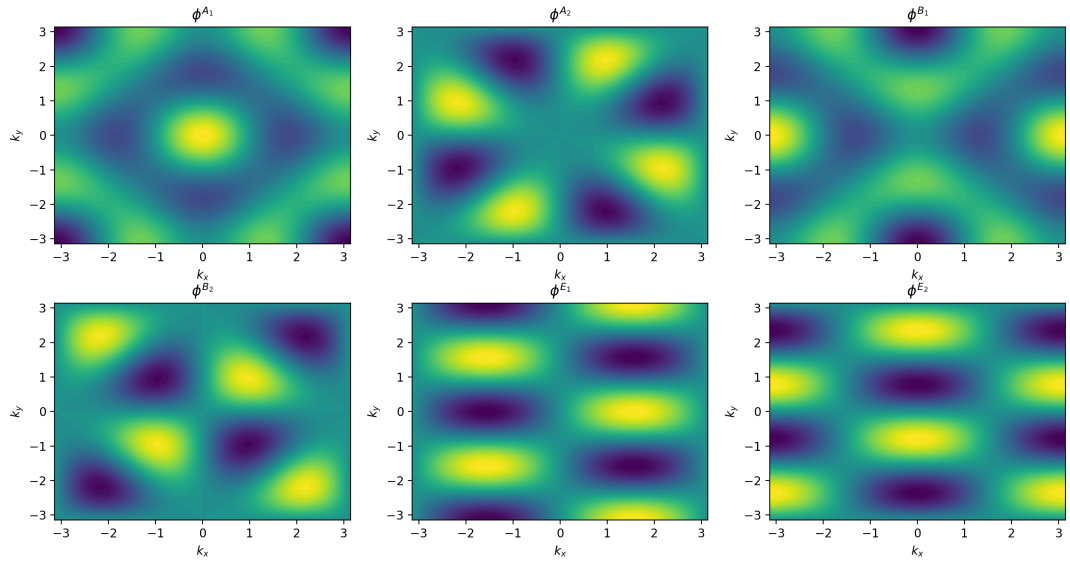


Figure 4.4: Examples of the symmetry adapted basis functions for the D4 point group with $\boldsymbol{r} = (2, 1)$.

with normalisation factors $N_{n,0} = 1/\pi$, $N_{n,m} = \sqrt{2}/\pi$

$$\phi^{B_2}_{n,m} = -N_{n,m}\Big(\sin(nk_y)\sin(mk_x) + \sin(nk_x)\sin(mk_y)\Big), \quad 0 \leq m \leq n \leq r_{\max}, \tag{4.43}$$

with normalisation factors $N_{n,0} = N_{n,n} = 1/\pi$, $N_{n,m} = \sqrt{2}/\pi$. The E basis $\phi^{E}_{m,n}$ is a two-dimensional irrep, and as such we may pick the basis functions corresponding to the projection of each row,

$$\phi^{E_1}_{n,m} = N_{n,m}\sin(mk_x)\cos(nk_y), \quad 0 < m \leq n \leq r_{\max} \tag{4.44}$$

$$\phi^{E_2}_{n,m} = -N_{n,m}\cos(mk_x)\sin(nk_y), \quad 0 < m \leq n \leq r_{\max} \tag{4.45}$$

With $= N_{n,m} = 1/\pi$.

Fig. 4.4 shows an example of the symmetry adapted basis functions implemented in our code. Currently the square, cubic, and triangular point group symmetries D_4,

O_h, and D_6, respectively, as well as the C_2 point group are implemented. The square irreducible representations were calculated by hand, and validated via GTPack [55], whereas the cubic and triangular groups were obtained via GTPack directly. For both the square- and cubic-lattice symmetry basis functions, our current implementation makes use of the high symmetry zone as indicated by the constraint placed on n, m. This is easily expanded upon to consider anisotropic theories, or different hopping terms, by simply defining a derived class and overloading a single function that builds the tuples (n, m) ((n, m, l) in 3D).

4.9.2 Temporal basis functions

For the imaginary time basis functions we have two implementations, the Matsubara representation, or the discrete Lehman representation(DLR) [56].
The Matsubara basis,

$$u(\tau) = \sum_{i\omega_n} e^{i\omega_n \tau}, \tag{4.46}$$

where $i\omega_n = (2n+1)\pi T$, is the simplest of the temporal basis functions implemented in the code, with implementations for:

- All Matsubara frequencies in a user defined range $[n_{min}, n_{max}]$
- A dense + sparse grid implementation where all frequencies in the range $[n_{min}, n_{max,d}]$ are defined, and then sparse Matsubara frequencies up to the cut off $n_{max,s}$.

The DLR basis is derived directly from the Lehman spectral representation [56],

$$G(\tau) = \int_{-\infty}^{\infty} K(\tau, \omega)\rho(\omega)d\omega. \tag{4.47}$$

Here $\rho(\omega)$ is the spectral weight, and the (fermionic) kernel K is,

$$K(\tau, \omega) = \frac{e^{-\omega\tau}}{1 + e^{-\beta\omega}}. \tag{4.48}$$

Construction of this basis is achieved by performing interpolative decomposition, which gives the Green's function in the DLR basis as,

$$G_{DLR}(\tau) = \sum_{l}^{r} K(\tau, \omega_l)\hat{g}_l, \tag{4.49}$$

where l denotes a frequency from a given set $\{\omega_l\}_{l=1}^{r}$, and $\hat{g}_l$ are some coefficients to be determined. The DLR library [56] defines operations to perform transformations to the Matsubara frequency domain in a self contained fashion. All that is required is to sample G at the grid points produced by the discretization to obtain the DLR coefficients $\hat{g}_l$. We implement an interface between our code base and the FORTRAN DLR library that is easy to use. At the time of writing the DLR library has been updated to include a C++ implementation, which we endeavour, in the future, to integrate into the project.

4.10 Measurements

A large part of the simulation run time is spent recording observations, and therefore we wish to optimize this process. With a naive measurement process we would

measure the diagrams value after every Monte Carlo update. This, however, would be very inefficient. We therefore implement the so called 'buffered measurement technique'.

The measurement line only depends on the external momentum and imaginary time of the diagram, therefore a Monte Carlo move that only alters internal variables does not affect the measurement line. We can use this property to perform buffered measurements such that we only record measurements each time the measurement line is changed. To do this we simply store a count of the number of positive, and negative diagrams, along with their weight until the measurement line is changed, resulting in a single measurement record. What we actually record in our observables is

$$q(Y) = (n_p - n_n)R(\mathcal{C}) \tag{4.50}$$

where n_p is the count of number of positive diagrams recorded, and n_n the number of negative diagrams. This greatly reduces the required number of recordings of measurements during each run, especially since the measurement line may not be altered for a large amount of updates at high orders.

As mentioned above we may also include a random basis function in the weight of each MC configuration the diagram, which can be altered by the *Swap Measurement Basis* update. The inclusion of a basis function, chosen randomly from the set of point group symmetry basis functions used – we may define a single basis function as the product of a spatial and temporal basis function, or simply as a spatial basis function – avoids the need to expand each measurement over all basis functions. This drastically reduces the number of operations required as there can be a very large number of basis functions required for low symmetry systems.

4.11 Autocorrelation time

Autocorrelation effects are measured by a simple analysis of how long the simulation takes to go from the lowest order diagram allowed, to the highest, and back. When initializing from a first order diagram, we only have a single free parameter, the external momentum, traversing orders almost guarantees that the parameters are different by the time the first order is reached again. In general this is achieved in a very short time, and to avoid autocorrelation effects we define a thermalisation stage of the simulation that performs all updates defined, but does not record any measurements. This value will of course depend on the parameters used for the simulation in hand, but in any case, it should be set to a value larger than the time taken for a round trip.

In cases where the max order is separated largely from the lowest order, we can find that we rarely sample low order diagrams. This is due to the combination of the $n!$ scaling of number of diagrams with order, and higher order diagrams carrying significantly more weight than lower orders. We use a reweighting function ($R(\mathcal{C})$) defined in section 4.8, that may be tuned to alter the weight of specific configurations. The re-weighting is used to make certain orders appear more in the Markov chain. The use of the order-by-order normalisation method reduces the utilisation of the re-weighting function, however it is a necessity when running shifted action simulations described in section 4.13.

4.12 Error calculations

Whilst we perform a thermalisation phase at the start of each simulation, Markov chain samples are not completely independent. To reduce the effects of correlations, we calculate variance using resampling techniques. Resampling techniques estimate statistical properties by sampling subsets of the recorded data and calculating averages over all subsets. This leads to better variance estimates, and a reduction in bias when compared to the standard estimator. The estimator implemented for calculating self-energy is the jack-knife [57]. The jack-knife estimator works by calculating the mean over all samples when a single sample is left out. This is an unbiased estimator for linear functions, such as the self-energy. The jack-knife sub-sample average is given as,

$$\bar{x}_{(i)} = \frac{1}{m-1} \sum_{k \neq i}^{m} x_k, \tag{4.51}$$

where m is the number of independent and identically distributed(i.i.d) samples. This is the standard mean with the sample $i = k$ removed. The estimator is then calculated by taking the mean of the jack-knife sub-sample averages,

$$\bar{x}_{jack} = \frac{1}{m} \sum_{i} \bar{x}_{(i)}. \tag{4.52}$$

This is performed during the simulation by binning y observations and performing the jack-knife analysis over all bins. The idea being that when simulations are carried out, M threads are run simultaneously, and then the mean over threads is taken via a post processing step. The error value we use is then calculated via the variance of

the jack-knife average,

$$\mathrm{var}(x_{jack}) = \frac{m-1}{m}\sum_{i=1}^{m}(\bar{x}_i - \bar{x}_{jack})^2. \tag{4.53}$$

4.13 Shifted action

The most relevant draw-back to diagMC methods is the possibility of having a divergent series. It is, in general, not possible to determine if the series will converge *a-priori*, and therefore knowledge of resummation methods are required for using DiagMC to investigate strongly correlated systems in earnest. It is possible that the divergence of the series is not one of physical nature, i.e not due to a phase transition. In cases like this, the series diverges in the complex plane of the interaction. The homotopic action formalism [58] is an approach to deal with such situations. The approach combines homotopy, shifted-action [59], and conformal mappings [60] to produce a non-diverging series – in the case where the series generated by a shifted action series can be mapped to a convergent series. We implement the simplest homotopic action approach; the shifted-action approach. As the name suggests, the shifted-action approach starts with the action, and introduces extra bilinear terms causing a shift. For a generic fermionic action of the form,

$$S[\phi] = S_0[\phi] + gS_{int}[\phi], \tag{4.54}$$

where S_0 is bilinear in Grassman fields, and S_{int} is the interaction term that is greater than bilinear in Grassman fields, we introduce an extra term that is also bilinear in Grassman fields, that can be written as a Taylor series. This along with an auxiliary

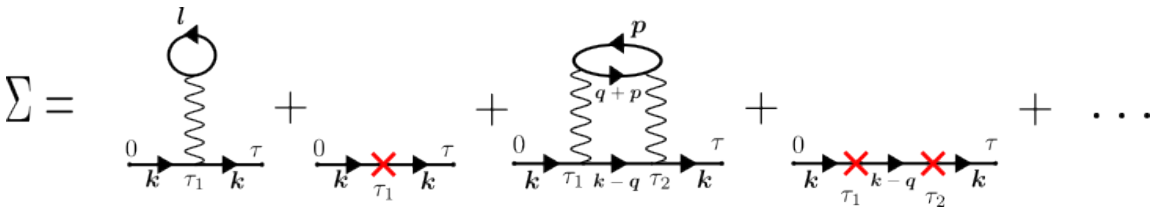


Figure 4.5: The set of first and second order diagrams sampled for a shifted action expansion for the Hubbard Model. Red crosses indicate α counter terms.

variable ξ gives action,

$$\tilde{S}[\phi, \xi] = \tilde{S}_0[\phi] + \lambda[\phi; \xi] + g\xi S_{int}[\phi], \tag{4.55}$$

which reduces to the original action when $\xi = 1$, via $\tilde{S}_0[\phi] + \lambda[\phi; \xi = 1] = S_0[\phi]$, e.g. $\tilde{S}[\phi, \xi = 1] = S[\phi]$. The diagrammatics are now performed in powers of ξ, around $\tilde{S}_0$. Whilst there are no limitations on the form of $\tilde{S}_0$, a simple linear shift has been shown to improve convergence properties [61]. The propagaor in the shifted-action formalism becomes,

$$\tilde{G}_0(\boldsymbol{k}, \omega) = \frac{1}{\omega - \epsilon_{\boldsymbol{k}} - \alpha}, \tag{4.56}$$

where α is devoid of labels since its form, and dependencies are arbitrary.

In this formalism we are now effectively summing the series, along with counter terms (see Fig. 4.5), around the shifted starting point $\tilde{S}_0$. The self energy of the shifted series is,

$$\Sigma(\boldsymbol{k}, i\omega_n) = \sum_{m}^{M} \tilde{a}_m(\boldsymbol{k}, i\omega_n)\xi^m \tag{4.57}$$

Where $\tilde{a}_m$ is the sum of all diagrams contributing to a_l, with l running from $1 - m$, along with the sum over all possible permutations of diagrams with $m - l$ insertions of α. Where a_l is the sum of all 1PI diagrams at order l.

The crux of this formalism is that the configuration space of all diagrams increases,

since we now must account for counter terms. Wu *et al* [61] have developed a recursive formula to lessen this problem which we implement in our code. The idea is to implicitly include lower order diagrams by dressing a certain number of propagators with self energy insertions. For a diagram of order m, we use the previous orders n, where $n < m$ to dress p lines via,

$$G^{(p)} = \sum_{n}^{p} G^{(n)} \tilde{a}_m \xi^{p-n} \tilde{G}_0, \ p > 0. \tag{4.58}$$

The self energy is then obtained by summing the skeleton series of orders $[1, m]$, where the total dressing of lines follows $\sum_i p_i = m - l$.

In practice, this results in sampling, for a given order k in an expansion of ξ, all orders of interaction up to and including k. While sampling for the kth order, the diagrams only contain $\tilde{G}_0$ propagators as each vertex carries an order of ξ. An example of low order diagrams for the Hubbard model is shown in figure 4.6.

4.13.1 Updates

The updates for the shifted action method are generally the same as the generic updates, however we must now harmonize the dressing orders of propagators to ensure we are always sampling at the specified order of ξ.

We employ the convention that the measurement line is always a bare propagator, and dressings can be placed on any other line in the diagram. We allow the worm to carry dressing, such that it can propagate the dressing across the diagram without introducing an extra move to do so – although an extra move was added for testing purposes. When the worm is created on a vertex slot, the worm obtains the dressing

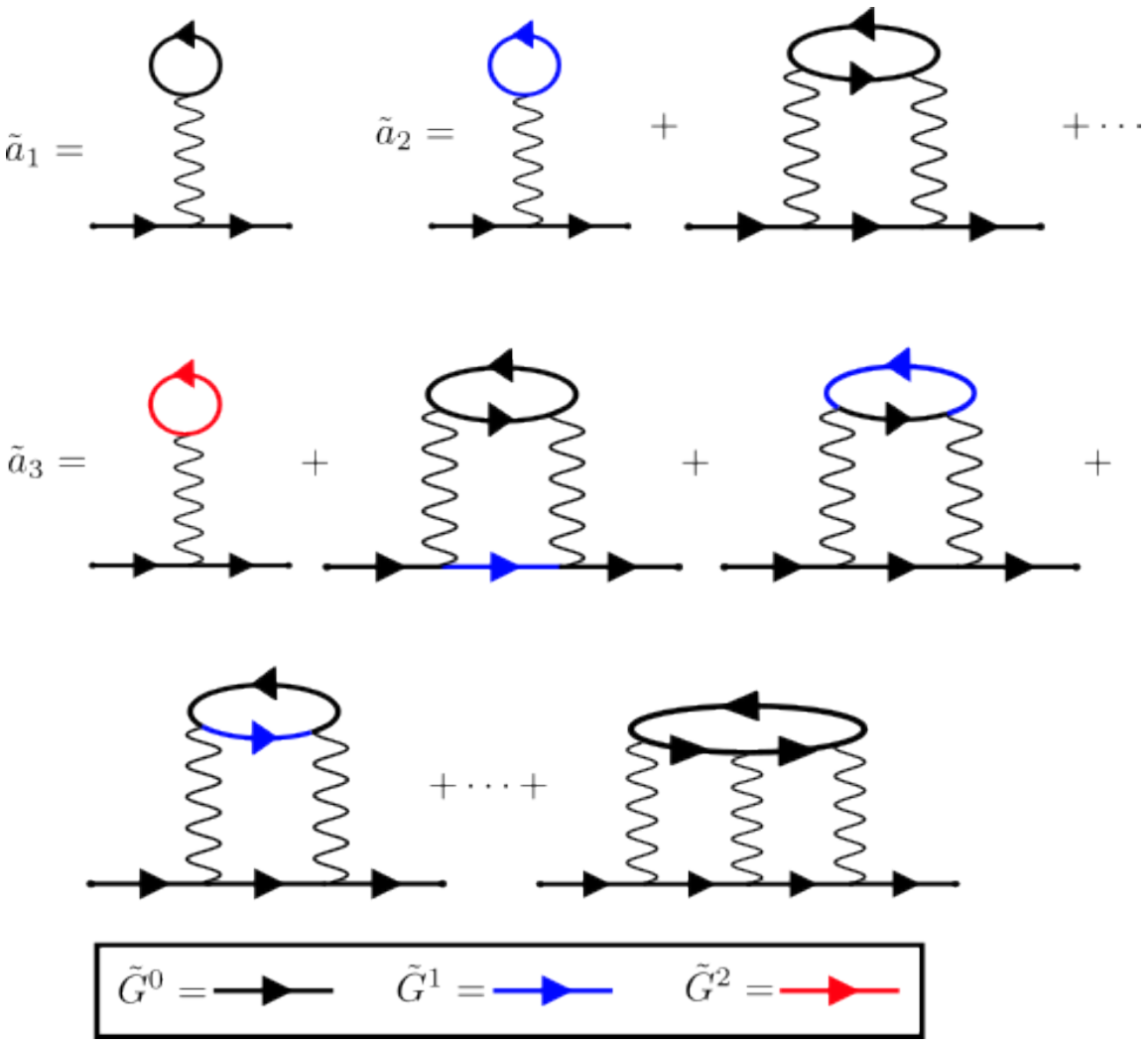


Figure 4.6: Low order terms of diagrammatic expansion in ξ via shifted-action recursive method. Black lines represent bare propagators, blue lines represent $\tilde{G}^{(1)}$ i.e. dressed with $\tilde{a}_1$, and red lines $\tilde{G}^{(2)}$ i.e. dressed with $\tilde{a}_2$

.

of the propagator that is connected to that slot. The propagator gives up all dressing orders and is recalculated as $\tilde{G}_0$. When the delete worm update is successful, the converse of this process happens and the propagator connected to the slot gains the worm's dressing. The only difference in acceptance ratio when compared to the

updates for the bare vertices is that G_0 can now be of the form $G^{(n)}$.

The *Add/Remove Vertex* update now must consider all possible ways to distribute the dressings, d, contained in the worm if $d > 1$. If the worm only contains a single dressing power this is implicitly included by the newly added vertex, whereas for $d > 1$, we can choose any of the four propagators connected to the new vertex to dress, or even split up the dressing and dress multiple propagators with dressing d_i, such that $\sum_i d_i = d - 1$.

Chapter 5

Benchmarks

In this chapter we show data for the Hubbard model on a square lattice at half filling to confirm the validity of our implementation.
Practically, we accumulate data for multiple independent threads via the parallel package [62] and collate results via a custom script. All data has been obtained using our local high powered computers – Intel Server Systems with dual Intel(R) Xeon(R) Gold 5318Y CPUs and 256GB DDR4 RAM, up-kept by Gunnar Möller.

5.1 Square Lattice Hubbard Model

5.1.1 Low Order Contributions

In Fig. 5.2 we reproduce the second-order contribution to the self-energy as a function of Matsubara frequency at the nodal, $\boldsymbol{k}_N = (\pi, 0)$, and anti-nodal, $\boldsymbol{k}_{AN} = (\pi/2, \pi/2)$

points, for various temperatures, at $U = 2$, as shown in Ref. [17]. For high temperatures the second order contribution is large when compared with higher orders, and reproduces the full self -energy very well. As temperature decreases the self-energy differs from second order contributions, although not appreciably at first. For lower temperatures the second order contributions do not capture the insulating behaviour of the self energy, which is indicated by $\mathrm{Im}\Sigma(\boldsymbol{k}, i\omega_0) < \mathrm{Im}\Sigma(\boldsymbol{k}, i\omega_1)$ for inverse temperatures of $\beta \gtrsim 4.0$.

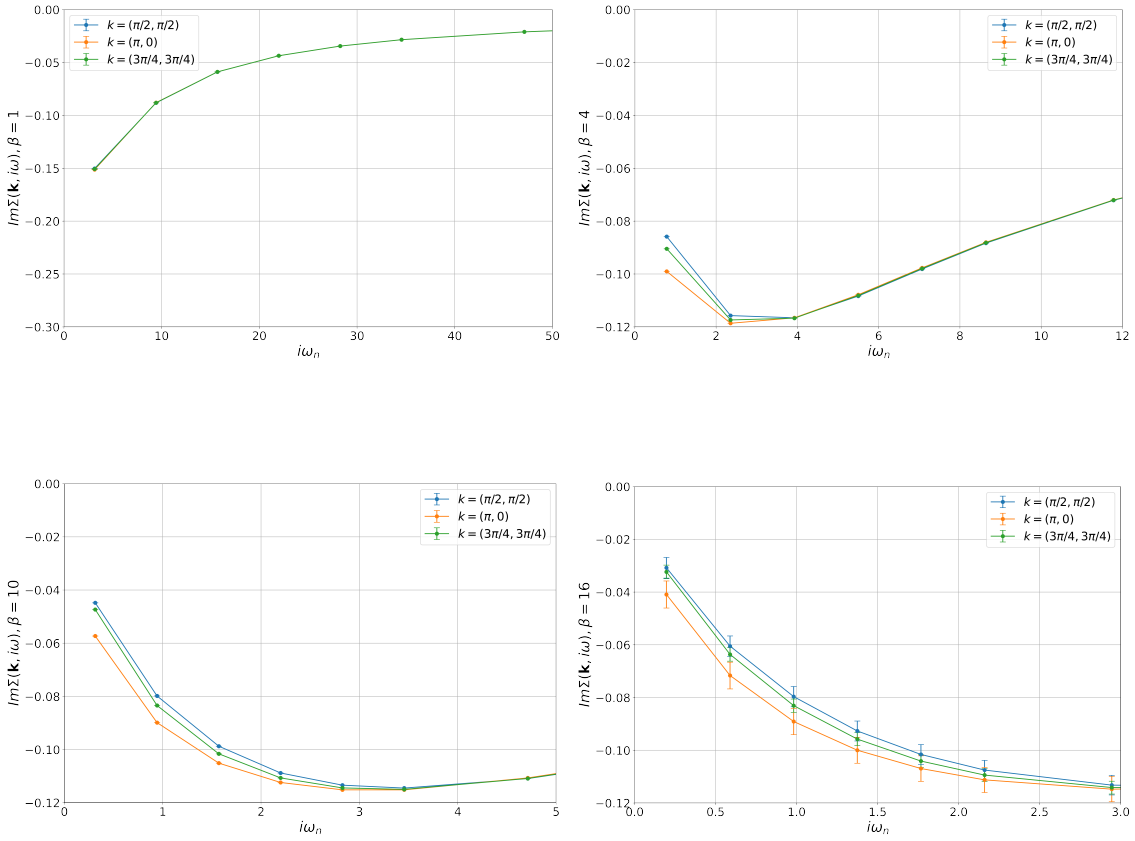


Figure 5.2: Second order contribution to the self energy at the nodal $\boldsymbol{k}_N = (\pi, 0)$, and anti-nodal $\boldsymbol{k}_{AN} = (\pi/2, \pi/2)$ points, as well as a generic point $\boldsymbol{k}_N = (3\pi/4, 3\pi/4)$ for various temperatures

5.1.2 Comparison With Other Diagrammatic Methods

Ref. [63] is a benchmarking paper that brings together results from diagMC, Dual Fermion (DF), dynamical vertex approximation (DΓA), and dynamical cluster approximation (DCA). We reproduce Fig.17 which shows the imaginary part of the self energy for the six lowest matsubara frequencies obtained via these methods. We overlay our results (Fig. 5.3) showing excellent agreement with DF and DΓA. Both these methods perform expansions via two-particle vertex functions, and it has been shown that for the square lattice Hubbard model, the results should be very similar to those obtained via an expansion in one-particle irreducible self-energy diagrams [47].

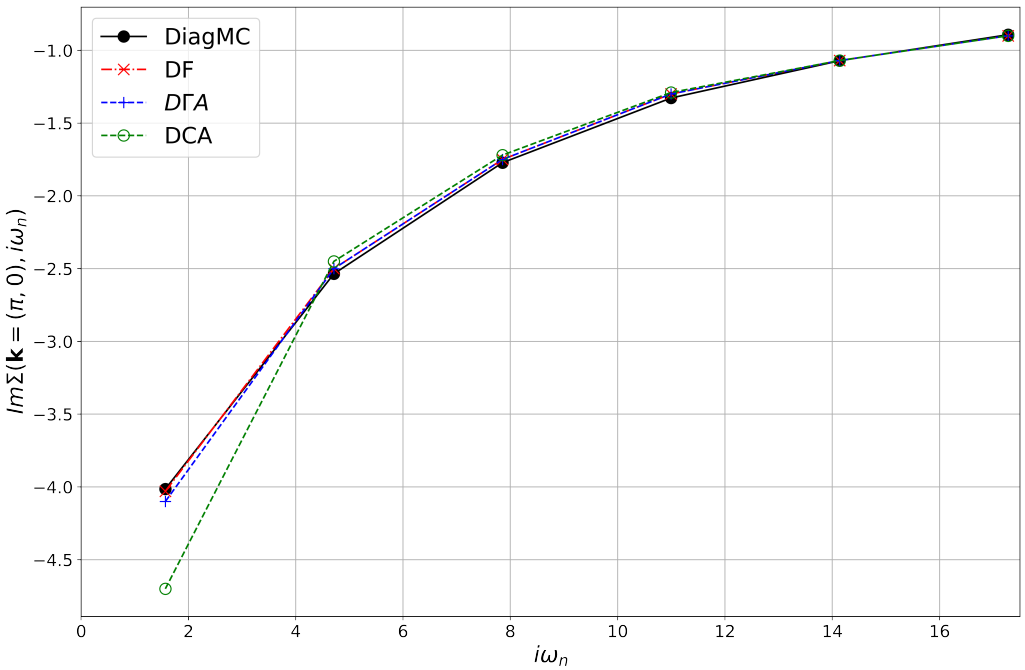


Figure 5.3: Comparison of self-energy obtained via diagMC, DF, DΓA, and DCA for half filling at $\beta = 2$.

5.1.3 Momentum Depedency of the Self-Energy

The following data we benchmark against was kindly provided by E. Kozik, is taken from Ref. [39], and produced via a DDMC implementation. In figures 5.4, 5.5, 5.6 we present the full momentum depdendence of the self-energy at the lowest Matsubara frequency, ω_0, for $\beta = 1.25, 2.0, 5.0$, at $U = 4, 8$ inclusive of order $N = 6$ along the high symmetry path $\Gamma \to X \to M \to \Gamma$. Note that by projecting onto symmetry adapted basis functions we may construct the self-energy to arbitrary momentum precision. We find that we can accurately reproduce reference data with 20 points for each 'leg' on along the high symmetry path.

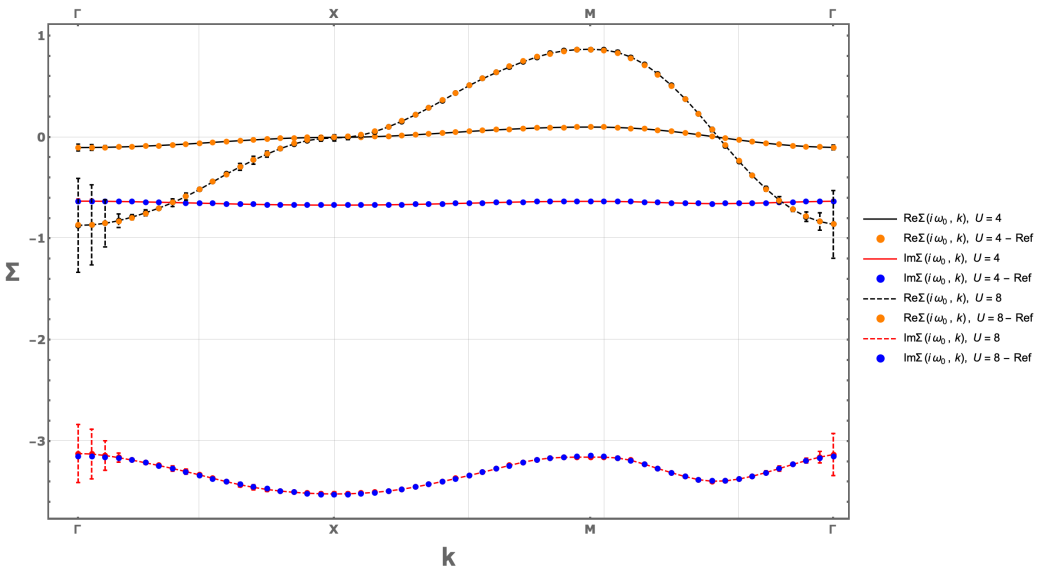


Figure 5.4: Benchmark Data for $\beta = 1.25$, With ReΣ for $U = 4$ (black), and $U = 8$ (black, dashed) and ImΣ for $U = 4$ (red), and $U = 8$ (red, dashed), and the corresponding reference data shown as points.

We are able to reproduce the full momentum dependence of the self-energy for various U values, where error bars could be further reduced by running higher-order calculations for longer, or by employing more threads per run. This data supports

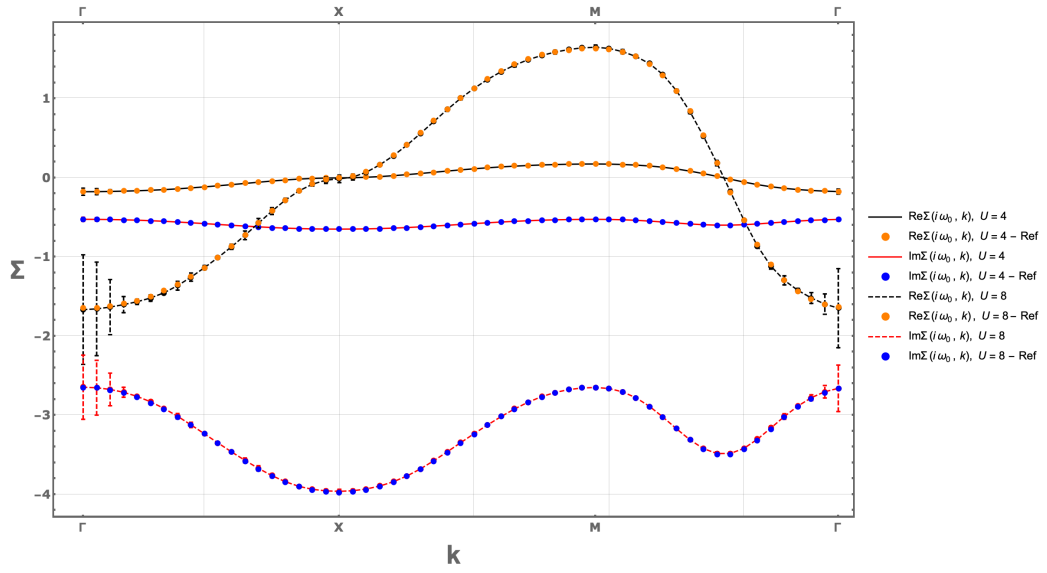


Figure 5.5: Benchmark Data for $\beta = 2.0$, With ReΣ for $U = 4$ (black), and $U = 8$ (black, dashed) and ImΣ for $U = 4$ (red), and $U = 8$ (red, dashed), and the corresponding reference data shown as points.

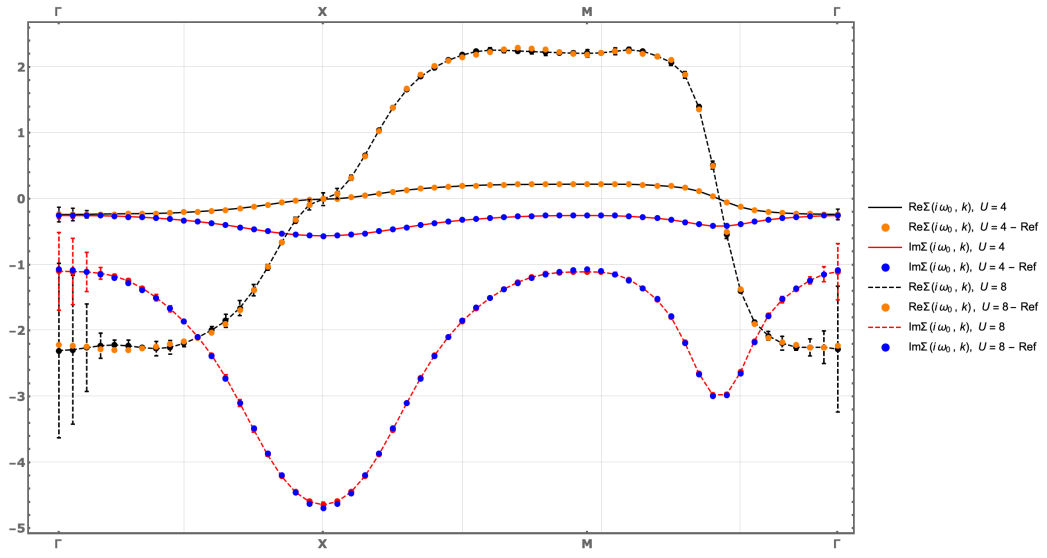


Figure 5.6: Benchmark Data for $\beta = 5.0$, With ReΣ for $U = 4$ (black), and $U = 8$ (black, dashed) and ImΣ for $U = 4$ (red), and $U = 8$ (red, dashed), and the corresponding reference data shown as points.

the implementation of suppression of tadpole diagrams, which requires running the simulation with a shifted chemical potential, $\mu' = \mu - Un_\sigma$. We note that the level of agreement here is very good, with only minor deviations at $\beta = 5.0$. This is a non-trivial benchmark, since these results requires the summation of a large number of graphs – in general the number of graphs increases factorially with the diagram order. The results indicate that our updates are functioning as intended, which is a difficult task to test, especially for the case of the *Reconnect* update, which is only called for diagrams of order 3 and greater. Furthermore, we require accurate sampling to make odd-order diagrams vanish when summed, which is the case for the square lattice model at half filling.

5.1.4 Momentum Distribution Function

Finally, in Fig. 5.7 we show the momentum distribution function $n(\boldsymbol{k}) = G(\boldsymbol{k}, \tau = 0^-)$ at various temperatures which closely follows results reported in Ref. [64]. The data was obtained by calculating Dyson's equation with the self-energy projected onto DLR basis functions (see section 4.9.2) [56]. G is most easily solved in frequency-momentum space, as it becomes an algebraic function, solved via a scalar inversion. The tail of G decays as $1/\omega_n$, and we therefore calculate $\Delta G(\boldsymbol{k}, i\omega_n) = G(\boldsymbol{k}, i\omega_n) - G_0(\boldsymbol{k}, i\omega_n)$ on a momentum grid, as a more stable function to perform simulations with, due to better stability when performing the numerical Fourier transform. We then perform the fourier transform back to imaginary time to obtain $\Delta G(\boldsymbol{k}, \tau)$. Figure 5.7 shows the sharpness of the Fermi surface increasing as temperature decreases, where the 'width' of the step is proportional to $1/k_B T$ with k_B the Boltzmann factor.

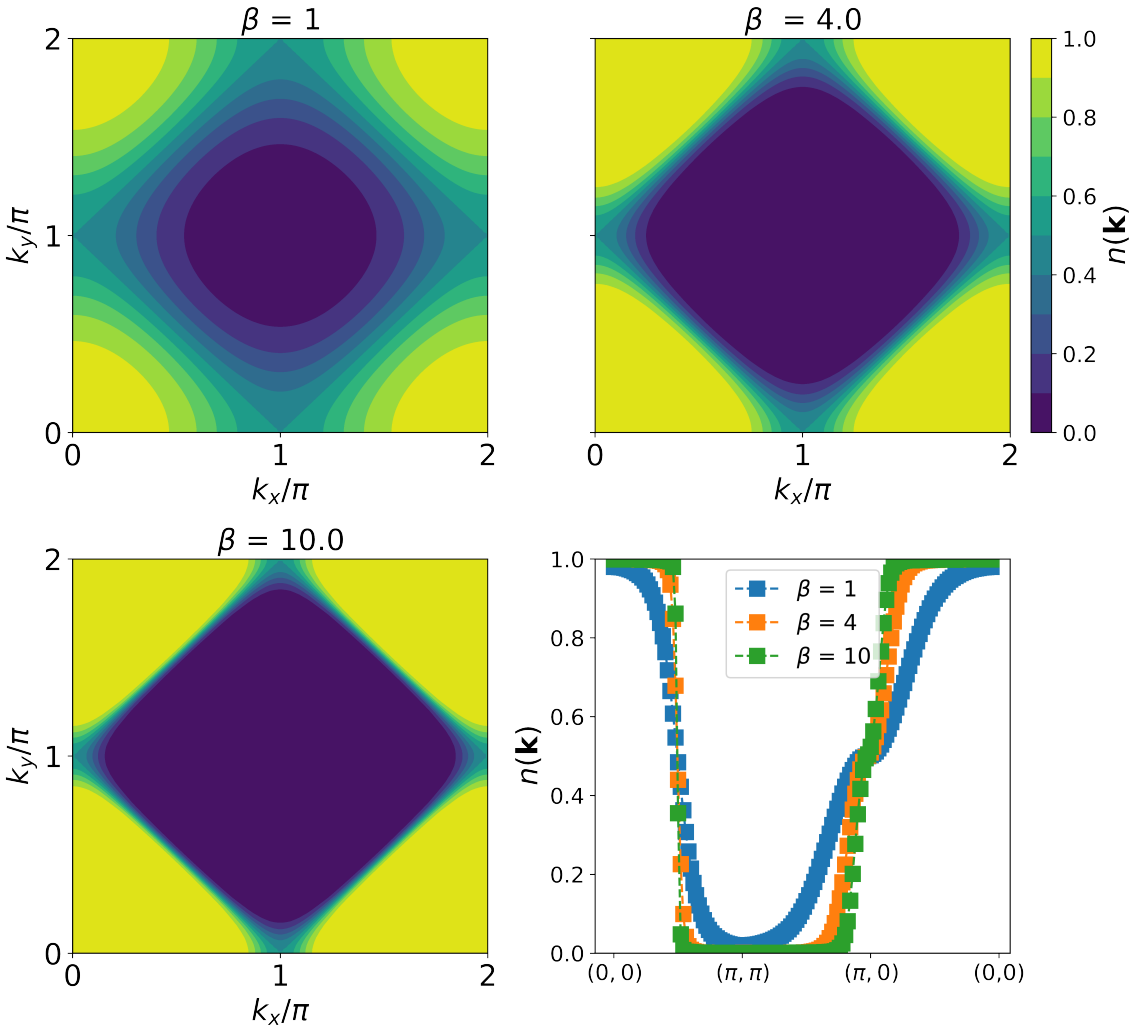


Figure 5.7: The momentum distribution $n(\boldsymbol{k})$ for different temperatures, showing the sharpness of the Fermi surface increasing with decreasing temperature.

Chapter 6

Anisotropic Triangular Hubbard Model Investigation

In recent years there has been much interest in 2d materials both theoretically and experimentally. Interacting quantum systems in two dimensions are in a strong quantum regime, located between exactly solvable systems in 1D and typically more mean-field like behaviours found in 3d. Their importance has been highlighted by the discovery of high-Tc superconductors which are composed of 2d Cu-O_2 layers [65]. Many magnetic materials with triangular lattices have been subject to experimentation, such as, the organic salt family κ-(BEDT-TTF)X [66–70] – for which it is found certain compounds X have an isotropic triangular lattice structure, whilst others can be modelled anisotropically – $NaYbO_2$, and Cs_2CuCl_4 for example. These materials exhibit geometric frustration, electron itineracy, and are in the strongly correlated regime. Subsets of the κ-X family have been shown to exhibit no magnetic ordering down to low temperature, and are thought to be quantum spin-liquid

candidates [70–72]. Moreover, these materials show metallic, insulating, and superconducting phases [73, 74], and therefore are of great interest.

Theoretically, the investigation of models including geometric frustration is of interest, as the formation of long-range order at finite temperature causes instability towards magnetic states which usually precludes the Mott transition. Geometric frustration suppresses long range order offering the possibility of a non-magnetic insulating (NMI) ground state. Theoretical studies of the isotropic case, $t' = 1.0$, at half filling [36, 68, 75–97], performed via various different methods provide varying results, such that the exact nature of the transition from metallic to insulating state is up for debate. Several DMFT studies [4, 98–102] report a first-order MIT indicated via a discontinuity in the double occupancy, along with hysteresis between metallic and insulating states occuring for $U_c \approx 8.0t$. Upon heating, the first-order transition ends in a critical point at $T = 0.1t$ [96, 102], with an associated Widom line [103, 104] – A Widom line is a high temperature remnant of a lower temperature first order phase transition, marked by the maximal response of a thermodynamic observable such as double occupancy – such that the double occupancy can be treated analogously to the density order parameter in a liquid-gas phase transition [105] – However DMFT approaches overestimate the ordering of the phases due to lack of non-local correlations, and its MF nature, often finding a first order transition where other approaches do not. A DMRG [106] study finds two first-order transitions in the ground state with $U_{c1} \approx 7.9t$, and $U_{c2} \approx 9.9t$. In contrast, a dual-fermion (DF) study [8], and a recent study applying minimally entangled thermal typical states (METTS), cluster DMFT, and DiagMC, finds the evolution from metallic to insulating state to be a crossover, down to temperatures of $T = 0.025t$ [36] occurring at $U_c \approx 8.4$. Furthermore, investigations of the existence of the spin-liquid phase occurring at the transition/crossover point are inconclusive. Studies carried out using Variational

Cluster approximation (VCA) [77, 84, 90], DMRG [106], path-integral renormalization group [97], Dual Fermion (DF) [107], and the prior mentioned METTS techniques suggest an evolution from metallic directly to spin-liquid phase prior to onset of QAFM, along with evidence suggesting that the spin-liquid is of chiral nature [92]. However, DCA [8], Variational Monte Carlo (VMC) studies [79, 108], and a (different) DF study [9], find no evidence of a spin-liquid state, with evolution from metallic to to 120° degree QAFM. Interestingly, the VMC studies disagree with each other, Ref. [108] finds a spin-liquid state existing from $t' = 0.75$ to asymptotically close to the isotropic limit with the spin-liquid forming after the formation of the 120° QAFM state as a function of U, which is the opposite behaviour found by other studies, whilst Ref. [79] finds no existence of a spin-liquid state at any t' for all U. Furthermore, the critical interaction strength U_c reported from various studies varies over the range $U_c = 5.14$ to $U_c = 15.8$ [83].

Away from the isotropic triangular limit, the literature finds more agreeable results. At $t' = 0$ (square lattice limit) the system is unstable toward Néel QAFM for an infinitesimal U. As t' increases, geometric frustration suppresses magnetic ordering and stabilises the metallic phase for finite U. The evolution from metallic to insulating state occurs at increasing values of U_c with an increase in t', and coincides with the formation of Néel QAFM [90]. The Néel order is found to be robust and exists until $t' \approx 7.0$ [9, 109]. For $t' > 0.7$ the Néel peak begins to move away from the M'-point toward the K-points, becomming commensurate with K at $t' = 1.0$. A comprehensive study employing DMRG [93] provides phase diagrams for the anisotropic lattice on different cylinder geometries. However, a main limitation of matrix-product state approaches, is that the complexity scales exponentially with the circumference of the cylinder geometry [92]. As a result, studies were limited to consider finite-circumference cylinders with $L_y \leq 6$, which exhibit strong finite size

effects, and the phase diagram differs quite drastically as the cylinder circumference is increased.

From the above summary of the literature to date, it is clear that the exact nature of the phase transition, and indeed the phases that occur, is still contested, unlike that of the square lattice. Moreover, to the author's knowledge, DiagMC has only been applied in a single case, in which it was used as an auxiliary method [36], providing motivation to study the phase transitions of the Hubbard model on an anisotropic triangular lattice via the finite-size effect free, cDet alogirthm.

In the following, we work in units where t, $\hbar$, and the lattice constant are set to unity. Therefore, μ, U and t' are in units of t. We concentrate on the range $0.6 \leq t' \leq 1.0$, as the Néel state is found to be robust for t' less than this; furthermore, no indications of a NMI state have been found for smaller values of t'. However, we show results for smaller t' at lower temperatures.

As mentioned previously (see chapter 3 section 3.2), cDet is performed in real space, and we tabulate the Green's function on a finite lattice. However, this is an effective thermodynamic limit since we can ensure that all vertices fall within the calculated range, or choose a range such that vertices that fall outside that range carry very little weight, and therefore provide only a fraction of the contribtuion to the observable. We calculate the matrix of Green's functions on a grid of $N_G \times N_G$ lattice points taking $N_G = 64$, and perform the MC simulations on a lattice of $L_x \times L_x$ sites, with $L_x = 126$. A large value of L_x ensures that the vertices, whose initial vertex positions are drawn using a triangular Gaussian distribution centred on $Lx/2$, can move around the lattice without reaching the boundary causing finite size effects. Any two interaction vertices that are spatially separated by $r_j - r_i > N_G$ are not drawn via the MC updates, as the Green's function connecting them is truncated

to zero, giving the diagram zero weighting, and hence the update zero acceptance ratio. With the values chosen, we find that all diagrams fall fully inside the $N_G \times N_G$ grid, such that no truncation occurs for all calculated orders. The value $N_G = 64$ was obtained by computing the Green's function on increasing grid sizes until the magnitude was below the threshold of 10^{-14} at the maximum spatial extent. This was carried out with $t' = 1.0$ as the isotropic triangular lattice Green's functions have a greater spatial extent than those of the square lattice, in which the threshold is met by $N_G = 24$. The larger spatial extent of the Green's function results in series coefficients being 'harder' to calculate as t' increases, as diagrams with larger spatial extent carry more weight i.e. non local effects become more prominent. As an example, we can obtain similar error bars for series coefficients at $t' = 0$, with a factor of 10 less MC samples when compared to $t' = 1.0$. For reference, Ref. [26] calculates observables on the cubic lattice with a grid of $N_G = 42$, whilst Ref. [110] finds $N_G = 20$ sufficient to not encounter finite size effects. The value L_x was obtained by running test simulations at high orders e.g. $N = 7$, at increasing values of L_x, until no measurements are recorded for r_x, r_y close to the lattice edges.

6.1 Results

6.1.1 Density

As described in chapter 3 density is an uncontrolled parameter for a system without particle-hole symmetry in the standard cDet implementation. The series expansion for the density is oscillatory in nature such that convergence is not achieved via partial summation to any order [111], see Fig. 6.1. As temperature is decreased higher orders

start to diverge – Note that for all figures presented if the error bars are not visible they are smaller than the marker size. However, the series are resummable via the

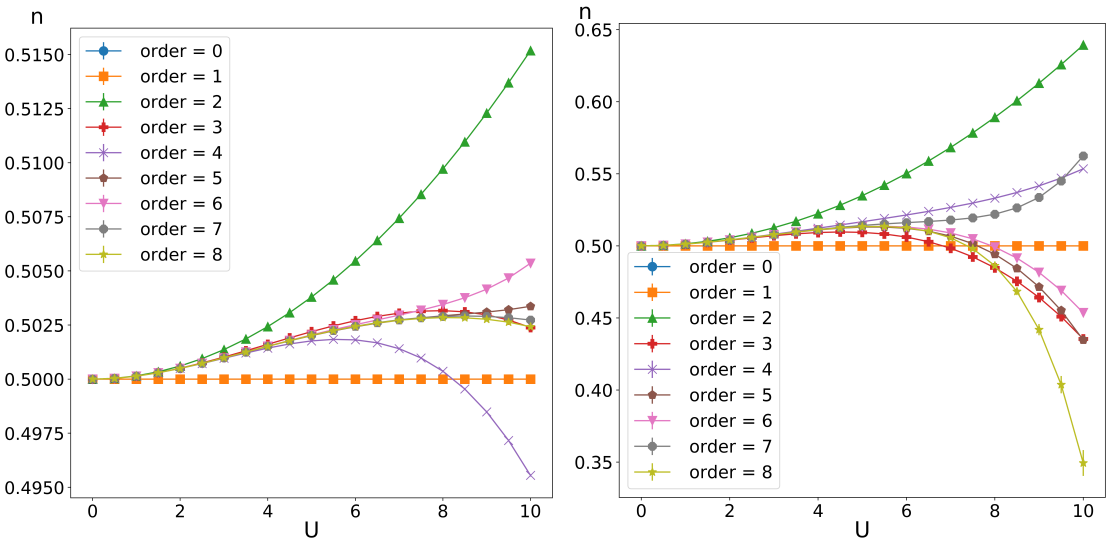


Figure 6.1: Left: partial summation of density at $\beta = 0.5$, for μ corresponding to half filling in the non-interacting limit. Right: same as left at $\beta = 2.0$. Note the overlap of the 0th and 1st order, as we nullify tadpole diagrams via an alpha shift such that the first order contribution is zero.

Dlog-Padé approximant [112, 113]. As the temperature is further decreased, the Dlog-Padé approximant begins to fail due to an increasing number of singularities occurring close to, or on the real axis. The singularities that occur are not physical, as they do not persist upon changing the values of N, M. Due to the singularities we are limited to temperatures of $\beta \leq 2.0$ for density calculations at large U. We are unable to achieve converged results for lower temperatures due to difficulties calculating high orders with error bars that are manageable for resummation techniques.

At $\beta = 0.5$ in the range of U we investigate, the density is a monotonic function that increases with U, see left of Fig. 6.2. Decreasing the temperature to $\beta > 1.0$, the density becomes non-monotonic, suggesting a change in physics as β increases

past this point. This value coincides with that found in Ref. [85], where the Mott insulating state is found to extend up to $\beta \approx 1.0$ for large U. Non-monotonic behaviour of density has been found to indicate the onset of phase separation – The coexistence of two phases via the formation of 'droplets' of one phase embedded in the other phase. However, we find no evidence of a first-order transition in any observable calculated. The right-hand side of Fig. 6.2 shows the non-monotonic behaviour at $\beta = 2.0$. The density curves for different μ values close to half filling begin to converge as U is increased, suggesting electron localisation, and a reduction of the compressibility of the system, via the relation $\kappa = dn/d\mu$. The reduction of compressibility is an indication of evolution toward a Mott insulating state [4]. We find that this behaviour persists as t' is reduced, down to $t' = 0.6$ (smallest t' calculated here); furthermore, as t' is reduced, the value U at which the curves begin to converge is reduced. The convergence of the density indicates an initial crossover value, from metallic to insulating states, of $U \approx 8.5$.

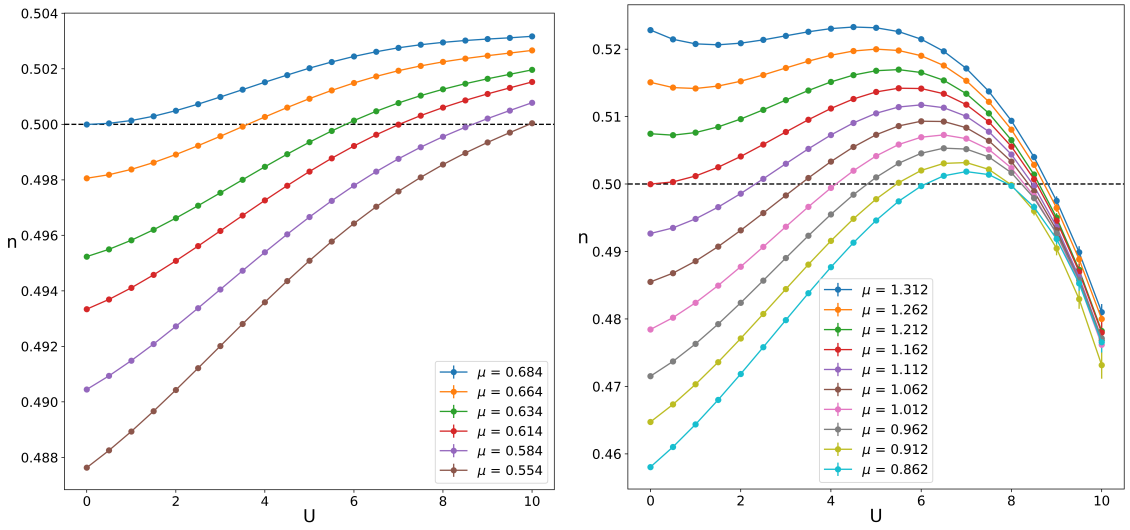


Figure 6.2: Left: Density extrapolated to infinite order via Dlog-Padé for various chemical potentials at $\beta = 0.5$. Right: same as left at $\beta = 2.0$

6.1.2 Double occupancy, Potential energy, and Kinetic energy

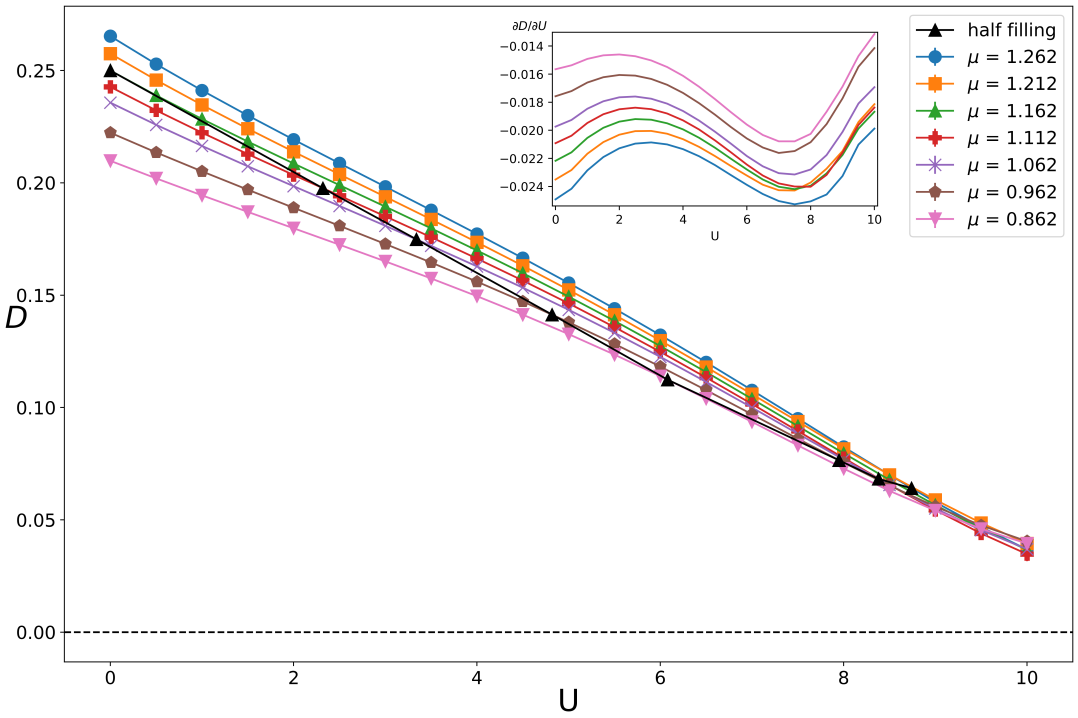


Figure 6.3: Double occupancy extrapolated to infinite order via Dlog-Padé for various chemical potentials at $\beta = 2.0$. The black line with triangular markers indicates double occupancy at half filling. Inset: derivative of D with respect to U.

Figure 6.3 shows the double occupancy as a function of U for various chemical potentials close to half filling at $\beta = 2.0$, $t' = 1.0$. The non-interacting limit reduces to the mean field value $\langle n_\uparrow n_\downarrow \rangle = \langle n_\uparrow \rangle \langle n_\downarrow \rangle = 0.25$ at half filling. The double occupancy reduces smoothly as U increases with no signs of a first-order transition. The curves at constant chemical potential show an inflection point (inset of Fig. 6.3), however this is due to the changing density and not an indication of the widom line – The points definining the widom line are the points at which the second order derivative of the double occupancy cross zero, i.e. the inflection point. We find that, for half filling

the double occupancy is almost linear, and starts to flatten out at large U, however, we are unable to obtain data for $U \gtrsim 8.5$ as no density curves cross $n = 0.5$. We note a good agreement for the half filling curve with Refs. [36, 83] up to $U \approx 8.5$. The double occupancy relates to the local magnetic moment $m_l \propto \sqrt{n - 2D}$ (see chapter 4 of [114]). From this relationship it's clear that as U is increased, local magnetic moments form. At finite temperature we do not expect the double occupancy to reduce to zero due to thermal fluctuations, and hence a finite probability that doubly occupied sites will occur for any finite U.

Figure 6.4 (left) shows the temperature dependence of the double occupancy at increasing values of U – we are unable to perform the Páde approximant at larger U values for $\beta = 4.0$, so they are not shown. Moreover, we have limited resolution as we must perform multiple simulations at different chemical potential to obtain a reasonable estimation for half filling – We find a minimum in the temperature dependence of the double occupancy at $\beta \approx 2.0$ for large values of U, which is also reported in [36], whereas an LDFA study finds this to occur at a higher temperature of $\beta \approx 1.0$. The temperature dependence of the double occupancy is related to the entropy of the system via the Maxwell relation,

$$\frac{\partial S}{\partial U}\Big|_T = -\frac{\partial D}{\partial T}\Big|_U, \tag{6.1}$$

which relates the negative gradient of D with respect to temperature, as an increase in entropy as a function of U. Intuitively we would expect the entropy of the system to decrease as the system cools, however this relationship shows the entropy increases under cooling for $\beta \gtrsim 2.0$. Alternatively we may think of this as an increase in localisation as the system is heated, or cooling under an adiabatic increase in U. This behaviour is analogous to the Pomeranchuk effect found in Helium-3

– The solid phase of Helium 3 has a higher entropy than the liquid phase due to localised disordered spins [115] – and has been found in the Hubbard model on the square lattice [116–120].

The double occupancy gives us access to the potential energy of the system which

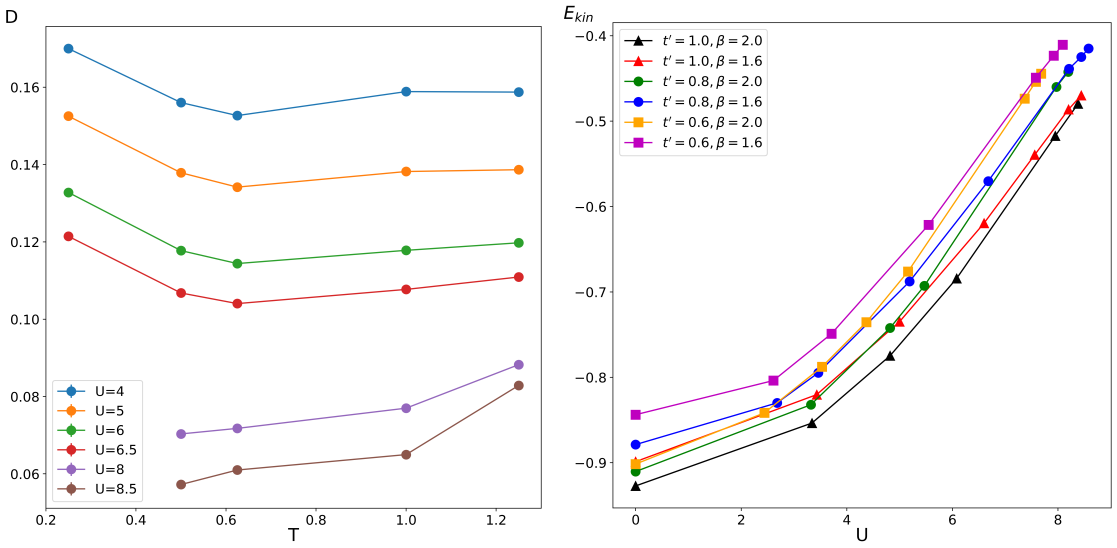


Figure 6.4: Left: Double occupancy as a function of temperature. A minimum in D is found at $\beta \approx 2.0$. The increase in D as temperature is reduced past $\beta \approx 2.0$ indicates an increase in entropy. Right: Kinetic energy for temperatures $\beta = 2.0, 1.6$ and $t' = 1.0, 0.8, 0.6$ showing a crossover in the derivative with respect to temperature at large U, which decreases with t'.

should initially increase due to increasing interaction strength, and then decrease upon approach, and into the insulating phase. The kinetic energy is a related observable, as the interplay between the competition of potential and kinetic energy is an indication of the physics occurring. The kinetic energy is negative – hopping lowers the energy of the system – and should decrease in magnitude as interaction increases due to the suppression of doubly occupied sites. Fig. 6.5 shows exactly this behaviour, for both potential and kinetic energy, without any signatures of a discon-

tinuity, suggesting a smooth crossover. However, we cannot rule out the possibility of a discontinuity at half filling due to insufficient resolution. Note that the half filling curves for potential and kinetic energy have been interpolated to follow the trend of the other curves. Figure 6.4 (right) shows the kinetic energy as a function

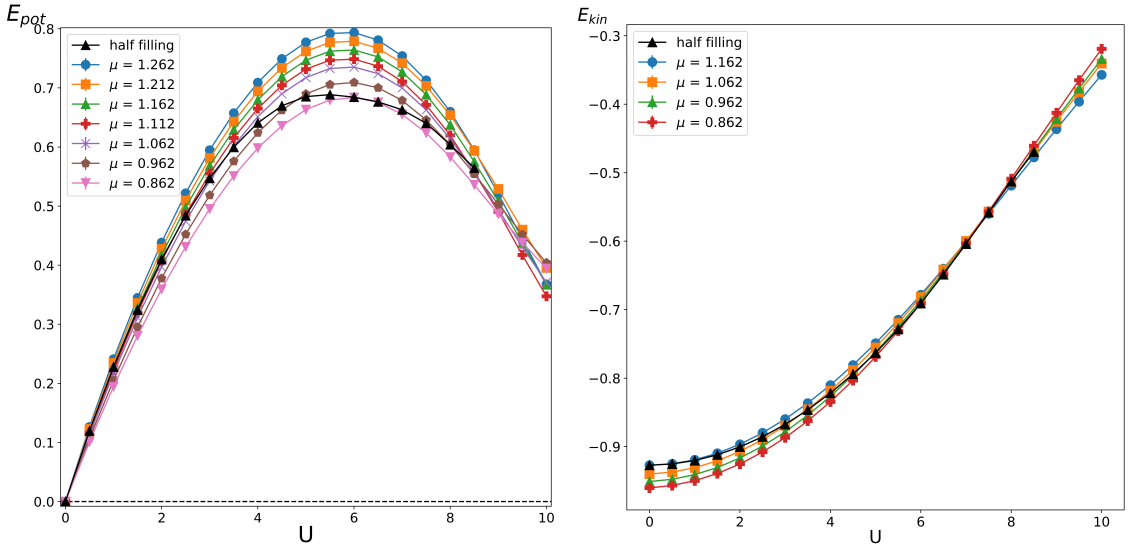


Figure 6.5: Left: Potential energy showing expected behaviour for metallic to insulating crossover. Right: Kinetic energy showing the same behaviour

of U for $\beta = 1.6$ and $\beta = 2.0$ for $t' = 1.0, 0.8, 0.6$. We find that $\partial E_{kin}/\partial T > 0$, as expected in a metal, until $U \approx 8.5$ at $t' = 1.0$. Past this point the derivative with respect to temperature is negative as one would expect in the insulating state. This occurs at slightly lower U for $t' < 1.0$.

6.1.3 Charge-Charge and Compressibility

The observables described above have provided evidence for a smooth crossover from metallic to insulating state, and some indication of the value of U when the crossover occurs, to which there is some arbitrariness due to the nature of crossovers. To improve upon this we follow a procedure carried out in Ref. [21], which makes use of the temperature dependence of the compressibility κ, potential energy, and kinetic energy, to define the crossover for the Hubbard model on the square lattice.

At low U the system is in a metallic state, and the the compressibility of the system is finite, since the system can accommodate extra particles at a minimal increase in energy. As the temperature decreases, the number of occupied states at the Fermi surface increases, causing compressibility to increase, such that $\partial\kappa/\partial T$ is negative. This effect is less pronounced at higher temperatures due to smearing of the Fermi surface, but still has a non-negligible effect [21]. At large U the system moves toward an insulating state which is characterised by a charge gap and density fluctuations that are temperature dependent. Increasing the number of particles comes at a costly energy penalty, and the compressibility of the system reduces. The temperature dependent density fluctuations cause $\partial\kappa/\partial T$ to become positive i.e. compressibility is larger for higher temperatures. The crossover location is then defined by $\partial\kappa/\partial T = 0$. Figure 6.6 shows the compressibility at different temperatures for curves with similar non-interacting density. The condition $\partial\kappa/\partial T = 0$ is satisfied at $U \approx 6.5$. We find the crossover at half filling to occur slightly later at $U \approx 6.9$ as shown in Fig. 6.7 – on the square lattice at $\beta = 2.0$ this occurs at $U \approx 3.2$ [21], showing the effect of geometric frustration stabilising the metalic state to higher U. Although this condition is considered at constant density in Ref. [21], we find that compressibility curves at a constant temperature for varying chemical potentials are extremely close, as shown

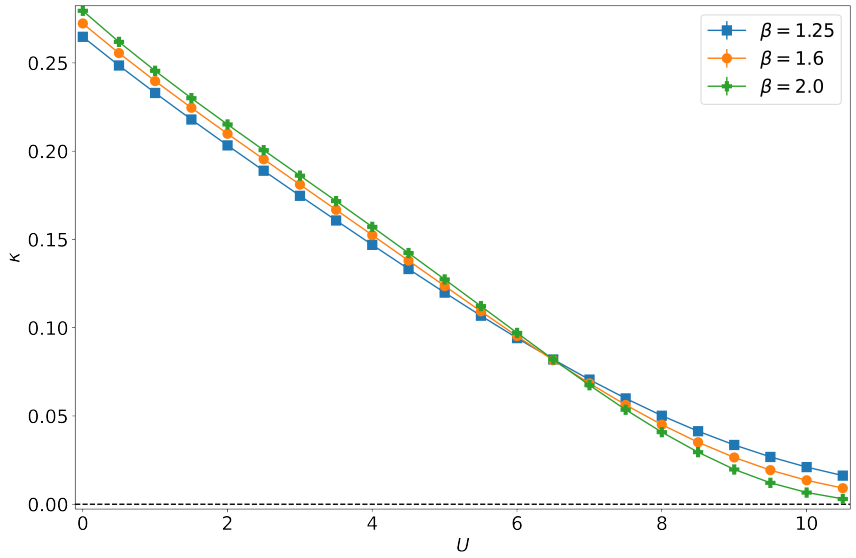


Figure 6.6: Curves of compressibility κ for different temperatures showing the condition $\partial\kappa/\partial T = 0$ is met at $U \approx 6.7$ defining the crossover.

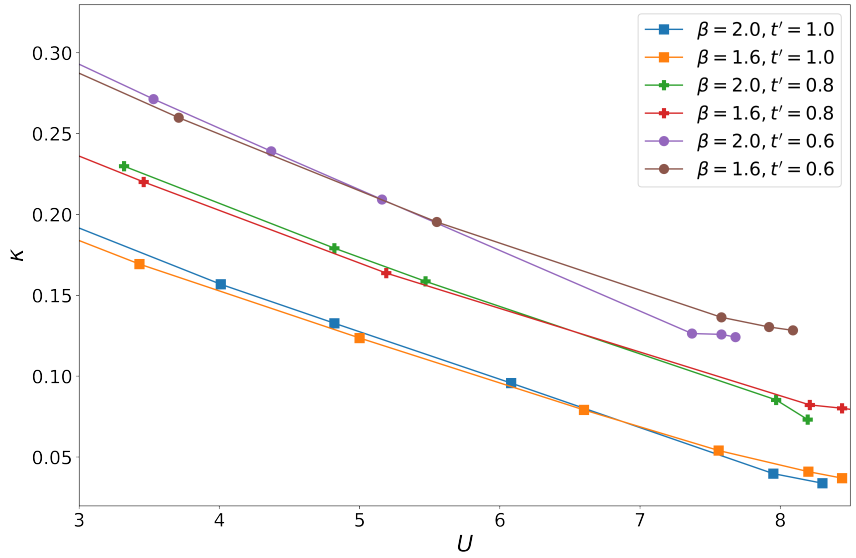


Figure 6.7: Compressibility curves at half filing for $\beta = 2.0$ and $\beta = 1.6$, showing the condition $\partial\kappa/\partial T = 0$ occuring for lower U as t' increases. Note that the curves for $t' = 0.8$, and $t' = 0.6$ have been shifted by $+0.05$, and $+0.1$ respectively.

in Fig. 6.8, such that the criterion to define the crossover should still hold away from half filling. The interaction strength corresponding to the maximum of the density

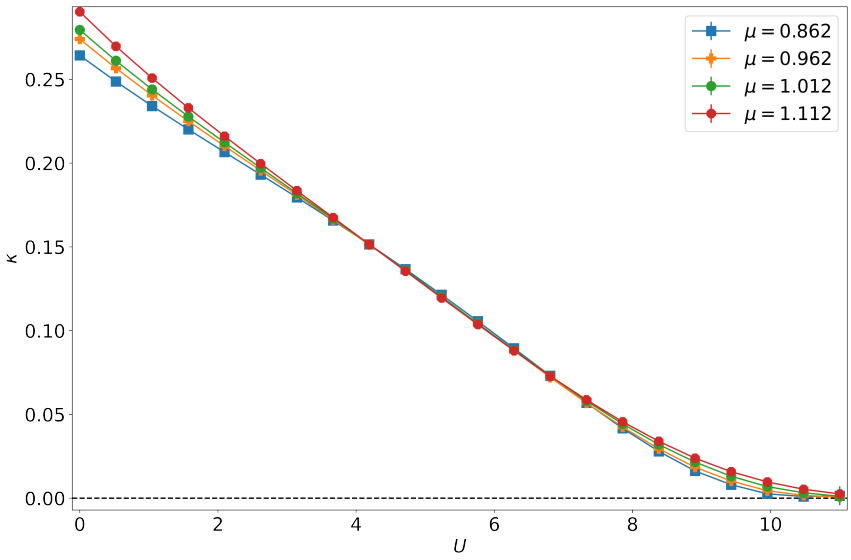


Figure 6.8: Compressibility curves for different chemical potentials at $\beta = 2.0$. The curves overlay each other at intermediate U values before splitting at large U.

curves corresponds closely to the crossover interaction value, with the crossover occurring at slightly larger U for lower chemical potentials. Past the crossover point $\partial\kappa/\partial T > 0$ indicates insulating behaviour, but $\partial D/\partial T < 0$, and $\partial E_{kin}/\partial T > 0$ as found in a metal [103], indicating the crossover is from a metallic to a non-Fermi liquid (nFL) regime. This behaviour is short lived, as by $U \approx 7.5$, $\partial D/\partial T > 0$ as expected for an insulator, and at $U \approx 8.5$, $\partial E_{kin}/\partial T < 0$, indicating insulator like behaviour from all observables. This value corresponds closely to the U value at which the density curves cross the half filling point and begin to converge. Our results indicate an intermediate regime between the metallic and insulating states, that is often referred to as the pseudogap, and has been found for the Hubbard model on a triangular lattice previously [96].

The compressibility may be factored into local and non-local contributions $\kappa = \beta(C_{loc} + C_{nl})$, with $C_{nl} = \frac{\beta}{N}\sum_{i\neq j} C(i-j)$, to distinguish the effect that non-local correlations have on compressibility. Local correlations are related to double occupancy via $C_{loc} = 2D$, and the decrease in compressibility with U is largely driven by the decrease in double occupancy. However, as shown in Fig. 6.9 we find that nonlocal correlations are of the same order of magnitude as local correlations, which has been observed for the Hubbard model on the square lattice [21, 121, 122]. The

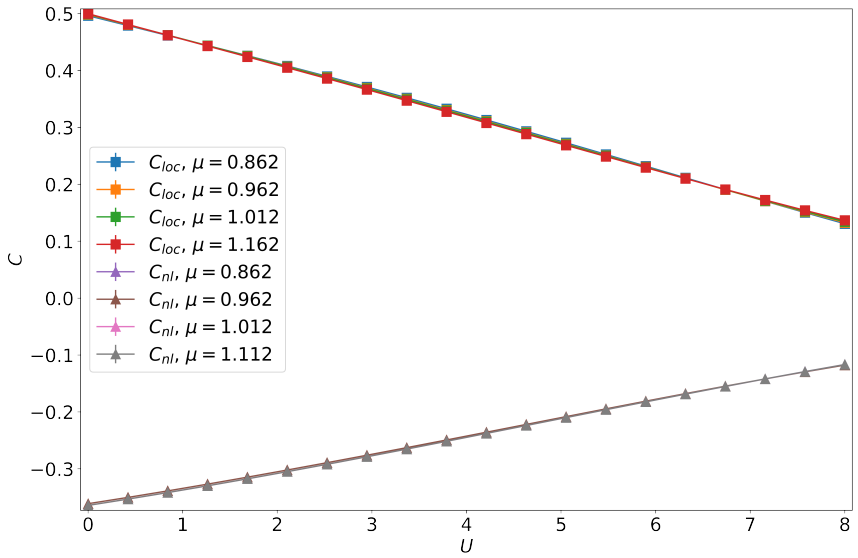


Figure 6.9: Plot comparing magnitude of local C_{loc}, and nonlocal C_{nl} charge correlations, highlighting the similarity in magnitude but difference in sign.

lines for different chemical potentials overlay each other so that the half filling line follows the same trend. In the non-interacting limit the non-local correlations are due to Fermion statistics i.e. the Pauli principle causes electrons with the same spin to antibunch, giving rise to anti-correlations which suppress charge fluctuations. This effect is known as the correlation hole [121]. As U increases, nonlocal correlations in the same sublattice rapidly increase, and are then suppressed as U increases further,

whilst nonlocal correlations on different sublattices are suppressed for all $U > 0$. This is shown in Fig. 6.10, where on the triangular lattice, relative to $\boldsymbol{r} = (0, 0)$, the closest sites on the same sublattice are $\boldsymbol{r} = (-1, 1), (1, -1)$, whilst $\boldsymbol{r} = \{(1, 0), (0, 1), (1, 1)\}$ and its negation, are on different sublattices – the sublattices have been defined here with respect to the 120° ordering [106], and are shown in Fig. 6.12 – A further difference between nonlocal correlations in the same, and different sublattices occurs for small U. Anticorrelations are slightly enhanced at higher density for the same sublattice, whilst they are slightly suppressed for different sublattices. The non local

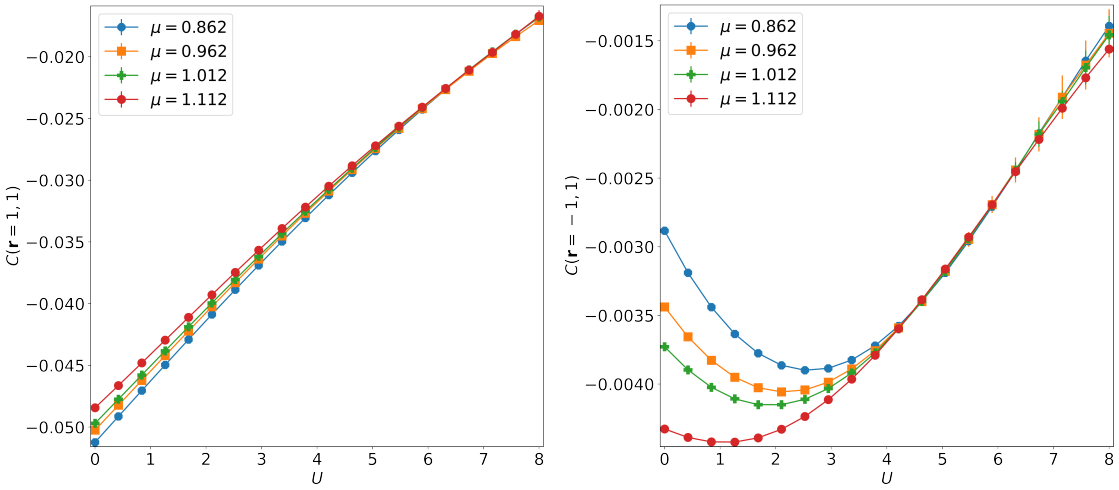


Figure 6.10: Left: Charge correlation on the same sublattice as $\boldsymbol{r} = (0, 0)$ as function of U for different chemical potentials. $\boldsymbol{r} = (1, -1)$ is identical to $\boldsymbol{r} = (-1, 1)$ and not plotted. Right: Charge correlation on different sublattices. $\boldsymbol{r} = (1, 0), (0, 1)(0, -1), (-1, 0)$ are identical to $\boldsymbol{r} = (1, 1)$ and not plotted

correlations are therefore responsible for the condition $\partial\kappa/\partial T > 0$ occuring prior to the potential energy showing metallic behaviour, thus driving the crossover into the nFL regime as found on the square lattice.

We note that for lower temperatures i.e. $\beta > 0.5$ Ref. [36] finds an increase in double occupancy up to values of $U = 12$ such that the above procedure would find

$\partial D/\partial T < 0$ for U up to at least $U = 12$, which aligns with the increase in entropy as the temperature decreases.

Table 6.1 shows the approximate values of U at which the derivatives with respect to temperature change sign for different values of t'.

t'	$\partial\kappa/\partial T$	$\partial D/\partial T$	$\partial E_{kin}/\partial T$
1.0	6.9	7.5	8.5
0.8	6.5	7.0	7.9
0.6	5.25	6.5	7.4

Table 6.1: Table showing values of U at which the crossover conditions occur. For U greater than the value at which $\partial\kappa/\partial T = 0$ occurs, the crossover from metallic to nFL state occurs, until $\partial E_{kin}/\partial T = 0$, when the system becomes insulating.

6.1.4 Spin structure factor

Finally, we present results for the spin structure factor. We firstly note that for $t' = 1.0$ we find similar behaviour in the spin structure factor at all chemical potentials calculated, which range in density as $0.48 < n < 0.52$, although only at certain U values. Ref. [123] finds the 120° QAFM order robust upon hole doping up to $\delta_h = 0.3$, whilst Ref. [85] finds the 120° QAFM order phase yielding to ferromagnetic-like ordering for electron doping of $\delta_e = 0.05$ i.e. $n = 0.55$. So this behaviour is expected, and differs from the square lattice in which small doping drastically affects the magnetic order. At $t' = 1.0$, and $\beta = 2.0$, we find short range 120° QAFM ordering occuring, via a smooth, broad peak at the K-points as shown in Fig. 6.11. Also shown is the transition of the peak from the M'-point, which indicates Néel QAFM ordering, to the K-point as t' increases [109] in the range $0.7 < t' < 1.0$.

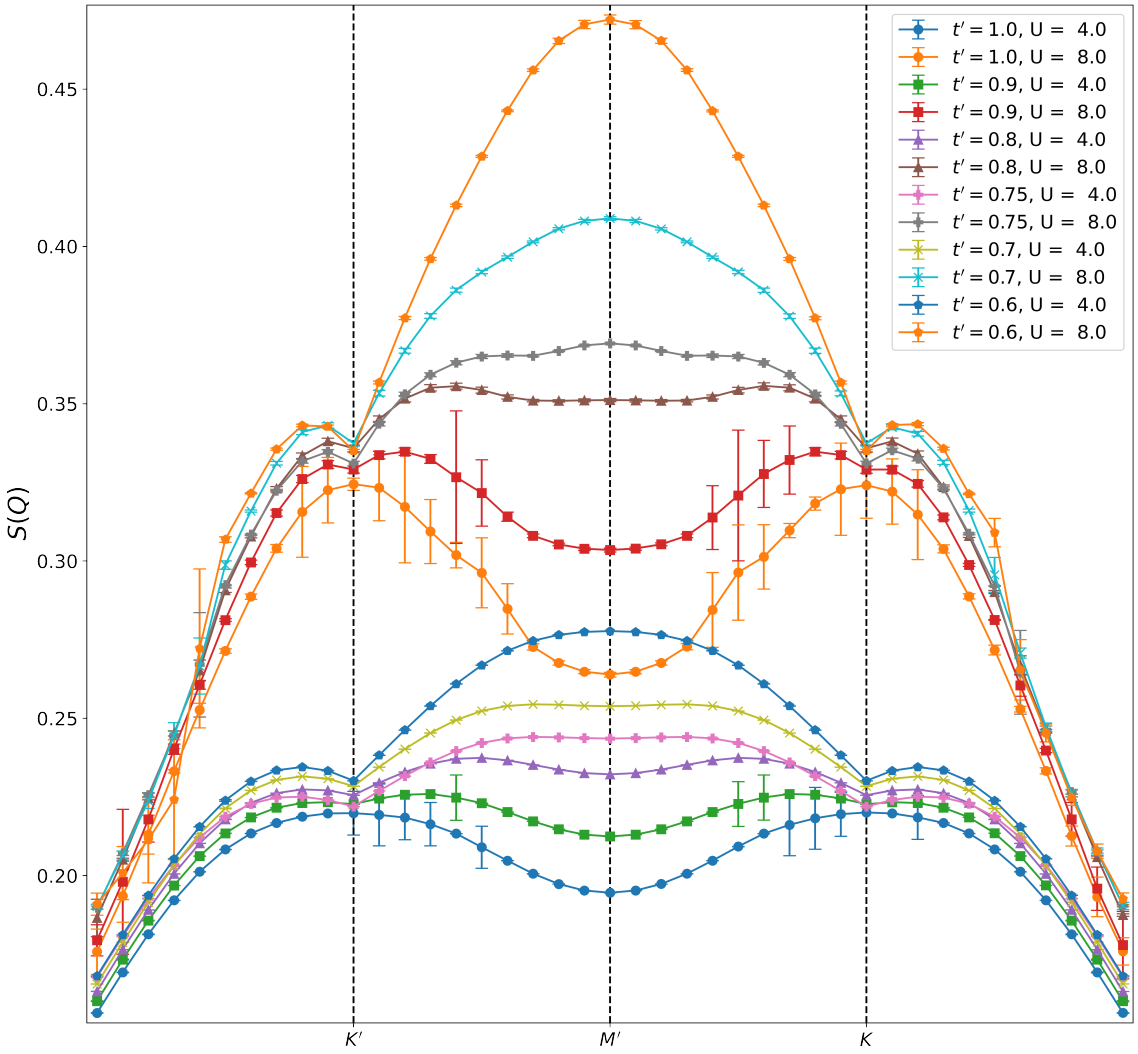


Figure 6.11: The evolution of the magnetic structure factor peak moving from M' to K as a t' increases at both small, and large interaction strength.

For $0.6 < t' < 0.7$ the peak is still situated at M', but the magnitude decreases as t' increases. In the range $0.7 < t' < 0.75$ the peak at M' continues to decrease whilst incommensurate peaks, half way between M' and K, gain in magnitude. Past this point we find that the peak both shifts toward K, and continues to decrease in magnitude, which is also found in Ref. [109]. Furthermore, it is not that the peak at the K-point 'develops', it is a side effect of the peak at the M'-point drastically decreasing, and the shoulder close to the K-point also decreasing, leaving a broad peak centered on K.

Since we are above the magnetic ordering temperature [90] we expect to see smooth, broad peaks, however, they are still indicative of the underlying physics. Moreover, Ref. [36] finds that 120° ordering is favoured at higher temperature as a consequence of the Pomeranchuk effect discussed earlier.

Note that the increased size of the error bars as $t' \to 1$ exemplifies the difficulties with convergence as the spatial extent of the Green's function increases.

In Fig. 6.12 we show the evolution of the real space spin-spin correlator as both U increases, and t' decreases. For the isotropic case at small U we find nearest neighbour correlations – $Z = 6$ for the triangular lattice indicated by the sites C and B. The diagonals which are on the A sublattice in the diagram are further away from the origin in terms of hopping – in a background of weakly correlated sites. As U increases the correlation length increases and we find 120° QAFM ordering with a correlation length $\xi \approx 1.83$ at $U = 8.0$, which is similar to that found in [106]. Here we have calculated the correlation length by fitting to an exponential function, i.e. the spin-spin correlator shows exponential decay indicative of the lack of long-range order. As t' decreases we find that the correlation length similarly increases upon increasing U, and the evolution toward the square bi-lattice is evident by the off-diagonals amplitude becoming similar to the diagonals i.e. the formation of short

range Néel ordering.

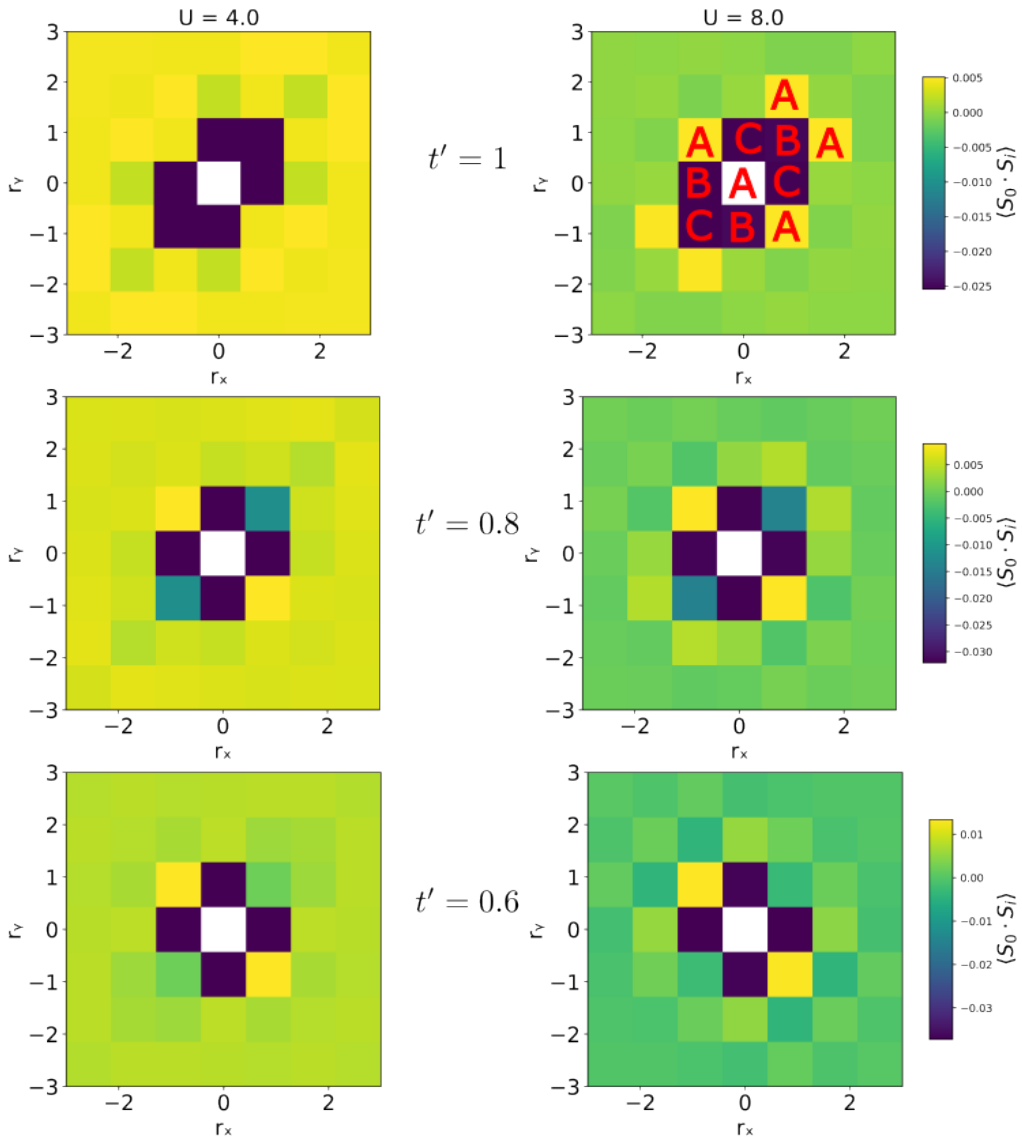


Figure 6.12: Spin-spin correlator in real space at both low and high U values. The triangular sublattices are labelled on the top right heatmap. t' decreases when moving down a row, and we see the evolution from a three-sublattice state toward a two-sublattice state.

In Fig. 6.13 we show the structure factor for small U at half filling – We are unable to converge the series for large U at these temperatures – for $\beta = 4, 10$. At these temperatures the peak is no longer commensurate with the K-point, and the magnitude at M' is further supressed when compared to $\beta = 2$. This is counter-intuitive as we would expect the peak at K to become more pronounced, and less broad. However, Ref. [9] finds such behaviour at small U, which becomes distinct peaks at the K point by $U = 10$. The low U behaviour can therefore be attributed to the lowering of localization and increased entropy upon cooling, as discussed earlier.

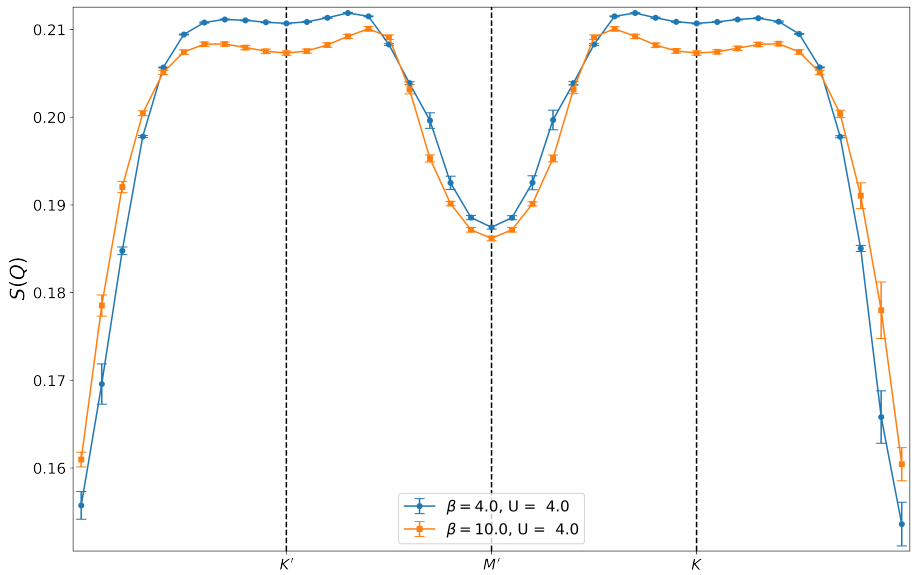


Figure 6.13: The spin structure factor for $\beta = 4, 10$ showing a decrease in the magnitude at the K-point, when compared with $\beta = 2$.

The high symmetry path taken in Fig. 6.13 does not show the whole picture of the structure factor, we therefore present heatmaps of the structure factor for $U = 4$, at $\beta = 4, 10$ – note that we do not show the heatmaps for $\beta = 2$ as they match the $\beta = 4$ closely, as the smoothness of the function makes them discernable from

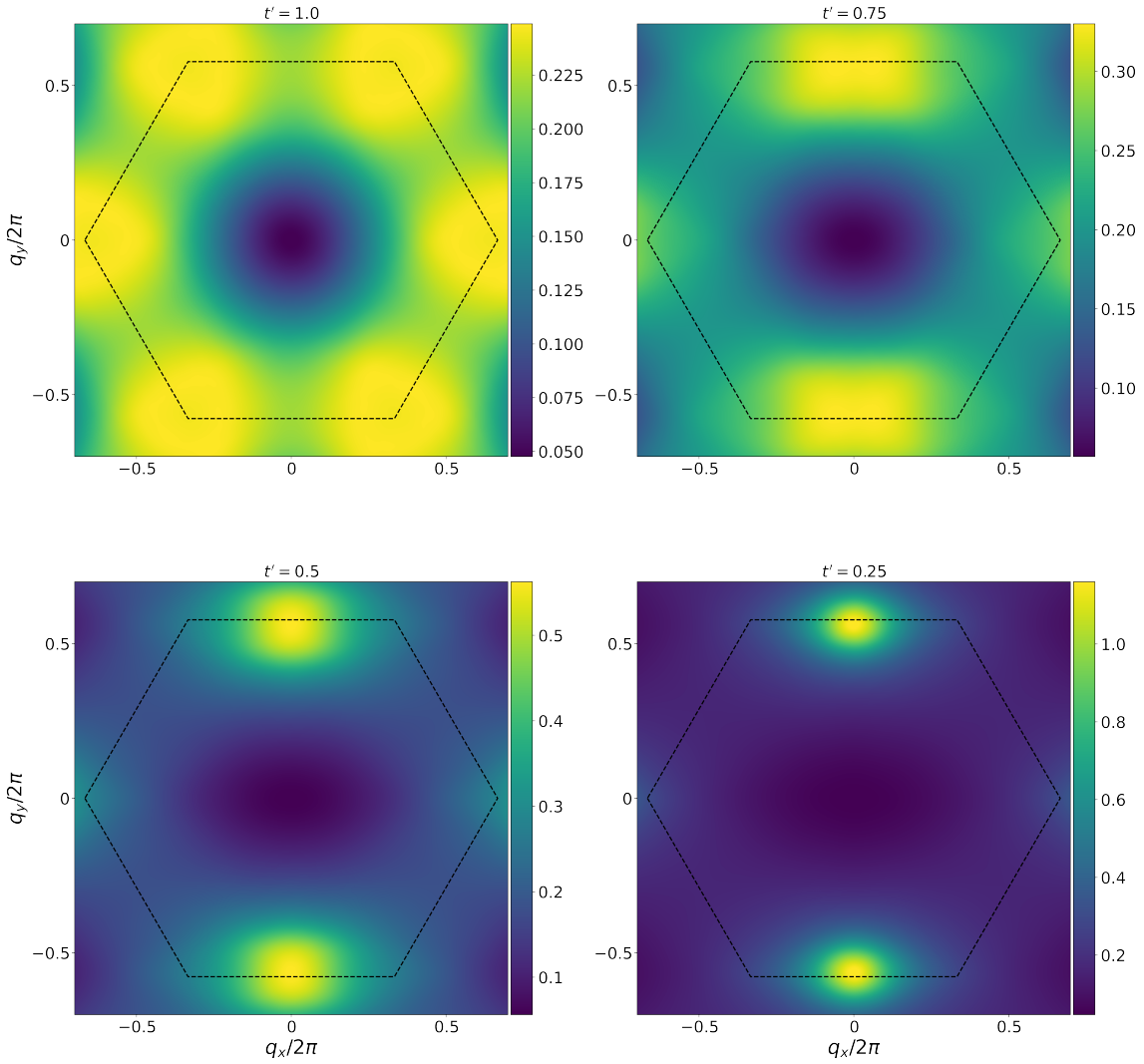


Figure 6.14: The spin structure factor for $\beta = 4$, $U = 4$, across the full Brillouin zone for $t' = 1.0, 0.75, 0.5, 0.25$.

one another – for orders $N = 5$, which we find to be sufficiently converged at low U. Fig. 6.14, and Fig. 6.15 show the structure factor at $t' = 1.0, 0.75, 0.5, 0.25$ for $\beta = 4.0$, and $\beta = 10$ respectively. At the isotropic limit we find the formation of triangular like structures centered on the K-point, that become more pronounced as β increases [9]. The structures around the K-points are indicative of $2\boldsymbol{k}_F$ scattering with $\boldsymbol{k}_F$ the Fermi momentum in the non-interacting limit. However, this is thought to play a less crucial role in driving order due to the effects of geometric frustration [106], indicated by its disappearance at larger U values [9]. At $t' = 0.75$ the prominence of the peak shifted away from the M'-point becomes more apparent as temperature decreases, and the development of the shoulder close to the K-points stands out. At $\beta = 10$ we find that the peak at the M'-point is incommensurate for $t' = 0.5$, whereas at $\beta = 2$ we found this peak to be robust until $t' \approx 0.75$, much like the incommensurate peaks around K at low U, Ref. [9] finds the peak to become commensurate with M' for larger U, suggesting this is similarly due to the Pomeranchuk effect.

6.1.5 Summary

In summary, we have calculated multiple observables for the anisotropic triangular lattice Hubbard model at $\beta = 2$. Using a combination of the compressibility, and energetics of the system, we have identified a crossover from metallic to nFL behaviour, indicated by compressibility exhibiting insulating behaviour, whilst the energetics of the system exhibit metallic behaviour. The crossover occurs at $U \approx 6.9$ at half filling in the isotropic limit. As U increases the nFL yields to an insulating state at $U \approx 8.5$, indicated by a change in sign of $\partial E_{kin}/\partial T$. The magnetic structure factor

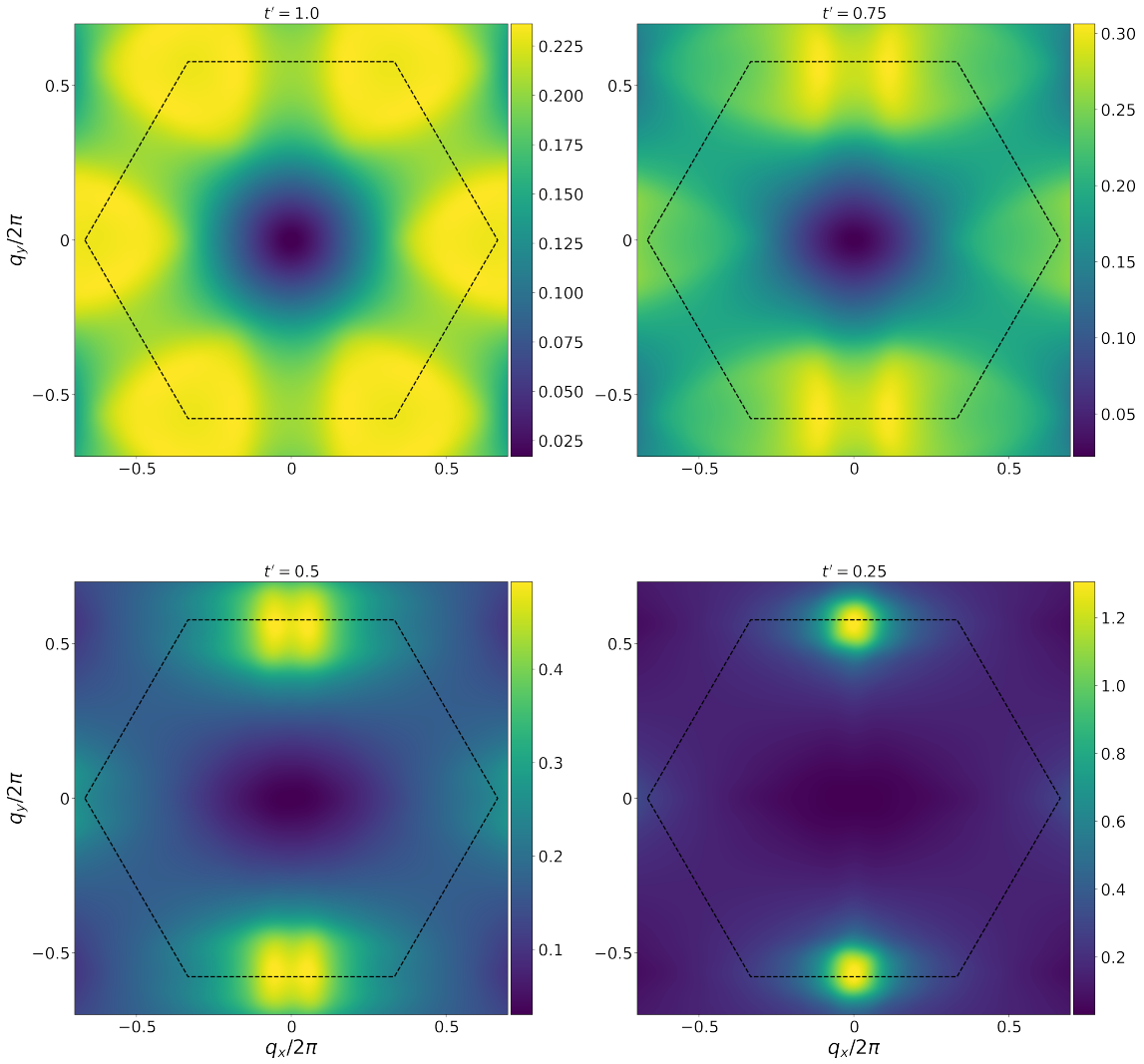


Figure 6.15: The spin structure factor for $\beta = 10$, $U = 4$, across the full Brillouin zone for $t' = 1.0, 0.75, 0.5, 0.25$.

shows broad peaks centred at the K-points indicative of 120° QAFM behaviour. As temperature is decreased we see signs of the Pomeranchuk effect in the magnetic structure factor, causing the formation of triangular like structures in the spin structure factor, centred around the K-points.

Away from $t' = 1.0$ we see similar crossover behaviour, and find that the critical U values for the crossover regimes reduce with the reduction of t', as indicated in table 6.1. As t' decreases, the peak of the structure factor moves toward the M'-point showing a tendency toward Néel QAFM. By $t' = 0.7$, at $\beta = 2$ the peak is commensurate with M' and grows in magnitude for smaller t' values. We find that at $\beta = 10$ the peak around M' becomes commensurate at the lower value of $t' \approx 0.5$ for small U. For lower temperatures we find convergence issues and cannot perform the same procedure to determine the crossover between metallic, nFL, and insulating behaviours due to the presence of non-physical singularities in the Páde approximants.

Chapter 7

Conclusion and Outlook

7.1 Conclusion

In this thesis, we first described the implementation of a "plug-and-play" type diagrammatic Monte Carlo (DiagMC) code base, which we hope to release for open use in the future. We implement "classical" DiagMC in which individual diagram topologies are sampled stochastically via a Markov chain Monte Carlo algorithm, along with the extension to the shifted action approach. The shifted action approach allows for re-ordering of the diagrams to improve convergence of the series by including a shift in the original action, which could take the form of an arbitrary constant, be provided by previous results, or an ansatz based on physical reasoning. A large amount of effort went into making updates as theory-independent as possible, with the addition of abstract interfaces for all classes, aiding extension to new theories. We implement the option to include the symmetrized basis function in the Monte Carlo weight to reduce variance of sampling, where the symmetrized

basis functions are implemented for square, cubic, and triangular lattices. Finally we showed some benchmark results for the self-energy of the square Hubbard model, as a function of frequency for nodal and anti-nodal points, and via cuts through the high symmetry path for the lowest Matsubara frequency for a range of temperatures. We also presented data for the momentum distribution function which is obtained via Dyson's equation.

Creating generic interfaces for all areas of the code base was a long task, and at times arduous. In terms of Monte Carlo updates, the standard DiagMC updates are complex when applied to a single theory. Generalising the updates compounded that complexity, and in turn, made debugging issues difficult. Moreover, generalisations of classes not central to the algorithm, such as the implementation of the hdf5 file format, took a long time to implement, pushing back investigations of physical systems. Whilst we have not obtained any novel results using the DiagMC implementation, we have proved its viability, and more importantly, created a robust code base that is both easily extendable into the future, and implements multiple tests for easily debugging newly introduced code. This should alleviate the need for multiple projects when calculating multiple observables, or similar observables for different models, as is often the case in computational physics.

Motivated by disagreements between existing works on the topic, we then turned to the study of the triangular lattice Hubbard model, allowing the hopping t' along one of the triangular directions to vary between $0 \leq t' \leq t$. As t' is increased from 0, geometric frustration plays an increasing role in determining the physics of the system, as it inhibits the formation of quasi-long-range magnetic ordering. Experiments on the organic salt family κ-(BEDT-TTF)X [66–69], in which certain compounds are found to have triangular lattice structures, find interesting phases

occuring such as superconductivity, and Mott insulating states. Furthermore, some materials are found to show no magnetic ordering down to very low temperatures, which are candidates for quantum spin-liquids (QSL) [66, 70]. We applied the connected determinant algorithm for moderate temperatures of $\beta \approx 2$, along with Páde approximant techniques to show the existence of a metal-insulator crossover, with an intermediate regime exhibiting non-Fermi liquid (nFL) behavour. This was achieved by calculating the density (n), compressibility (κ), double occupancy (D), and kinetic energy of the system. Due to the lack of particle-hole symmetry in the triangular hubbard model, the cDet algorithm has no way to lock the density at half filling, therefore calculating density was a requirement to know at which values of U our data corresponded to half filling.

In the isotropic limit, $t' = t$, at half filling and $\beta = 2.0$, the crossover from metallic to nFL occurs at $U \approx 6.9$, where the condition $\partial\kappa/\partial T = 0$ is met. At this interaction strength, the energetics of the system show metallic behaviour, hence the classification of a nFL [21, 96]. By $U \approx 8.5$ the conditions $\partial D/\partial T = 0$, and $\partial E_{kin}/\partial T = 0$ are met, and the system becomes insulating. Where the double occupancy is related the potential energy by $E_{pot} = UD$. As t' is reduced, the value of U at which the crossover from metallic to nFL, and nFL to insulating state, decreases. The crossover occuring for lower values of interaction is due to the decrease in geometric frustration, which acts to stabilise the metallic region via the destruction of quasi-long-range magnetic ordering. At $t' = 0$ the metallic state is unstable toward the formation of quasi-antiferromagnetic ordering at infinitesimal U.

The temperature dependence of the double occupancy shows a minimum occuring at $\beta \approx 2$ for large U values, indicating an increase in entropy as the system is cooled below this point, via the relation $\partial S/\partial U = -\partial D/\partial T$, where S is the entropy. This is analogous to the Pomeranchuk effect in Helium-3, and has been found in both the

triangular, and square lattice Hubbard model [36, 116–120].
Information about the magnetic state of the system was obtained via calculation of the spin structure factor, which is the Fourier transform of the spin-spin correlator. We found that the (quasi)Néel state is robust toward anisotropy away from the square lattice and exists for $0 \leq t' < 0.75$, although the magnitude of the structure factor decreases considerably as t' increases. At $t' \approx 0.75$ the Néel order gives way to an incommensurate peak around the M' point, which Ref. [124] describes as a QSL. However, with our current data we have no way to prove the existence of a QSL, and we choose to label this as incommensurate magnetic ordering. For $t' \gtrsim 0.75$ we find that the peak in the spin structure factor moves toward the K-points, until at $t' = 1.0$, the centre of the peak coalesces with the K-point indicating 120° (quasi)magnetic ordering. As temperature decreases the reduced localisation from the Pomeranchuk effect is seen in the spin structure factor, where for small to intermediate U, the peak at the K-points decreases and 'shells' at $\boldsymbol{q} \approx 2\boldsymbol{k}_F$ form around the K-points.

As discussed in the main text, we found issues with convergence of the series when reducing the temperature such that $\beta > 2$. This was due to the extended spatial extent of the Green's functions on the triangular lattice, on account of the increased connectivity between lattice sites i.e. the extra term in the dispersion relation. This had the effect of pushing the vertices further away from the origin during simulation, as diagrams with vertices well separated from each other had greater weight when compared to that of square lattice – the effect of lowering temperature increases the tails of the Green's functions, exacerbating this effect. A reduction in t' exhibited better convergence properties, and at $t' = 0$ we were able to obtain similar results with a factor of 10 less Monte Carlo samples. The lack of sufficient series expan-

sion coefficients, with small enough errorbars lead to the breakdown of the Páde approximant resummation method. Moreover, due to the absence of particle-hole symmetry, the lack of density control in the standard cDet algorithm required many series expansions to be calculated at different chemical potentials to obtain sufficient resolution to produce results for half filling. Such issues indicate that the cDet algorithm is not ideally suited for computing observables on the triangular lattice. Methods such as Dynamical Mean Field Theory (DMFT), its cluster extensions, and Density Matrix Renormalisation Group (DMRG) may be more well suited for this case, but also come with draw backs. For instance DMFT does not included non-local correlations, unless a cluster extension is employed. Cluster methods, which include non-local correlations, have limited momentum resolution and therefore do not correctly find incommensurate magnetic ordering [86]. Whilst DMRG includes some non-local correlations – limited by cylinder size – it exhibits strong finite size-effects in 2D [92, 93]. However, diagrammatic Monte Carlo has arbitrary momentum precision, and by construction includes all correlations via the summation of all diagrams contributing to an observable.

7.2 Outlook

Whilst we have worked towards a good baseline for a generic DiagMC application, there are a few implementations we have that are not mentioned here as they have not been formally tested, as well as many sophisticated diagrammatic techniques that we could still implement. Firstly we have fully implemented the Monte Carlo algorithm for the case of two-particle(four-point) diagrams, however there was not time to fully test this implementation. Furthermore, we have only partially tested the

shifted-action implementation (the reason for not presenting any benchmark data). Dyson's equation is fully implemented and tested, however time constraints stopped the calculation of higher order diagrams, and as a consequence, one-particle thermodynamic observables. Moreover the Monte Carlo algorithm for dressed vertices has been worked out, and implemented, alongside an implementation of a vertex dressed with the pair propagator. It would be great to benchmark these implementations and gather some data on interesting physics. We would also like to implement the cDet algorithm into our code base in a generic fashion, as it boasts polynomial complexity and can reach higher orders than classical DiagMC.

We may use the four-point diagrammatic implementation to confirm our density calculations obtained via the cDet algorithm on the triangular lattice. We may also investigate the structure of $\mathrm{Im}\Sigma$ against Matsubara frequency to determine the crossover regime critical U more accurately [18]. We are able to sample with anomalous propagators opening up studies of superconductivity, which is of great interest in the 2d Hubbard model. Moreover, the versatility of the Hubbard model allows us to emulate continuous systems by sampling at low density, with arbitrary momentum cut-offs.

The work carried out on the anisotropic triangular Hubbard model shows the viability of diagMC techniques to more than just calculation of self energies – as far as we are aware there is only a single diagMC study of the ansisotropic triangular Hubbard model [36], in which DiagMC was auxiliary to the investigation. The obvious downside of our current implementation is the lack of controlled density, which requires many calculations of the same observable at different chemical potentials to obtain enough data to construct curves for half filling. The application of "nilpotent polynomials", along with the inclusion of non perturbative information

to the cDet algorithm [111] results in the renormalisation of observables, which can be used to calculate at exactly half filling. An implementation of this applied to the anisotropic triangular lattice would reduce the number of calculations required, and remove the need for post processing procedures to find the half filling values of observables. Notwithstanding, our current implementation will provide a valuable benchmark for verifying the accuracy of the more advanced nilpotent polynomial renormalised technique, which computes a different series expansion, and will have different convergence properties.

Bibliography

1. Gonze, X. *et al.* The Abinit project: Impact, environment and recent developments. *Comput. Phys. Commun.* **248,** 107042. https://doi.org/10.1016/j.cpc.2019.107042 (2020).

2. Hubbard, J. Electron Correlations in Narrow Energy Bands. *Proceedings of the Royal Society of London. Series A, Mathematical and Physical Sciences* **276,** 238–257. ISSN: 00804630. http://www.jstor.org/stable/2414761 (2024) (1963).

3. Jaksch, D., Bruder, C., Cirac, J. I., Gardiner, C. W. & Zoller, P. Cold Bosonic Atoms in Optical Lattices. *Phys. Rev. Lett.* **81,** 3108–3111. https://link.aps.org/doi/10.1103/PhysRevLett.81.3108 (15 Oct. 1998).

4. Georges, A., Kotliar, G., Krauth, W. & Rozenberg, M. J. Dynamical mean-field theory of strongly correlated fermion systems and the limit of infinite dimensions. *Rev. Mod. Phys.* **68,** 13–125. https://link.aps.org/doi/10.1103/RevModPhys.68.13 (1 Jan. 1996).

5. Mai, P., Balduzzi, G., Johnston, S. & Maier, T. A. Pairing correlations in the cuprates: A numerical study of the three-band Hubbard model. *Phys. Rev. B*

103, 144514. https://link.aps.org/doi/10.1103/PhysRevB.103.144514 (14 Apr. 2021).

6. Fetter, A. L. & Walecka, J. D. *Quantum Theory of Many-Particle Systems* (McGraw-Hill, Boston, 1971).

7. Mattuck, R. D. Guide to Feynman diagrams in the many-body problem. https://www.osti.gov/biblio/6059343 (Jan. 1976).

8. Li, S. & Gull, E. Magnetic and charge susceptibilities in the half-filled triangular lattice Hubbard model. *Phys. Rev. Res.* **2,** 013295. https://link.aps.org/doi/10.1103/PhysRevResearch.2.013295 (1 2020).

9. Yu, Y., Li, S., Iskakov, S. & Gull, E. Magnetic phases of the anisotropic triangular lattice Hubbard model, 1–13. arXiv: 2211.09234. http://arxiv.org/abs/2211.09234 (2022).

10. Mahan, G. D. *Many Particle Physics, Third Edition* (Plenum, New York, 2000).

11. Jishi, R. A. *Feynman Diagram Techniques in Condensed Matter Physics* (Cambridge University Press, 2013).

12. Coleman, P. *Introduction to Many-Body Physics* (Cambridge University Press, 2015).

13. Dyson, F. J. Divergence of perturbation theory. *Physical Review* **85,** 631 (1951).

14. Salpeter, E. E. & Bethe, H. A. A Relativistic Equation for Bound-State Problems. *Phys. Rev.* **84,** 1232–1242. https://link.aps.org/doi/10.1103/PhysRev.84.1232 (6 Dec. 1951).

15. Born, M. & Oppenheimer, R. Zur Quantentheorie der Molekeln. *Annalen der Physik* **389,** 457–484. https://onlinelibrary.wiley.com/doi/abs/10.1002/andp.19273892002 (1927).

16. Mermin, N. D. & Wagner, H. Absence of Ferromagnetism or Antiferromagnetism in One- or Two-Dimensional Isotropic Heisenberg Models. *Phys. Rev. Lett.* **17,** 1133–1136. https://link.aps.org/doi/10.1103/PhysRevLett.17.1133 (22 Nov. 1966).

17. Schäfer, T. *et al.* Tracking the footprints of spin fluctuations: A multi-method, multi-messenger study of the two-dimensional hubbard model. *arXiv* **11,** 11058. ISSN: 23318422. arXiv: 2006.10769. https://doi.org/10.1103/PhysRevX.11.011058 (2020).

18. Iv, F. Š. *et al.* Extended Crossover from a Fermi Liquid to a Quasiantiferromagnet in the Half-Filled 2D Hubbard Model. **017003,** 1–6 (2020).

19. Rohringer, G. & Toschi, A. Impact of nonlocal correlations over different energy scales: A dynamical vertex approximation study. *Phys. Rev. B* **94,** 125144. https://link.aps.org/doi/10.1103/PhysRevB.94.125144 (12 Sept. 2016).

20. Schäfer, T. *et al.* Fate of the false Mott-Hubbard transition in two dimensions. *Phys. Rev. B* **91,** 125109. https://link.aps.org/doi/10.1103/PhysRevB.91.125109 (12 Mar. 2015).

21. Kim, A. J., Simkovic, F. & Kozik, E. Spin and Charge Correlations across the Metal-to-Insulator Crossover in the Half-Filled 2D Hubbard Model. *Phys. Rev. Lett.* **124,** 117602. https://link.aps.org/doi/10.1103/PhysRevLett.124.117602 (11 Mar. 2020).

22. Brown, P. T. *et al.* Spin-imbalance in a 2D Fermi-Hubbard system. *Science* **357,** 1385–1388. eprint: https://www.science.org/doi/pdf/10.1126/science.aam7838. https://www.science.org/doi/abs/10.1126/science.aam7838 (2017).

23. Ohashi, T., Momoi, T., Tsunetsugu, H. & Kawakami, N. Finite Temperature Mott Transition in Hubbard Model on Anisotropic Triangular Lattice. *Phys. Rev. Lett.* **100,** 076402. https://link.aps.org/doi/10.1103/PhysRevLett.100.076402 (7 Feb. 2008).

24. Cohen, H. *Numerical Approximation Methods:* $\Pi \approx 355/113$ ISBN: 9781441998361. https://books.google.co.uk/books?id=tlzj0MIugwUC (Springer, 2011).

25. Boito, D., London, C. Y., Masjuan, P. & Rojas, C. Model-independent extrapolation of MUonE data with Padé and D-Log approximants. *Phys. Rev. D* **110,** 074012. https://link.aps.org/doi/10.1103/PhysRevD.110.074012 (7 Oct. 2024).

26. Lenihan, C., Kim, A. J., Šimkovic, F. & Kozik, E. Evaluating Second-Order Phase Transitions with Diagrammatic Monte Carlo: Néel Transition in the Doped Three-Dimensional Hubbard Model. *Physical Review Letters* **129,** 1–6. ISSN: 10797114. arXiv: 2112.15209 (2022).

27. Prokof'ev, N. V. & Svistunov, B. V. Polaron Problem by Diagrammatic Quantum Monte Carlo. *Phys. Rev. Lett.* **81,** 2514–2517. https://link.aps.org/doi/10.1103/PhysRevLett.81.2514 (12 1998).

28. Van Houcke, K., Kozik, E., Prokof'ev, N. & Svistunov, B. Diagrammatic Monte Carlo. *Physics Procedia* **6,** 95–105. ISSN: 18753892. arXiv: 0802.2923 (2010).

29. Rossi, R. *et al.* Contact and Momentum Distribution of the Unitary Fermi Gas. *Physical Review Letters* **121,** 130406. ISSN: 10797114. arXiv: 1303.6245. https://doi.org/10.1103/PhysRevLett.121.130406 (2018).

30. Van Houcke, K., Werner, F., Ohgoe, T., Prokof'Ev, N. V. & Svistunov, B. V. Diagrammatic Monte Carlo algorithm for the resonant Fermi gas. *Physical Review B* **99,** 35140. ISSN: 24699969. https://doi.org/10.1103/PhysRevB.99.035140 (2019).

31. Kozik, E. *et al.* Diagrammatic Monte Carlo for correlated fermions. *Epl* **90.** ISSN: 02955075. arXiv: 0907.0863 (2010).

32. Kugler, F. B. Counting Feynman diagrams via many-body relations. *Physical Review E* **98,** 1–9. ISSN: 24700053. arXiv: 1808.01759 (2018).

33. Šimkovic, F. *et al.* Magnetic correlations in the two-dimensional repulsive Fermi-Hubbard model. *Physical Review B* **96,** 2–6. ISSN: 24699969. arXiv: 1706.07556 (2017).

34. Šimkovic, F., Rossi, R. & Ferrero, M. Efficient one-loop-renormalized vertex expansions with connected determinant diagrammatic Monte Carlo. *Physical Review B* **102,** 1–11. ISSN: 24699969. arXiv: 2008.07377 (2020).

35. Kim, A. J., Werner, P. & Kozik, E. Strange Metal Solution in the Diagrammatic Theory for the $2d$ Hubbard Model, 1–7. arXiv: 2012.06159. http://arxiv.org/abs/2012.06159 (2020).

36. Wietek, A. *et al.* Mott Insulating States with Competing Orders in the Triangular Lattice Hubbard Model. *Physical Review X* **11,** 1–23. ISSN: 21603308. arXiv: 2102.12904 (2021).

37. Deng, Y., Kozik, E., Prokof'Ev, N. V. & Svistunov, B. V. Emergent BCS regime of the two-dimensional fermionic Hubbard model: Ground-state phase diagram. *Epl* **110,** 1–6. ISSN: 12864854. arXiv: 1408.2088 (2015).

38. Prokof'ev, N. & Svistunov, B. Bold diagrammatic Monte Carlo technique: When the sign problem is welcome. *Physical Review Letters* **99,** 1–4. ISSN: 00319007 (2007).

39. Kozik, E., Ferrero, M. & Georges, A. Nonexistence of the luttinger-ward functional and misleading convergence of skeleton diagrammatic series for hubbard-like models. *Physical Review Letters* **114,** 1–5. ISSN: 10797114. arXiv: 1407.5687 (2015).

40. Rubtsov, A. N., Savkin, V. V. & Lichtenstein, A. I. Continuous-time quantum Monte Carlo method for fermions. *Phys. Rev. B* **72,** 035122. https://link.aps.org/doi/10.1103/PhysRevB.72.035122 (3 2005).

41. Rossi, R. Determinant Diagrammatic Monte Carlo Algorithm in the Thermodynamic Limit. *Physical Review Letters* **119,** 1–5. ISSN: 10797114 (2017).

42. Chen, K. & Haule, K. A combined variational and diagrammatic quantum Monte Carlo approach to the many-electron problem. *Nature Communications* **10,** 3725. ISSN: 2041-1723. https://doi.org/10.1038/s41467-019-11708-6 (2019).

43. Taheridehkordi, A., Curnoe, S. H. & Leblanc, J. P. Algorithmic Matsubara integration for Hubbard-like models. *Physical Review B* **99,** 1–5. ISSN: 24699969. arXiv: 1808.05188 (2019).

44. Taheridehkordi, A., Curnoe, S. H. & Leblanc, J. P. Optimal grouping of arbitrary diagrammatic expansions via analytic pole structure. *Physical Review B* **101,** 1–12. ISSN: 24699969. arXiv: 1911.11129 (2020).

45. Klett, M. *et al.* Real-space cluster dynamical mean-field theory: Center-focused extrapolation on the one- and two particle-levels. *Phys. Rev. Res.* **2,** 033476. https://link.aps.org/doi/10.1103/PhysRevResearch.2.033476 (3 Sept. 2020).

46. Prokof'ev, N. V., Svistunov, B. V. & Tupitsyn, I. S. "Worm" algorithm in quantum Monte Carlo simulations. *Physics Letters, Section A: General, Atomic and Solid State Physics* **238,** 253–257. ISSN: 03759601 (1998).

47. Gukelberger, J., Kozik, E. & Hafermann, H. Diagrammatic Monte Carlo approach for diagrammatic extensions of dynamical mean-field theory: Convergence analysis of the dual fermion technique. *Physical Review B* **96,** 1–25. ISSN: 24699969. arXiv: 1611.07523 (2017).

48. Moutenet, A., Wu, W. & Ferrero, M. Determinant Monte Carlo algorithms for dynamical quantities in fermionic systems. *Phys. Rev. B* **97,** 085117. https://link.aps.org/doi/10.1103/PhysRevB.97.085117 (8 Feb. 2018).

49. Burovski, E., Prokof'ev, N., Svistunov, B. & Troyer, M. The Fermi–Hubbard model at unitarity. *New Journal of Physics* **8,** 153. https://dx.doi.org/10.1088/1367-2630/8/8/153 (Aug. 2006).

50. Rossi, R. & Rossi, R. Contributions to unbiased diagrammatic methods for interacting fermions (2018).

51. Kozik, E., Burovski, E., Scarola, V. W. & Troyer, M. Néel temperature and thermodynamics of the half-filled three-dimensional Hubbard model by dia-

grammatic determinant Monte Carlo. *Phys. Rev. B* **87,** 205102. https://link.aps.org/doi/10.1103/PhysRevB.87.205102 (20 May 2013).

52. We credit this idea to Lars Schonenberg, an early developer of the Unitary Fermi Gas code Gunnar Ḿoller has worked on.

53. Cotton, F. A. *Chemical applications of group theory* 3rd ed. eng. ISBN: 0471510947 (Wiley, New York, 1990).

54. Heine, V. Group Theory: Application to the Physics of Condensed Matter. *Physics Today* **61,** 57–58. ISSN: 0031-9228. eprint: https://pubs.aip.org/physicstoday/article-pdf/61/11/57/8318796/57_2_online.pdf. https://doi.org/10.1063/1.3027994 (2008).

55. Geilhufe, R. M. & Hergert, W. GTPack: A Mathematica Group Theory Package for Application in Solid-State Physics and Photonics. *Frontiers in Physics* **6,** 86. ISSN: 2296-424X. https://www.frontiersin.org/article/10.3389/fphy.2018.00086 (2018).

56. Kaye, J., Chen, K. & Parcollet, O. Discrete Lehmann representation of imaginary time Green's functions. *Phys. Rev. B* **105,** 235115. https://link.aps.org/doi/10.1103/PhysRevB.105.235115 (23 2022).

57. Efron, B. *The Jackknife, the Bootstrap and Other Resampling Plans* eprint: https://epubs.siam.org/doi/pdf/10.1137/1.9781611970319 (Society for Industrial and Applied Mathematics, 1982).

58. Kim, A. J., Prokof'ev, N. V., Svistunov, B. V. & Kozik, E. Homotopic Action: A Pathway to Convergent Diagrammatic Theories. *Physical Review Letters* **126.** ISSN: 1079-7114. http://dx.doi.org/10.1103/PhysRevLett.126.257001 (2021).

59. Rossi, R., Werner, F., Prokof'ev, N. V. & Svistunov, B. Shifted-Action Expansion and Applicability of Dressed Diagrammatic Schemes. *arXiv.org,* 3654. arXiv: 1508.03654 [1508]. http://arxiv.org/abs/1508.03654 (2015).

60. Rossi, R., Ohgoe, T., Van Houcke, K. & Werner, F. Resummation of Diagrammatic Series with Zero Convergence Radius for Strongly Correlated Fermions. *Physical Review Letters* **121,** 130405. ISSN: 10797114. arXiv: 1802.07717. https://doi.org/10.1103/PhysRevLett.121.130405 (2018).

61. Wu, W., Ferrero, M., Georges, A. & Kozik, E. Controlling Feynman diagrammatic expansions: Physical nature of the pseudogap in the two-dimensional Hubbard model. *Physical Review B* **96,** 1–5. ISSN: 24699969. arXiv: 1608.08402 (2017).

62. Tange, O. *GNU Parallel 20221122* GNU Parallel is a general parallelizer to run multiple serial command line programs in parallel without changing them. 2022. https://doi.org/10.5281/zenodo.7347980.

63. LeBlanc, J. P. F. *et al.* Solutions of the Two-Dimensional Hubbard Model: Benchmarks and Results from a Wide Range of Numerical Algorithms. *Phys. Rev. X* **5,** 041041. https://link.aps.org/doi/10.1103/PhysRevX.5.041041 (4 Dec. 2015).

64. Varney, C. N. *et al.* Quantum Monte Carlo study of the two-dimensional fermion Hubbard model. *Phys. Rev. B* **80,** 075116. https://link.aps.org/doi/10.1103/PhysRevB.80.075116 (7 Aug. 2009).

65. Schilling, A., Cantoni, M., Guo, J. D. & Ott, H. R. Superconductivity above 130 K in the Hg–Ba–Ca–Cu–O system. *Nature* **363,** 56–58. ISSN: 1476-4687. https://doi.org/10.1038/363056a0 (May 1993).

66. Kurosaki, Y., Shimizu, Y., Miyagawa, K., Kanoda, K. & Saito, G. Mott Transition from a Spin Liquid to a Fermi Liquid in the Spin-Frustrated Organic Conductor κ-$(ET)_2Cu_2CN_e$. *Phys. Rev. Lett.* **95,** 177001. https://link.aps.org/doi/10.1103/PhysRevLett.95.177001 (17 2005).

67. Isono, T. *et al.* Gapless Quantum Spin Liquid in an Organic Spin-1/2 Triangular-Lattice κ-H_3Cat-EDT-TTF_2. *Phys. Rev. Lett.* **112,** 177201. https://link.aps.org/doi/10.1103/PhysRevLett.112.177201 (17 2014).

68. Shimizu, Y., Miyagawa, K., Kanoda, K., Maesato, M. & Saito, G. Spin Liquid State in an Organic Mott Insulator with a Triangular Lattice. *Phys. Rev. Lett.* **91,** 107001. https://link.aps.org/doi/10.1103/PhysRevLett.91.107001 (10 Sept. 2003).

69. Yamashita, S. *et al.* Thermodynamic properties of a spin-1/2 spin-liquid state in a κ-type organic salt. *Nature Physics* **4,** 459–462. ISSN: 1745-2481. https://doi.org/10.1038/nphys942 (2008).

70. Miksch, B. *et al.* Gapped magnetic ground state in quantum spin liquid candidate κ-$(BEDT\text{-}TTF)_2Cu_2(CN)_3$. *Science* **372,** 276–279. eprint: https://www.science.org/doi/pdf/10.1126/science.abc6363. https://www.science.org/doi/abs/10.1126/science.abc6363 (2021).

71. Anderson, P. Resonating valence bonds: A new kind of insulator? *Materials Research Bulletin* **8,** 153–160. ISSN: 0025-5408. https://www.sciencedirect.com/science/article/pii/0025540873901670 (1973).

72. Savary, L. & Balents, L. Quantum spin liquids: a review. *Reports on Progress in Physics* **80,** 016502. https://dx.doi.org/10.1088/0034-4885/80/1/016502 (2016).

73. Takada, K. *et al.* Superconductivity in two-dimensional CoO2 layers. *Nature* **422,** 53–55. ISSN: 1476-4687. https://doi.org/10.1038/nature01450 (2003).

74. Schaak, R. E., Klimczuk, T., Foo, M. L. & Cava, R. J. Superconductivity phase diagram of NaxCoO2·1.3H2O. *Nature* **424,** 527–529. ISSN: 1476-4687. https://doi.org/10.1038/nature01877 (2003).

75. Honerkamp, C. Instabilities of interacting electrons on the triangular lattice. *Phys. Rev. B* **68,** 104510. https://link.aps.org/doi/10.1103/PhysRevB.68.104510 (10 Sept. 2003).

76. Koretsune, T., Motome, Y. & Furusaki, A. Exact Diagonalization Study of Mott Transition in the Hubbard Model on an Anisotropic Triangular Lattice. *Journal of the Physical Society of Japan* **76,** 074719. https://doi.org/10.1143/JPSJ.76.074719 (2007).

77. Sahebsara, P. & Sénéchal, D. Hubbard Model on the Triangular Lattice: Spiral Order and Spin Liquid. *Phys. Rev. Lett.* **100,** 136402. https://link.aps.org/doi/10.1103/PhysRevLett.100.136402 (13 Mar. 2008).

78. Clay, R. T., Li, H. & Mazumdar, S. Absence of Superconductivity in the Half-Filled Band Hubbard Model on the Anisotropic Triangular Lattice. *Phys. Rev. Lett.* **101,** 166403. https://link.aps.org/doi/10.1103/PhysRevLett.101.166403 (16 Oct. 2008).

79. Watanabe, T., Yokoyama, H., Tanaka, Y. & Inoue, J. Predominant magnetic states in the Hubbard model on anisotropic triangular lattices. *Phys. Rev. B* **77,** 214505. https://link.aps.org/doi/10.1103/PhysRevB.77.214505 (21 June 2008).

80. Galanakis, D., Stanescu, T. D. & Phillips, P. Mott transition on a triangular lattice. *Phys. Rev. B* **79,** 115116. https://link.aps.org/doi/10.1103/PhysRevB.79.115116 (11 Mar. 2009).

81. Yoshioka, T., Koga, A. & Kawakami, N. Quantum Phase Transitions in the Hubbard Model on a Triangular Lattice. *Phys. Rev. Lett.* **103,** 036401. https://link.aps.org/doi/10.1103/PhysRevLett.103.036401 (3 July 2009).

82. Yang, H.-Y., Läuchli, A. M., Mila, F. & Schmidt, K. P. Effective Spin Model for the Spin-Liquid Phase of the Hubbard Model on the Triangular Lattice. *Phys. Rev. Lett.* **105,** 267204. https://link.aps.org/doi/10.1103/PhysRevLett.105.267204 (26 Dec. 2010).

83. Kokalj, J. & McKenzie, R. H. Thermodynamics of a Bad Metal–Mott Insulator Transition in the Presence of Frustration. *Phys. Rev. Lett.* **110,** 206402. https://link.aps.org/doi/10.1103/PhysRevLett.110.206402 (20 May 2013).

84. Yamada, A. Magnetic properties and Mott transition in the Hubbard model on the anisotropic triangular lattice. *Phys. Rev. B* **89,** 195108. https://link.aps.org/doi/10.1103/PhysRevB.89.195108 (19 May 2014).

85. Li, G., Antipov, A. E., Rubtsov, A. N., Kirchner, S. & Hanke, W. Competing phases of the Hubbard model on a triangular lattice: Insights from the entropy. *Phys. Rev. B* **89,** 161118. https://link.aps.org/doi/10.1103/PhysRevB.89.161118 (16 Apr. 2014).

86. Lee, K., Sharma, P., Vafek, O. & Changlani, H. J. Triangular lattice Hubbard model physics at intermediate temperatures. *Phys. Rev. B* **107,** 235105. https://link.aps.org/doi/10.1103/PhysRevB.107.235105 (23 June 2023).

87. Ngo, V. T. & Diep, H. T. Phase transition in Heisenberg stacked triangular antiferromagnets: End of a controversy. *Physical Review E - Statistical, Nonlinear, and Soft Matter Physics* **78.** ISSN: 15393755. arXiv: 0808.0520 (2008).

88. Collins, M. F. & Petrenko, O. A. *Triangular antiferromagnets* **9,** 605–655. ISBN: 9055297070. arXiv: 9706153 [cond-mat] (1997).

89. Tocchio, L. F., Gros, C., Valentí, R. & Becca, F. One-dimensional spin liquid, collinear, and spiral phases from uncoupled chains to the triangular lattice. *Phys. Rev. B* **89,** 235107. https://link.aps.org/doi/10.1103/PhysRevB.89.235107 (23 June 2014).

90. Laubach, M., Thomale, R., Platt, C., Hanke, W. & Li, G. Phase diagram of the Hubbard model on the anisotropic triangular lattice. *Phys. Rev. B* **91,** 245125. https://link.aps.org/doi/10.1103/PhysRevB.91.245125 (24 2015).

91. Mishmash, R. V., González, I., Melko, R. G., Motrunich, O. I. & Fisher, M. P. A. Continuous Mott transition between a metal and a quantum spin liquid. *Phys. Rev. B* **91,** 235140. https://link.aps.org/doi/10.1103/PhysRevB.91.235140 (23 June 2015).

92. Szasz, A., Motruk, J., Zaletel, M. P. & Moore, J. E. Chiral Spin Liquid Phase of the Triangular Lattice Hubbard Model: A Density Matrix Renormalization Group Study. *Phys. Rev. X* **10,** 021042. https://link.aps.org/doi/10.1103/PhysRevX.10.021042 (2 May 2020).

93. Szasz, A. & Motruk, J. Phase diagram of the anisotropic triangular lattice Hubbard model. *Phys. Rev. B* **103,** 235132. https://link.aps.org/doi/10.1103/PhysRevB.103.235132 (23 June 2021).

94. Cookmeyer, T., Motruk, J. & Moore, J. E. Four-Spin Terms and the Origin of the Chiral Spin Liquid in Mott Insulators on the Triangular Lattice. *Phys. Rev. Lett.* **127,** 087201. https://link.aps.org/doi/10.1103/PhysRevLett.127.087201 (8 Aug. 2021).

95. Chen, B.-B. *et al.* Quantum spin liquid with emergent chiral order in the triangular-lattice Hubbard model. *Phys. Rev. B* **106,** 094420. https://link.aps.org/doi/10.1103/PhysRevB.106.094420 (9 Sept. 2022).

96. Downey, P.-O. *et al.* Mott transition, Widom line, and pseudogap in the half-filled triangular lattice Hubbard model. *Phys. Rev. B* **107,** 125159. https://link.aps.org/doi/10.1103/PhysRevB.107.125159 (12 Mar. 2023).

97. Morita, H., Watanabe, S. & Imada, M. Nonmagnetic Insulating States near the Mott Transitions on Lattices with Geometrical Frustration and Implications for κ-(ET)2Cu2(CN)3. *Journal of the Physical Society of Japan* **71,** 2109–2112. https://doi.org/10.1143/JPSJ.71.2109 (2002).

98. Georges, A. & Kotliar, G. Hubbard model in infinite dimensions. *Phys. Rev. B* **45,** 6479–6483. https://link.aps.org/doi/10.1103/PhysRevB.45.6479 (12 Mar. 1992).

99. Jarrell, M. Hubbard model in infinite dimensions: A quantum Monte Carlo study. *Phys. Rev. Lett.* **69,** 168–171. https://link.aps.org/doi/10.1103/PhysRevLett.69.168 (1 July 1992).

100. Maier, T., Jarrell, M., Pruschke, T. & Hettler, M. H. Quantum cluster theories. *Rev. Mod. Phys.* **77,** 1027–1080. https://link.aps.org/doi/10.1103/RevModPhys.77.1027 (3 Oct. 2005).

101. Balzer, M., Kyung, B., Sénéchal, D., Tremblay, A.-M. S. & Potthoff, M. First-order Mott transition at zero temperature in two dimensions: Variational plaquette study. *Europhysics Letters* **85,** 17002. https://dx.doi.org/10.1209/0295-5075/85/17002 (Jan. 2009).

102. Dang, H. T., Xu, X. Y., Chen, K.-S., Meng, Z. Y. & Wessel, S. Mott transition in the triangular lattice Hubbard model: A dynamical cluster approximation study. *Phys. Rev. B* **91,** 155101. https://link.aps.org/doi/10.1103/PhysRevB.91.155101 (15 Apr. 2015).

103. Fratino, L., Sémon, P., Sordi, G. & Tremblay, A.-M. S. An organizing principle for two-dimensional strongly correlated superconductivity. *Scientific Reports* **6,** 22715. ISSN: 2045-2322. https://doi.org/10.1038/srep22715 (Mar. 2016).

104. Fratino, L., Sémon, P., Charlebois, M., Sordi, G. & Tremblay, A.-M. S. Signatures of the Mott transition in the antiferromagnetic state of the two-dimensional Hubbard model. *Phys. Rev. B* **95,** 235109. https://link.aps.org/doi/10.1103/PhysRevB.95.235109 (23 June 2017).

105. Xu, L. *et al.* Relation between the Widom line and the dynamic crossover in systems with a liquid–liquid phase transition. *Proceedings of the National Academy of Sciences* **102,** 16558–16562. https://www.pnas.org/doi/abs/10.1073/pnas.0507870102 (2005).

106. Shirakawa, T., Tohyama, T., Kokalj, J., Sota, S. & Yunoki, S. Ground-state phase diagram of the triangular lattice Hubbard model by the density-matrix renormalization group method. *Phys. Rev. B* **96,** 205130. https://link.aps.org/doi/10.1103/PhysRevB.96.205130 (20 Nov. 2017).

107. Antipov, A. E., Rubtsov, A. N., Katsnelson, M. I. & Lichtenstein, A. I. Electron energy spectrum of the spin-liquid state in a frustrated Hubbard model. *Phys. Rev. B* **83,** 115126. https://link.aps.org/doi/10.1103/PhysRevB.83.115126 (11 Mar. 2011).

108. Tocchio, L. F., Feldner, H., Becca, F., Valentí, R. & Gros, C. Spin-liquid versus spiral-order phases in the anisotropic triangular lattice. *Phys. Rev. B* **87,** 035143. https://link.aps.org/doi/10.1103/PhysRevB.87.035143 (3 Jan. 2013).

109. Goto, S., Kurihara, S. & Yamamoto, D. Incommensurate spiral magnetic order on anisotropic triangular lattice: Dynamical mean-field study in a spin-rotating frame. *Phys. Rev. B* **94,** 245145. https://link.aps.org/doi/10.1103/PhysRevB.94.245145 (24 Dec. 2016).

110. Garioud, R. *et al.* Symmetry-Broken Perturbation Theory to Large Orders in Antiferromagnetic Phases. *Phys. Rev. Lett.* **132,** 246505. https://link.aps.org/doi/10.1103/PhysRevLett.132.246505 (24 June 2024).

111. Rossi, R., Šimkovic, F. & Ferrero, M. Renormalized perturbation theory at large expansion orders. *Epl* **132.** ISSN: 12864854. arXiv: 2001.09133 (2020).

112. Šimkovic, F. & Kozik, E. Determinant Monte Carlo for irreducible Feynman diagrams in the strongly correlated regime. *Physical Review B* **100,** 1–6. ISSN: 24699969. arXiv: 1712.10001 (2019).

113. Lenihan, C., Kim, A. J., Simkovic Iv., F. & Kozik, E. Entropy in the Non-Fermi-Liquid Regime of the Doped 2 D Hubbard Model. *Physical Review Letters* **126,** 1–6. ISSN: 10797114. arXiv: 2001.09948 (2021).

114. *Quantum Materials: Experiments and Theory* (eds Pavarini, E., Koch, E., van den Brink, J. & Sawatzky, G.) 420 S. ISBN: 978-3-95806-159-0. https://juser.fz-juelich.de/record/819465 (Forschungszentrum Jülich GmbH Zentralbibliothek, Verlag, Jülich, Sept. 12, 2016).

115. Richardson, R. C. The Pomeranchuk effect. *Rev. Mod. Phys.* **69,** 683–690. https://link.aps.org/doi/10.1103/RevModPhys.69.683 (3 July 1997).

116. Georges, A. & Krauth, W. Physical properties of the half-filled Hubbard model in infinite dimensions. *Phys. Rev. B* **48,** 7167–7182. https://link.aps.org/doi/10.1103/PhysRevB.48.7167 (10 Sept. 1993).

117. Rozenberg, M. J., Kotliar, G. & Zhang, X. Y. Mott-Hubbard transition in infinite dimensions. II. *Phys. Rev. B* **49,** 10181–10193. https://link.aps.org/doi/10.1103/PhysRevB.49.10181 (15 Apr. 1994).

118. Georges, A. & Krauth, W. Numerical solution of the d=∞ Hubbard model: Evidence for a Mott transition. *Phys. Rev. Lett.* **69,** 1240–1243. https://link.aps.org/doi/10.1103/PhysRevLett.69.1240 (8 Aug. 1992).

119. Daré, A.-M., Raymond, L., Albinet, G. & Tremblay, A.-M. S. Interaction-induced adiabatic cooling for antiferromagnetism in optical lattices. *Phys. Rev. B* **76,** 064402. https://link.aps.org/doi/10.1103/PhysRevB.76.064402 (6 Aug. 2007).

120. Werner, F., Parcollet, O., Georges, A. & Hassan, S. R. Interaction-Induced Adiabatic Cooling and Antiferromagnetism of Cold Fermions in Optical Lattices. *Phys. Rev. Lett.* **95,** 056401. https://link.aps.org/doi/10.1103/PhysRevLett.95.056401 (5 July 2005).

121. Walsh, C., Sémon, P., Sordi, G. & Tremblay, A.-M. S. Critical opalescence across the doping-driven Mott transition in optical lattices of ultracold atoms. *Phys. Rev. B* **99,** 165151. https://link.aps.org/doi/10.1103/PhysRevB.99.165151 (16 Apr. 2019).

122. Cheuk, L. W. *et al.* Observation of spatial charge and spin correlations in the 2D Fermi-Hubbard model. *Science* **353,** 1260–1264. eprint: https://www.science.org/doi/pdf/10.1126/science.aag3349. https://www.science.org/doi/abs/10.1126/science.aag3349 (2016).

123. Qin, M. Effect of hole doping on the 120 degree order in the triangular lattice Hubbard model: a Hartree–Fock revisit. *Journal of Physics: Condensed Matter* **34,** 235603. https://dx.doi.org/10.1088/1361-648X/ac5e79 (Apr. 2022).

124. Yuste, A., Moreno-Cardoner, M. & Sanpera, A. Using random boundary conditions to simulate disordered quantum spin models in two-dimensional systems. *Phys. Rev. B* **95,** 195167. https://link.aps.org/doi/10.1103/PhysRevB.95.195167 (19 2017).

125. Kyung, B. & Tremblay, A.-M. S. Mott Transition, Antiferromagnetism, and *d*-Wave Superconductivity in Two-Dimensional Organic Conductors. *Phys. Rev. Lett.* **97,** 046402. https://link.aps.org/doi/10.1103/PhysRevLett.97.046402 (4 July 2006).

126. Acheche, S., Reymbaut, A., Charlebois, M., Sénéchal, D. & Tremblay, A.-M. S. Mott transition and magnetism on the anisotropic triangular lattice. *Phys. Rev. B* **94,** 245133. https://link.aps.org/doi/10.1103/PhysRevB.94.245133 (24 2016).

127. Yamada, A. Magnetic properties and Mott transition of the Hubbard model for weakly coupled chains on the anisotropic triangular lattice. *Phys. Rev. B* **90,** 235138. https://link.aps.org/doi/10.1103/PhysRevB.90.235138 (23 2014).

128. Misumi, K., Kaneko, T. & Ohta, Y. Phase Diagram of the Frustrated Square-Lattice Hubbard Model: Variational Cluster Approach. *Journal of the Physical Society of Japan* **85,** 064711. eprint: https://doi.org/10.7566/JPSJ.85.064711 (2016).

129. Willsher, J., Jin, H.-K. & Knolle, J. Magnetic excitations, phase diagram, and order-by-disorder in the extended triangular-lattice Hubbard model. *Phys. Rev. B* **107,** 064425. https://link.aps.org/doi/10.1103/PhysRevB.107.064425 (6 Feb. 2023).

130. Vojta, M. Frustration and quantum criticality. *Reports on Progress in Physics* **81.** ISSN: 00344885. arXiv: 1711.08455 (2018).

131. Claveau, Y., Arnaud, B. & Matteo, S. D. Mean-field solution of the Hubbard model: the magnetic phase diagram. arXiv: arXiv:1403.2259v1.

132. Prokof'ev, N. V. & Svistunov, B. V. Bold diagrammatic Monte Carlo: A generic sign-problem tolerant technique for polaron models and possibly interacting many-body problems. *Physical Review B - Condensed Matter and Materials Physics* **77,** 1–13. ISSN: 10980121 (2008).

133. Uhlarz, M., Pfleiderer, C. & Hayden, S. M. Quantum phase transitions in the itinerant ferromagnet ZrZn2. *Physical Review Letters* **93,** 2–5. ISSN: 00319007 (2004).

134. Belitz, D., Kirkpatrick, T. & Vojta, T. Nonanalytic behavior of the spin susceptibility in clean Fermi systems. *Physical Review B - Condensed Matter and Materials Physics* **55,** 9452–9462. ISSN: 1550235X (1997).

135. Betouras, J., Efremov, D. & Chubukov, A. Thermodynamics of a Fermi liquid in a magnetic field. *Physical Review B - Condensed Matter and Materials Physics* **72,** 1–5. ISSN: 10980121 (2005).

136. Sachdev, S. & Keimer, B. Quantum criticality. *Physics Today* **64,** 29–35. ISSN: 00319228. arXiv: 1102.4628 (2011).